AD-A251 850

AD_____

CONTRACT NO: DAMD17-88-C-8125

TITLE: SPECTROSCOPY OF BURN WOUNDS

PRINCIPAL INVESTIGATORS: Martin A. Afromowitz, Ph.D.
                           James D. Callis, Ph.D.

CONTRACTING ORGANIZATION: University of Washington
                           School of Medicine
                           Seattle, WA   98195

REPORT DATE: May 5, 1992

TYPE OF REPORT: Final Report

PREPARED FOR: U.S. ARMY MEDICAL RESEARCH AND DEVELOPMENT COMMAND
               Fort Detrick, Frederick, Maryland   21702-5012

DISTRIBUTION STATEMENT: Approved for public release;
                         distribution unlimited

The findings in this report are not to be construed as an
official Department of the Army position unless so designated by
other authorized documents.

92-16370

92 6 22 03?

REPORT DOCUMENTATION PAGE

1. AGENCY USE ONLY (Leave blank)	2. REPORT DATE	3. REPORT TYPE AND DATES COVERED
	5 May 1992	Final Report (7/15/88 – 7/14/91)

4. TITLE AND SUBTITLE

SPECTROSCOPY OF BURN WOUNDS

5. FUNDING NUMBERS

Contract No.
DAMD17-88-C-8125

63002A
3M263002D840.DA.001
WUDA315068

6. AUTHOR(S)

Martin A. Afromowitz, Ph.D.
James D. Callis, Ph.D.

7. PERFORMING ORGANIZATION NAME(S) AND ADDRESS(ES)

University of Washington
School of Medicine
Seattle, WA 98195

8. PERFORMING ORGANIZATION REPORT NUMBER

9. SPONSORING/MONITORING AGENCY NAME(S) AND ADDRESS(ES)

U.S. Army Medical Research and Development Command
Fort Detrick
Frederick, Maryland 21702-5012

10. SPONSORING/MONITORING AGENCY REPORT NUMBER

11. SUPPLEMENTARY NOTES

12a. DISTRIBUTION/AVAILABILITY STATEMENT

Approved for public release; distribution unlimited

12b. DISTRIBUTION CODE

13. ABSTRACT (Maximum 200 words)

This research seeks to develop non-invasive burn depth evaluation methods from non-contacting visible and near-infrared spectroscopic measurements. In previous years, we demonstrated that features of the optical reflection spectra of burn wounds can be correlated with the depth of burn. An imaging system was built which determined, with accuracy equal to or better than that of a skilled burn surgeon, the probability that burn sites would heal within three weeks from date of injury. Our goal for the current project is to investigate the optical reflectance properties of burns, utilizing the techniques of multivariate analysis, in order to improve the reliability of this instrument.

14. SUBJECT TERMS

RA II; Volunteers; Diagnosis; Burn Wounds; Burn Depth; Instrument; Burn Injuries

15. NUMBER OF PAGES

16. PRICE CODE

17. SECURITY CLASSIFICATION OF REPORT	18. SECURITY CLASSIFICATION OF THIS PAGE	19. SECURITY CLASSIFICATION OF ABSTRACT	20. LIMITATION OF ABSTRACT
Unclassified	Unclassified	Unclassified	Unlimited

ABSTRACT

This research seeks to develop non-invasive burn depth evaluation methods from non-contacting visible and near-infrared spectroscopic measurements. In previous years, we demonstrated that features of the optical reflection spectra of burn wounds can be correlated with the depth of burn. An imaging system was built which determined, with accuracy equal to or better than that of a skilled burn surgeon, the probability that burn sites would heal within three weeks from date of injury. Our goal for the current project is to investigate the optical reflectance properties of burns, utilizing the techniques of multivariate analysis, in order to improve the reliability of this instrument.

Excellent progress has been made toward achievement of the goals of this project. In the first year a commercial spectrophotometer was purchased and modified to make optical reflection measurements in both the visible and near-infrared regions (450-1800 nm). A library of reference spectra was acquired with this instrument.

During the second year, experiments were conducted to understand the major components of the reflectance spectra of human skin *in vivo*. Two dynamic processes which influence *in vivo* spectra were studied to improve our knowledge of burn physiology: temperature and ischemia. These were modeled in healthy human subjects. The spectrum of pure water, which is highly temperature dependent and dominates the spectra of biological tissues, was mathematically analyzed for the purpose of compensating for water absorbances in tissues.

Thirty four patients at Harborview Burn Center were studied, and the reflectance spectra of their burns analyzed with multivariate statistics. An unexpected absorption band correlating to burn depth was observed at 630 nm and was identified as arising from methemoglobin. Based on the foregoing results, a more reliable algorithm was developed for the imaging system. The new algorithm incorporates wavelengths which measure this methemoglobin absorption. It has been tested by simulating imaging system responses from spectrophotometer data. The new model predicts the healing potential of 110 burn sites with 88% accuracy, significantly better than simulated responses from the old imaging system (79%).

FOREWORD

Opinions, interpretations, conclusions and recommendations are those of the author and are not necessarily endorsed by the U.S. Army.

_____ Where copyrighted material is quoted, permission has been obtained to use such material.

_____ Where material from documents designated for limited distribution is quoted, permission has been obtained to use the material.

_~~i(~~ Citations of commercial organizations and trade names in this report do not constitute an official Department of the Army endorsement or approval of the products or services of these organizations.

_____ In conducting research using animals, the investigator(s) adhered to the "Guide for the Care and Use of Laboratory Animals," prepared by the Committee on Care and Use of Laboratory Animals of the Institute of Laboratory Animal Resources, National Research Council (NIH Publication No. 86-23, Revised 1985).

_~~/~~~/((For the protection of human subjects, the investigator(s) have adhered to policies of applicable Federal Law 45CFR46.

_____ In conducting research utilizing recombinant DNA technology, the investigator(s) adhered to current guidelines promulgated by the National Institutes of Health.

_____
PI Signature   Date

TABLE OF CONTENTS

INTRODUCTION

Burn injuries affect more than two million American victims each year. Two hundred thousand of these will require hospitalization and 10,000 will die.[1] Skin grafting has significantly reduced infection, mortality, and disfigurement in patients with deep wounds. Shallow wounds, however, produce smoother skin when they are allowed to heal on their own. As a general rule, only burns which do not heal in 21 days benefit from grafting[2,3]. An accurate diagnosis may be obtained by waiting for 3 weeks before deciding to operate, but it has been shown that grafting within the first few days produces better surgical results and reduces hospital stay[*2]. This has been the driving force behind the development of methods to predict potential healing times.

For a wound to heal well (and within 21 days), it must re-epithelialize from remnants of epithelium in the lining of ducts and hair follicles. No one has yet proposed a method to predict healing by measuring the abundance of epithelium. Instead, most estimate the depth of irreparably damaged tissue with respect to the total thickness of the dermis.

Many hospitals today use a technique called clinical assessment which combines visual inspection with simple tests, such as the wound's sensitivity to touch[4]. Data collection, even for the largest and most variegated wounds, requires less than 15 minutes and does not cause excessive pain, neither from the tests themselves or from prolonged exposure of the wound. However, the accuracy of this technique is highly dependent on the experience of the assessor. Other techniques, including histopathological inspection,[5,6,7] topical application of dyes,[8] radio isotope studies,[9] ultrasound,[10] thermography,[11,12] pulse oximetry,[13] laser doppler flowmetry,[14,15] and multispectral photographic analyzers,[16,17] have proven to be slower, more painful, or less reliable and are less commonly used.

The Burn Depth Indicator

In 1980 we built the Burn Depth Indicator (BDI), a hand-held probe which illuminated a 3 cm^2 area of wound with pulsed light from three LED chips and measured the reflected light. This technique proved to be as fast as clinical assessment, less painful, and significantly more reliable.[18,19] We developed a similar instrument in 1986, which provided spatially resolved burn wound diagnosis. This device, the Imaging Burn Depth Indicator (IBDI), produces a color-coded image of a wound.[20,21,22]

Selection of the wavelengths used by the BDI (green (550 nm), red (640 nm), and near infrared (880 nm)) was based on the visible appearance of burn wounds and the discovery that near infrared light is reflected more by deep burns than shallow.[*16] Van Liew interpreted the BDI measurements in terms of blood volume, blood oxygenation, and eschar thickness. The results of his model agreed well with both the measured data and the expected physiology.[*19,23]

Spectroscopic Oximetry _in vivo_

Measurement of blood oxygenation by spectral analysis of reflected or transmitted light is a well established method. Visible (400-700 nm) and short-wave near infrared (700-1100 nm) light have been employed. Hemoglobins have $\pi \to \pi^*$, $d \to d^*$ and $f \to f^*$ electronic transitions in this region. Oxidation and ligand binding influence the spectrum substantially (Figure 1). A non-invasive oximeter, the Pulsed Oximeter,[24] now common in hospitals, uses transmission of 660 and 920 nm light through a finger tip. Its results correlate well with arterial blood O_2 saturation measured by conventional, invasive methods.[25] The success of this method has stimulated research on other non-invasive, spectrophotometric oximeters. These new instruments measure either transmitted or

reflected light and have been applied to the head,[26,27] brain,[28] heart,[*28] and skin.[*28,29] These methods are rarely calibrated to give absolute values, due to the unavailability of reference data, but they are quite useful for clinical trend monitoring and kinetic studies, where relative changes are important.

Near Infrared Spectroscopy

Near infrared light (700-2500 nm) is absorbed by other biological components besides hemoglobins. Most near infrared (NIR) absorbances are due to overtones and combination bands of vibrational transitions, primarily C-H, N-H, and O-H. This region has been used in the agricultural and food processing industries to determine, for instance, protein, oil, and moisture content.[30,31] Samples are frequently analyzed in solid or powdered form by diffuse reflectance. The resulting absorption bands, despite the high degree of light scatter in the samples, are often linear with concentration. However the spectral bands are broad and overlapping, making analysis difficult. Calibrations are therefore based on empirically observed spectral behavior rather than on first principle considerations.

Multivariate Statistics

The key that has unlocked the potential of NIR spectroscopy is multivariate statistics, mathematical methods for analyzing data sets which include multiple measurements for each sample. For spectroscopy, each filter or each monochromator setting is used to obtain different information, producing a response vector for each sample. Multivariate statistics assists the analyst to find an empirical mathematical model which will best reproduce the values of one or more constituents, given the response

vectors of a set of calibration samples. Once the model is obtained, it may be used to estimate values for prediction samples, those whose constituents are unknown.

Constituents are usually chemical concentrations, but may also be physical properties, e.g. crystallinity of nylon yarns, or abstract properties, e.g. the loaf score of flour (the volume, appearance, texture, and spring of bread made with that flour) (31). The property needs only to have some systematic relation to the spectra. Multivariate statistics can be used to analyze the spectra of burn injuries to estimate healing potential, blood oxygenation, and other properties. Further, the results of these analyses and a more precise understanding of the spectra of burned skin can be used to optimize the algorithm currently used by the IBDI.

PRELIMINARY RESEARCH

THE SPECTROMETER

The instrument used is an LT Quantum 1200 spectrometer, which was specifically modified for this project by the manufacturer. It employs a concave holographic grating and a manually switched pair of filters to scan 900-1800 nm (first order) and 450-900 nm (second order). Light is conducted to the sample through a 2 m fiber optic cable (0.5 cm bundle). The reflected light is measured by two 45° PbS detectors in a module at the end of the cable (Figure 2). The module is suspended 1 to 2 cm over the sample and supported by a tripod. Data is collected for 40 seconds (100 scans) and analyzed with software written in the MATLAB[32] program environment. This instrument can measure the reflectance of 1 cm^2 of skin in less than 3 minutes, including the time required to position the patient and detector. It is completely painless, non-contacting, and non-destructive.

REFERENCE SPECTRA

Reference spectra of distilled water, mineral oil, collagen, and whole blood (Figures 3-6) were obtained using the LT spectrometer in trans-reflectance mode. Band assignments were made from Colthup type charts and other data[*30] and are listed in Table I. Reflectance spectra were also acquired from pork fat, pork muscle, beef tendon, and human skin *in vivo* (Figures 7-10). These spectra are composed of combinations of hydrocarbon, protein, and water absorbances. The primary absorber in biological tissues is water (80% by weight). Since the spectrum of water is highly temperature dependent, water spectra were studied in detail (pages 35 -46).

Although muscle, tendon, and skin are primarily water, their spectra are remarkably

different. The Beer-Lambert law (Absorbances of components add linearly),

$$A_{ij} = -\log_{10}(I_{ij} / I_{0,ij}) = b_i \left(_k\Sigma a_{jk}c_{ik}\right) \tag{1}$$

$A_{ij} = i^{th}$ sample absorbance at the jth wavelength

$I_{t,ij} = $ intensity of transmitted radiation

$I_{0,ij} = $ intensity of incident radiation

$a_{jk} = $ absorptivity of the kth chemical component at the jth wavelength,

$b_i = $ path length of light through sample = thickness of sample

$c_{ik} = $ concentration of the kth analyte in the ith sample

and the diffuse reflectance approximation

$$A_{ij} \approx \log(1/R_{ij}) \tag{2}$$

$$R_{ij} = (I_{reflected, \, ij}) / (I_{0,ij}) \tag{3}$$

are somewhat inappropriate for these samples; the assumptions on which these equations are based are not valid. Light scatter, stray light, specular reflectance, and distribution error cause pronounced non-linearities in the spectra of these tissues. The multiple layers of tissues in skin produce additional distortions. These non-linearities affect both the visible and NIR spectra and make theoretical analysis extremely difficult. On the other hand, they may provide clues to physical parameters, such as surface texture and hydration, distribution of blood cells in vessels and tissue, disruption of connective tissue layers, etc. These parameters generally cannot be measured directly, but their effects on the spectra of burn wounds may correlate empirically with healing time.

IN VIVO STUDIES

Skin Temperature

Preliminary *in vivo* studies were done to observe spectral changes due to expected dynamic processes. The first study investigated the effect of temperature. When skin is warmed, the capillaries dilate in a manner similar to the hyperemic response in burns. Reflectance spectroscopy should detect temperature dependent shifts in water bands and an increase in hemoglobin concentration.

Spectra were taken from the forearms of seven people at temperatures ranging from 9 to 35°C. The skin was cooled with water and heated with a lamp. Temperature was measured with a small thermistor at the surface of the skin.

One subject was studied in detail from 9 to 36°C. Figure 11a shows second derivative NIR spectra. The largest variations appear at 1150 and 1213 nm. Difference spectra were computed using the spectrum taken at 9°C as a reference (Figure 11b). The large peaks at 970, 1155, and 1390 nm in the difference spectra are attributed to the shifting of the water bands at elevated temperatures (Figure 11c).

Similar results were observed in all seven subjects. The subjects were divided into two groups. Step-wise linear regression was used to build two 3 wavelength models using each group as a separate calibration set. Both models used similar wavelengths (1016,1073,1156 and 1001,1076,1150 nm) The 1150,1156 and 1001,1016 nm wavelengths correspond to spectral changes of pure water. Each model was used to predict temperatures of the subjects in the other group (Figure 12). The standard errors of prediction (SEP) were 1.3° and 1.4°, approximately equal to the estimated accuracy of the reference method (1.5°C). The correlation coefficients were both 0.982. These results suggest that it may be possible to measure the surface temperature of a burn

wound and to monitor the inflammation of the wound as it responds to injury or infection.

Ischemia

The second study investigated the effect of ischemia, which may cause destruction in the zone of stasis. The largest changes would be expected in the visible region where the double-banded absorbance of oxyhemoglobin (HbO_2) would be replaced by the single, broad band of deoxyhemoglobin (Hb) (Figure 1a).

Ischemia was induced in the forearm of a healthy volunteer by applying a pressure cuff (150 mm Hg) for 8 minutes. Spectra were recorded in the visible region (450-780 nm) every 20 seconds, while circulation was restricted and for 8 minutes after it was released.

Figure 13 shows spectral (second derivative) shifts that occurred during ischemia. The two bands of oxyhemoglobin (540, 575 nm) are visible, as are the 555 and 760 nm bands of deoxyhemoglobin. Principal Component Analysis (PCA) resolves the spectra into two components (Figures 14a, 14c) corresponding to the average spectrum (primarily HbO_2) and the Hb-HbO_2 difference. The behavior of these components agrees with the known physiology of cuff induced ischemia: when the circulation is restricted, the blood becomes deoxygenated. When the restriction is released, the initial surge of new blood causes a hyperemic increase in blood volume, primarily oxygenated arterial blood, which gradually returns to normal equilibrium.[33] Figures 14b and 14d show the scores calculated by PCA, the estimated "concentrations" of HbO_2 and Hb components that were derived from the spectra. The deoxygenation (0-8 min.), overshoot (8 min.), and reestablishment of equilibrium (8-16 min.) are clearly visible. This study demonstrates that the LT spectrometer is capable of detecting changes in local blood oxygenation in the skin, without touching the patient or requiring pulsed blood flow.

HUMAN BURN PATIENTS AT THE NORTHWEST BURN CENTER

The main body of this research project is the analysis and interpretation of the spectra acquired from the skin of seriously burned patients at the Northwest Burn Center at Harborview Hospital.

EXPERIMENTAL

Human Subjects

Forty-three patients were studied at the Northwest Burn Center, Harborview Medical Center in Seattle, Washington, over a 13 month period. One fifth of the injuries were selected by the research nurse to give a representative sample of typical superficial, shallow partial, deep partial, and full thickness burns. The remainder were chosen because they were indeterminant or unusual. The medically fragile, including elderly, hemophiliac, and mentally ill patients, were excluded. Children were also excluded.

Patients were examined on the third day post-burn as was done in previous studies.[18] A few of the unusual injuries were studied on the fourth day, because the patients were transferred from other hospitals and were not available on the third day.

Two to five sites were chosen by the research nurse, often with the recommendation of the attending physician. After routine cleaning and debridement (removal of loose dead tissue), these sites were wrapped in cellophane to prevent drying and infection. Large wounds were rebandaged, except for the selected sites. The patient was then returned to his own room and positioned either in bed or in a chair. The cellophane was removed prior to spectral data acquisition.

One spectrum was acquired from each site, using the LT Quantum 1200 spectrophotometer.[34] Site locations were recorded on polaroid photographs. This

procedure generally took 15 to 30 minutes, including the time required to position the patient and to remove the equipment afterwards. If the patient was willing, IBDI images were also acquired, generally requiring another 10 to 20 minutes.

The injuries were followed by visual inspection for one month. The sites from which spectra had been acquired were classified according to outcome into three categories: Shallow (healed in less than 21 days), Deep (healed in more than 21 days), and Unknown. Most sites which were grafted were classified as deep. Those which were clearly shallow but were excised due to their proximity to a more severe injury were classified as shallow. If an injury was not grafted, it was inspected by the research nurse on or near the 21st day to determine if it had healed. When that was not possible, the information was obtained by phoning the patient. Sites for which there was insufficient information were classified as unknown and were excluded from analysis.

Of the sites whose outcomes were known, 34 were deep and 76 were shallow. The most common etiology was flame (52%), followed by scald (22%), chemical (8%), flash (8%), contact (6%), and grease (4%). The mean age of the patients was 33 years and the mean TBSA was 6%. There were 3 hispanics, 2 blacks, and 1 oriental. Burn locations included face, arms, hands, palms, backs, sides, legs, and feet.

Mathematical Methods

The multivariate mathematical methods needed to interpret data include preprocessing, calibration, and classification techniques. The goal is to find a useful relationship between a sample's spectrum (r) and the values of its constituents (c). Constituents are usually chemical concentrations, but may also be physical properties, abstract properties, or classifications. The property needs only to have some systematic relation to the spectra.

The notation used will be as follows: Matrices will be written in bold, upper case (**A**, **B**, **C**), row vectors in bold, lower case (**a**, **b**, **c**), and scalars in normal italic (*A*, *B*, *C*, *a*, *b*, *c*). Column vectors will be written as the transpose of row vectors ($\mathbf{a}^T$, $\mathbf{b}^T$, $\mathbf{c}^T$). Each spectrum will be referred to as a response row vector **r**, with length *J*, where *J* is the number of discrete wavelengths contained in each spectrum. *I* spectra grouped into a matrix will be **R**, with dimensions *I* by *J*. The elements of **R** will be written as r_{ij}. The matrix **C**, will be *I* by *K*, where *K* is the number of spectrally distinguishable constituents. The elements of **C** are c_{ik}.

Preprocessing

Preprocessing transforms the spectra such that the spectral features which correlate to the constituents are maximized and the remainder are minimized. The first step is usually linearization with respect to constituent concentration. Normally the logarithm of instrument response (*R*) is used for linearization:

$$R = I \,/\, I_0 \tag{3}$$

where I_0 is the intensity of the light incident on the sample and *I* is the intensity of the light that returns from the sample and is measured by the instrument. The sample absorbance (*A*) is

$$A = -\log_{10}(R) \tag{2}$$

and is proportional to analyte concentration (*c*) under certain conditions. The Beer-Lambert law is

$$A = a\,b\,c \tag{4}$$

where *b* is the path length, the distance the radiation traveled through the sample, and *a* is the molar absorptivity, a constant characteristic of the analyte. For a more complex sample, the sample absorbance (A_{ij}) is a linear sum of the absorbances of all

components.

$$A_{ij} = {}_k\Sigma A_{ijk} = b_i ({}_k\Sigma a_{jk} c_{ik})$$ (1)

It is assumed that all of the radiation travels the same distance through the sample so that b_i is constant for all rays. For diffuse reflectance, this is not strictly true, but it is often a useful approximation.

Other common transformations include mean centering, baseline subtraction, and derivatives. The equation for mean centering is

$$(r_j^T)_{mean\ centered} = r_j^T - 1/J\ \Sigma(r_{ij})$$ (5)

where r_j^T is the column vector of log(1/R) for the jth wavelength and all samples. Baseline subtraction is

$$(r_i)_{baseline\ corrected} = r_i - r_{i,Jb}$$ (6)

where r_i is the spectrum for sample i and $r_{i,Jb}$ is the absorbance at the J_b^{th} wavelength.

An estimation of the second derivative using a finite difference function is

$$f'' \approx (f_{j+g} - 2f_j + f_{j-g}) / g^2$$ (7)

where f_j is the intensity at the jth wavelength and g represents the gap size of the derivative.

Calibration

Calibration is used for continuous constituent values, such as chemical concentrations or physical properties. Calibration models must be validated before they may be used for prediction. In calibration, a model is developed that relates the spectra data matrix (**R**), composed of the spectra vectors r_i, to the constituent matrix (**C**), composed of the elements c_{ik}, for a set of samples, called the training set or the

calibration set (designated by the subscript $_c$). A second set is used for validation. The model is used to predict the constituent values of the second set. Poor prediction indicates that either irrelevant data, such as instrument noise was included in the calibration model (overfitting) or that there is variance in the validation set that was not present in the training set, such as a new component. Once the model has been validated, it may be used to predict the constituents of unknown samples (designated by the subscript $_p$).

Another method of validation, leave-one-out cross validation, is useful when there are only a few spectra available. Instead of dividing the set in two, half for the calibration set and half for the prediction set, all samples except one are used for the calibration set and the remaining sample becomes the prediction set. This is repeated I times, leaving out and predicting each spectra once. The result gives an estimate of the accuracy of the model that uses all I samples. Since the spectra acquired from different sites on the same wound may be highly correlated, this approach was modified: all spectra from a single patient were left out and predicted together.

Classical Least Squares

The calibration model generally consists of a vector of matrix of coefficients (**S**) that relates the constituent matrix to the spectral matrix. The coefficients are typically estimated by least squares or similar methods. The most straight forward methods calculate **S** assuming the Beer-Lambert relationship.

Classical least squares (CLS) is a direct calibration technique based on the Beer-Lambert law, which in matrix form is

$$\mathbf{R} = \mathbf{C}\,\mathbf{S} + \mathbf{E}_R \qquad\qquad (8)$$

where **S** is the estimated pure component spectra ($s_{jk} \approx a_{jk}\, b_{ij}$) and $\mathbf{E}_R$ is the matrix of

spectral errors. The **S** matrix is determined by

$$S = R_c C_c^+ \tag{9}$$

where R_c and C_c are the spectral and concentration matrices of the training set. C^+ is the Moor-Penrose pseudoinverse:[35]

$$C^+ = (C^T C)^{-1} C^T \tag{10}$$

By solving these equations, E_R is minimized in a least squares sense. The estimated concentrations $(\hat{c}_p^T)_i$ of all k components in the ith unknown sample with spectrum $(r_p^T)_i$ is

$$(\hat{c}_p^T)_i = (r_p^T)_i S^+ \tag{11}$$

It is often useful to include constraints, such as requiring all elements in **S** and $(\hat{c}_p^T)_i$ to be greater than or equal to zero.

Multiple Linear Regression

When the sample spectra cannot be approximated as a simple sum of pure component spectra, either because some of the components are unknown or because Beer's law is inapplicable, indirect calibration in used. The basic model is

$$C = R P + E_C \tag{12}$$

where E_C is the error in the concentration matrix and **P** is the I by J matrix of coefficients, similar to **S**. **C** may be any constituents, not just chemical concentrations. The equation is solved to minimize E_C, and prediction is

$$(\hat{c}_p^T)_i = (r_p^T)_i P \tag{13}$$

Since estimating **P** involves calculating the pseudoinverse of R_c, J must be small. If the spectra originally contain a large number of wavelengths, there are two methods of simplifying the spectral data: selecting a few relevant wavelengths and factoring the whole spectrum.

Multiple linear regression (MLR), also known as inverse least squares[36] and the P-matrix approach[37], is an inverse least squares model that uses the spectral data from a small, selected set of wavelengths. The model is

$$c_k^T = R\, p_k^T + e_c \qquad (14)$$

where p_k^T is the vector of regression coefficients for the kth constituent and e_c is the error in the concentration matrix.

The most common method for choosing the wavelengths to use in the MLR model is to calculate the correlation coefficients between all wavelengths and the constituent of interest. The wavelength with the greatest correlation in chosen as the first wavelength for the model. The variance associated with the correlation is removed from the spectral and constituent data and a second wavelength is chosen, and so on. Other methods also exist.

Principal Component Regression

Principal component regression (PCR)[38,39] uses the same fundamental definition as MLR but decomposes the full spectral matrix R into two factor matrices T and P,

$$R = T\,P + E_R \qquad (15)$$

which can be calculated by singular value decomposition:

$$R = V\,S\,U^T + E_R \qquad (16)$$

where V is I by A, S is A by A, and U^T is A by J, and A is the number of factors (principal components). T and P are VS and U^T, respectively. The matrix T contains "scores," linear combinations of concentration data, and P contains "loadings," linear combinations of spectral data. Scores and loadings are difficult to interpret in terms of the individual components. The concentrations can be estimated from the scores,

$$c = T\,q + e_c \qquad (17)$$

$$\mathbf{q} \approx \hat{\mathbf{T}}_c^+ \, \mathbf{c}_c \qquad (18)$$

$$\hat{\mathbf{c}}_p = \mathbf{R}_p \, \hat{\mathbf{P}}^T \, \hat{\mathbf{T}}_c^+ \, \mathbf{c}_c \qquad (19)$$

where $\mathbf{q}$ is the vector of coefficients that relates $\mathbf{c}$ to $\mathbf{T}$. If $\hat{\mathbf{c}}_p$ is not calculated, this method is known as principal component analysis (PCA) and does not require any constituent values. This method is useful as a classification technique, particularly when constituent values are unavailable.

Classification

When constituent data is discrete, such as the place of origin of the samples or "acceptable" and "unacceptable", classification algorithms are used. The most common is K Nearest Neighbors (KNN). The samples are treated as points in a multidimensional space and their "nearness" to each other are calculated:

$$D_{ij} = \| \mathbf{r}_i - \mathbf{r}_j \| \qquad (20)$$

where D_{ij} is the distance between samples i and j, and $\mathbf{r}_i$ and $\mathbf{r}_j$ are the spectral or score vectors for the two samples. It is assumed that samples within a class will be closer to each other than to samples in another class.

Like calibration, KNN classification requires a training set of samples whose classifications are known. However, there is no matrix of regression coefficients, an unknown sample is simply compared to all samples in the training set, one at a time. If $K = 1$, the unknown sample is assigned to the class of the training set sample that it is closest to. Otherwise the classifications of the K nearest training samples are considered.

The data used for KNN is often scaled (weighted) so that the variables which have the largest correlation to the classification are bigger than those which are less relevant. One common method of determining which variables are relevant is the variance weight,[40] which is the ratio of the intercategory variances to the sum of the intracategory

variances. The equation is

$$W_{ab} = 2 * [(1/N_a)\Sigma x_a^2 + (1/N_b)\Sigma x_b^2 - (2/N_aN_b)\Sigma x_a \Sigma x_b] /$$

$$[(1/N_a)\Sigma(x_a-x_{a,m})^2 + (1/N_b)\Sigma(x_b-x_{b,m})^2] \tag{21}$$

where N_a and N_b are the number of samples in classes a and b, x are the values of the variable in question, and $x_{a,m}$ is the mean of x for samples in class a.

RESULTS

Case Study

A case study is included here to illustrate typical results for shallow and full thickness burns. Patient #14 had a small scald burn on her foot. Hot water had run down into her high-top boot, producing a shallow partial thickness burn at the top and a deep burn where the water pooled at the bottom. In the spectrum of the shallow partial thickness burn (Figure 15a) the oxy- and deoxy- hemoglobin bands (400-600 nm) are very intense, because the epidermis was absent and the wound was inflamed. In the near infrared region (700-1800 nm) there are three absorbance bands that arise from the overtones of O-H stretching modes of water (960, 1150, and 1450 nm). The discontinuity in the spectrum at 900 nm is an instrumental artifact, caused by a filter change.

The spectrum of the deep burn (Figure 15b) was markedly different. The baseline was considerably higher and the water bands in the near infrared were less intense. The cause of these differences is unknown. The 560 nm hemoglobin bands are also less intense, as there is less blood in the injured skin. All of the above had been expected. At 630 nm, however, the is an unanticipated band. The intensity of this band, evident as a shoulder on the oxy-/deoxy- hemoglobin peak, suggested that it was due to another form of hemoglobin. The band was attributed to the acid form of methemoglobin which

has a band at 630 nm (Figure 1a). This compound is relatively well known and is present in normal subjects at the 0.5-1.0% level. Other hemoglobin derivatives may also be present in smaller quantities.

Principal Component Models

Raw Spectra

The spectra from all of the burn wounds are shown in Figure 16. Twelve spectra, acquired from discolored (black, brown, or green; n=10) and first degree (n=2) burns contain spectral features that are not relevant to the discrimination of shallow and deep burns. They were not included in any of the calibration models, to avoid making the models more complicated than necessary, but were included in predictions to demonstrate that they would not be misclassified. These spectra are shown in Figure 16 and subsequent figures as dotted lines.

The spectral regions which correlate to burn depth were located by calculating the variance weights (Equation 21) for the absorbances at each wavelength (Figure 17). There is some correlation between 550 and 580 nm, but little or none (variance weight = 2) anywhere else. This indicates that the hemoglobin absorbances (550-580 nm) have some correlation to burn depth, which is in accord with one of the fundamental tenets of clinical assessment, that the darker pink a wound is, the more likely it is to be shallow. The low correlation in other portions of the spectra indicates that the baseline offsets are unrelated to burn depth and are probably caused by irreproducibility in the source / sample / detector geometry.

Since the major spectral features do not correlate strongly to burn depth, the spectra were analyzed by Principal Component Analysis (Equations 15-19) to locate minor features which might be more relevant. The spectra would be expected to display at least

four major types of variation, corresponding to baseline offsets, multiplicative factors (path length and total blood concentration), oxygenation of the blood, and methemoglobin concentration. Minor variations, representing minor chemical components or spectral non-linearities would also be expected. The first four principal component loadings (spectral domain, Figure 18a,b) show that there are indeed at least four significant types of orthogonal spectral variance. The next four (Figure 18c,d) model only a small amount of the total variance. It is possible, but unlikely that these later factors are significant.

The principal component scores (concentration domain, Figure 19) show that the first two factors, are dominated by irrelevant effects of sample/instrument geometry. Similar effects have been observed in the diffuse reflectance spectra of other irregularly-shaped samples.[41] The third and fourth principal components, however, are correlated to burn depth. The variance weights for the first eight principal components are 2.3, 2.5, 2.7, 3.2, 2.5, 2.3, 2.0, and 2.0.

The distinction between "shallow" and "deep is a somewhat arbitrary division of a continuous variable, the fraction of dermis destroyed. It might be expected that in a multidimensional space, the scores for shallow burns might be located on one side and those for deep burns on the other, with the borderline injuries inbetween (Figure 19b). Shallow burns would most likely be closest to other shallow burns, etc., so KNN should give reasonable results. The KNN algorithm in Pirouette[42] successfully classified 100 (91%) of the 110 spectra, using 4 principal components. The optimal number of neighbors to consider was found to be 2. Cross validation, leaving out one patient's spectra each time (MATLAB program written by the author), successfully classified 101 (92%), using 6 principal components and considering 3 neighbors.

Assuming that there is only one continuous variable which relates to burn depth, another possible method of classification is to define a multidimensional plane between

the two classes. All scores on one side of the plane should represent shallow burns, and all scores on the other side should represent deep injuries. This plane may be found by rotating the axes so that the first axis corresponds to the direction of the variance in the data which most clearly distinguishes between the two classes. The discrimination plane is then perpendicular to the first rotated axis.

The algorithm used for single-plane discrimination involved 5 steps. The first step was to mean-center[39] the scores. Then the mean-centered scores were range scaled[39] and feature weighted,[39] according to the variance weight. The scaled data was then rotated, two dimensions at a time, starting with those which have the greatest variance weights. The best rotation was defined as that which produced the largest variance weight for the first of the two dimensions. Once the best rotation was found, the discrimination plane was defined perpendicular to the first axis, located so that the number of misclassified calibration samples was minimized. The samples were classified according to which side of the discrimination plane their rotated scores were located. The MATLAB code for these programs are in Appendix B.

The scores, rotated in the first four dimensions, are shown in Figure 20. The discrimination plane is also shown, projected as a line. All but 7 of the samples are correctly classified by this plane. Including more than four dimensions does not improve classification, since only the first four principal components contain much relevant information. Cross validation, using 4 principal components correctly classified 102 (93%). The single-plane discrimination is slightly better than KNN because only one dimension contains relevant information. The model is simpler and less influenced by any single calibration sample.

The loadings, rotated in the same manner (Figure 21), show that there is a strong positive correlation between the absorbance at 630 nm and the depth of the burn. This

is probably due to the absorbance of methemoglobin which appears to be characteristic of deep burns. There is also a strong negative correlation at 570 nm, where oxyhemoglobin absorbs. It is reasonable to assume that the more healthy, oxygenated hemoglobin a wound contains, the more likely it is to heal quickly. The first rotated loading is small for the wavelengths 650-700 nm indicating that this region, which contains little hemoglobin absorbance, is not useful for prediction. This further supports the previous results indicating that the baseline offsets are unrelated to burn depth. Subsequent rotated loadings (not shown) are not correlated to burn depth (variance weights < 2.2).

Baseline subtracted spectra

Since the baseline offsets are useless, they can be removed without losing information, approximating the baseline by the apparent absorbance at 700 nm (Equation 6, J_b = 700 nm). Among the resulting spectra (Figure 22) the spectral differences between the two classes are more obvious. The intensity of the hemoglobin absorbance (520-580 nm) is, on the average, greater for shallow injuries than for deep, but this variable alone is insufficient for diagnosis. Considering only the intensity of the absorbance, what the eye sees, only 69% of the injuries, at best, could be correctly classified. Clinical assessment considers a few other variables and is potentially more accurate.

Since the variance due to the offsets has been removed, fewer principal components should be needed to describe the data set. The first four loadings (Figure 23) are similar to those from the raw spectra (Figure 18). The subsequent loadings, however, contain more noise. The second and third principal components are most highly correlated (Figure 24), rather than the third and fourth (Figure 19), and the variance weights for the principal components are greater, 2.5, 4.6, 2.9, and 2.2 for the first four. Prediction results from KNN and single-plane discrimination are not significantly better, but the model is simpler.

Normalized spectra

Although the amount of blood visible in a wound is a good indication of its viability, it is an unreliable indicator. Edema (inflammation) and hematoma (bruising) both increase the amount of blood without increasing the healing potential. In this study, the diagnostic errors made by the physicians were caused either by injuries that were outside the range of their experience, such as an unusual chemical burn, or by deep injuries that appeared

pink instead of white. To correctly diagnose these wounds it is helpful to focus on the second factor which relates to burn depth, the methemoglobin content.

To remove the variance caused by variable amounts of blood in the skin, the spectra were normalized to the maximum of the average spectrum (570 nm was chosen). The normalization equation is

$$(r_i)_{normalized} = (r_i)_{baseline\ subtracted} / r_{i,570nm} \tag{22}$$

where $r_{i,570nm}$ is the apparent absorbance of the ith spectrum at 570 nm. The methemoglobin absorbance at 630 nm is clearly visible in the normalized spectra (Figure 25).

The removal of the multiplicative factors is inaccurate since this normalization is somewhat simplistic, so the rank of the spectral data set does not decrease. But since the data is simplified, the correlation to burn depth increases (Figure 26). The loadings (Figure 27) are similar to those of the baseline-corrected spectra (Figure 23), but the scores of the first two principal components (Figure 28) are more highly correlated. The variance weights for the first four principal components are 3.5, 5.3, 2.8, and 2.2. Prediction results are nearly identical to those from the baseline-corrected data.

Hemoglobin Spectra Model

Single Layer Model

The above results suggest that there is a single spectral feature or single combination of interrelated features which is indicative of the depth of a burn wound. Further, in the normalized spectra, the 630 nm absorbance, attributed to the acid form of methemoglobin, correlated to burn depth. This suggests that the concentration of acidic methemoglobin in the skin, relative to the total blood volume, is proportional to the amount of tissue damage and, hence, to the length of time required for healing.

Unfortunately, there is no way to test this hypothesis directly. Even if the patients consented to having skin samples removed for analysis, conventional methods of hemoglobin speciation are not applicable to solid tissue samples.

One alternative is to attempt to reproduce the observed reflectance spectra, starting from the spectra of pure hemoglobins. Assuming that (a) the particles in the skin scatter light isotropically, (b) the hemoglobin is uniformly distributed, (c) there is no specular reflectance or stray light, and (d) the only absorbing compounds in the skin are hemoglobins, then the reflectance spectra of the skin could be modeled as a linear sum of pure hemoglobin spectra, using Classical Least Squares (Equations 8-11). None of the assumptions are actually true and the hemoglobins used to acquire the basis spectra were not 100% pure, so the model is not expected to fit the data precisely. The spectra of the hemoglobins (the matrix S) are shown in Figure 29, including oxyhemoglobin, deoxyhemoglobin, acid methemoglobin, base methemoglobin, and a baseline. The spectra were fit to a reflectance spectrum of a burn wound, and a new spectrum was reconstructed from the estimated hemoglobin concentrations. This was repeated for all burn spectra.

Two examples are shown in Figure 30. The reconstructed spectra are not exactly the same as the measured spectra, since the assumptions are incorrect. This simplistic model does, however, give an estimate of methemoglobin in a burn, information which has previously been unavailable. The resulting predictions are less accurate (79%) than those from the empirical PCA models, indicating that the methemoglobin concentration alone is insufficient to predict healing or that the fitting errors were too large, probably both. However, the success of this model in discrimination does strongly support the hypothesis that oximetric information correlating to burn depth can be obtained from the spectra.

Two Layer Model

Of the assumptions used in the above model, two are approximately true, one might be true, and one is definitely false. The hemoglobin is not distributed homogeneously; in most cases there is a layer of bloodless, dead tissue (eschar) at the surface. This layer reflects incident light, reducing the amount that interacts with the blood beneath. The reflectance from a non-absorbing layer is dependent on light scattering and is a function of wavelength.

If the amount of light of wavelength j, reflected from the sample is I_j, and the total incident light is $I_{0,j}$, then the instrument response ($R_{obs,j}$) is

$$R_{obs,j} = I_j / I_{0,j} \tag{23}$$

$$R_{obs,j} = (I_{s,j} + I_{r,j}) / (I_{s0,j} + I_{r,j}) \tag{24}$$

where $I_{r,j}$ is the intensity reflected from the non-absorbing eschar layer, $I_{s0,j}$ is the intensity of the light that passes through the first layer and enters the second, blood-filled layer, and $I_{s,j}$ is the intensity of the light returning from the second layer. The fraction of the incident radiation that would be diffusely reflected from the second layer, if there were no specular reflectance and if the first layer were removed, is $R_{s,j}$,

$$R_{s,j} = I_{s,j} / I_{s0,j} \tag{25}$$

and is related to the absorbance of the blood in the second layer ($A_{s,j}$),

$$A_{s,j} \approx \log(1/R_{s,j}) \tag{26}$$

It can be estimated from the instrument response:

$$R_{s,j} = (I_{0,j} R_{obs,j} - I_{r,j}) / (I_{0,j} - I_{r,j}) \tag{27}$$

$$R_{s,j} = (T_{obs,j} - S_j) / (1 - S_j) \tag{28}$$

$$S_j = I_{r,j} / I_{0,j} \tag{29}$$

if S_j is known.

For the burn spectra, S is not known. Instead, S was approximated by a second

order polynomial, a function of the wavelength (λ):

$$S \approx s_0\, f(\lambda^0) \;+\; s_1\, f(\lambda^1) \;+\; s_2\, f(\lambda^2) \tag{30}$$

R_s should be, approximately, the product of the transmittances (T_k) of the hemoglobin species (k) times their concentrations (c_k).

$$R_s \approx {}_k\prod (c_k\, T_k) \tag{31}$$

And therefore

$$(T_{obs,j} - S_j)\, /\, (1 - S_j) \approx {}_k\prod (c_k\, T_k) \tag{32}$$

There are $3+k$ variables which must be solved simultaneously (s_0, s_1, s_2, c_1, c_2, ... c_k) by using a non-linear curve fitting algorithm and minimizing the spectral fitting error:

$$\text{error} = (T_{obs,j} - S_j)\, /\, (1 - S_j) \;-\; {}_k\prod (c_k\, T_k) \tag{33}$$

The Gauss-Newton algorithm supplied by Mathworks,[32] gave satisfactory results, under the following constraints:

$$c_k \geq 0 \tag{34}$$

$$0 \leq S_j \leq 1 \tag{35}$$

The reconstructed spectrum (A_{obs}) is then

$$T_{obs,j} = T_{s,j}\, (1 - S_j) + S_j \tag{36}$$

$$A_{obs,j} \approx -\log(T_{obs,j}) \tag{37}$$

The transmission spectra of hemoglobins and the functions $f(\lambda^0)$, $f(\lambda^1)$, and $f(\lambda^2)$ are shown in Figure 31. The reconstructed spectra for the two examples are shown in Figures 32 and 33. In general, the fit was not improved if S was assumed to be 0th order with respect to wavelength ($s_1 = 0$ and $s_2 = 0$). When S was 1st order, there was significant improvement; nearly all of the systematic distortion was accounted for. Adding the 2nd order improved some of the more unusual spectra, but generally had little effect on the "typical" spectra. The 1st order model indicated that deep burns usually have more than 9% acid methemoglobin (Figure 34) and correctly classified 90% of the injuries.

Skin Temperature Model

In the second year, spectra were acquired from the forearms of healthy volunteers. Their skin temperature was varied from 9 to 35 °C and measured with a thermistor at the surface. The spectra, after second derivative transformation, were analyzed by Multiple Linear Regression (Equations 12-14) and were found to correlate to the skin temperature (correlation coefficient R = 0.982), with a standard error of prediction of 1.4 °C. This experiment is described in the previous report.[43] The equation was

$$t = 22.7 + (1.21 \times 10^6)\, r''_{1015nm} - (1.44 \times 10^6)\, r''_{1073nm} - (3.85 \times 10^5)\, r''_{1156nm} \qquad (38)$$

where r''_{1015nm} is the second derivative (Equation 7, gap=23) at 1015 nm and t is the temperature in °C.

The model for estimating skin temperature in normal skin was used to estimate the temperature of the burn wounds (Figure 35). The results suggest that deeper burns are cooler than shallow burns (Figure 36). The average estimated temperatures were 32 ± 7 and 27 ± 7 for shallow and deep burns (P<0.01). Thermography, using emitted infrared light, has also shown that deep burns are cooler than shallow,[11,12] but that such measurements are extremely sensitive to cooling caused by evaporation of surface water. NIR reflectance should be less sensitive to surface effects, since it measures that temperature within the skin and below it. The model used here is not optimal; it is derived from healthy skin. A more accurate model could be obtained empirically, if the temperatures of wounds could be measured by a contacting or invasive probe, or theoretically, if the spectral non-linearities were better understood.

Although several features in the NIR spectra, including water temperature correlated to burn depth, none were as useful as the hemoglobin bands, nor did they improve prediction. It is likely that there is still much useful information in these spectra, but in the absence of physiological reference data, this information could only be extracted by

rigorous application of diffuse reflectance theory.

BDI and IBDI Simulations

Now it is possible to explain the predictive ability of the old Burn Depth Indicators (imaging and non-imaging). Both instruments used baseline-subtracted, single-wavelength normalized data. The baseline offsets were approximated by the instrument response of the NIR LED (880 nm) or filter (880-1100 nm) and the remaining data was normalized to the response of the Green (560 nm). The methemoglobin concentration was then, inadvertently, approximated by the normalized response of the Red (640 nm). The exact mathematics are slightly different, because instruments used the instrument response (R) rather that $\log(1/R)$, but the principle is the same.

In order to compare the prediction results from our spectrophotometer with predictions from the Burn Depth Indicator (BDI) and the Imaging Burn Depth Indicator (IBDI) built previously, the BDI and IBDI responses were simulated from our spectra. The emission spectra of the light emitting diodes (LED's) in the BDI were simulated as Gaussian-shaped peaks with maxima at 550, 640, and 880 nm and band widths (fwhm) of 70 nm.[21,22] The spectra of the IBDI filters (Figure 37b) were obtained from the literature.[20] The responses for the near infrared LED and filter are somewhat uncertain, because our spectral data between 750 and 890 nm is unreliable and was not used. The simulated results (Figures 38a and 38b), however, are reasonably close to those obtained in previous work.[19,22] For the few wounds for which IBDI images were acquired, the simulated results agree with the images. The burn sites used in this study seem to have a slightly wider range, both for the Red/NIR and Green/NIR ratios, than those used in previous studies, which is consistent with our attempt to select the widest variety of injuries. The accuracy of the BDI and IBDI simulations for prediction burn depth was

about 77 and 79%, respectively. VanLiew and Moore reported 79 and 84% accuracies for different sets of indeterminate burns for the two instruments.[18,20]

Proposed Model for New Imaging-Burn-Depth-Indicator

These results show that the model used for the Burn Depth Indicators was essentially sound and from the perspective of burn physiology, basically correct, though its explanation was erroneous. The choice of wavelengths, however, could be substantially improved. First, the filter originally selected for baseline subtraction (880-1100 nm) measures a large absorbance band at 970 nm (Figure 37) as well as the offsets. This band arises, in part, from the water in and on the skin. The water absorption is variable but not well correlated to burn depth. The 880-1100 nm filter also measures the absorbances of hemoglobins (Figure 1b), but the path length in this region is much longer than in the visible region. It is uncertain whether the blood in the volume sampled is representative of the blood in the skin or primarily below the skin. Furthermore, the BDI and IBDI simulations produced comparable results, in spite of the fact that the wavelength ranges used for baseline correction were significantly different. Therefore, little relevant information is lost and some interference is avoided by moving the baseline-correction filter to 650 or 700 nm, where the absorbances are significantly lower.

Second, the normalization filter could be narrowed and shifted to produce a more reliable response. There is a pronounced, non-linear distortion of the spectra which affects the 550-580 nm region where the hemoglobin absorbance is particularly strong. In the spectra of whole blood (Figure 1a), the two oxyhemoglobin absorption bands (535 and 570 nm) have similar intensities. In the burn spectra, however, the 535 nm band is decreased relative to the 570 nm band, and the degree of distortion is unrelated to burn

depth. The distortion is probably caused by scattering, and scattering is highly wavelength dependent. Therefore, the scattering at 630 nm is likely to be more similar to that at 570 nm than 535 nm, and the former should give a more accurate normalization for the 630 nm methemoglobin band. Simulations of fixed-filter instruments using various possible normalization filters confirm this. The normalization LED for the BDI had a 80 nm band width and was at 560 nm, sampling both oxyhemoglobin bands equally. The filter in the IBDI at 540 nm was worse, sampling only the most distorted portion of the oxyhemoglobin spectrum. A filter with a narrower band width, 30 nm or less, and located at 570 nm should give a more reliable normalization.

Third, the methemoglobin filter should be optimized. The filter used previously had a 80 nm band width and was centered at 640 nm. The methemoglobin absorbance peak is at 630 nm, and for the normalized spectra, the wavelength that correlates most to burn depth is 625 nm (Figure 26). The band width of the methemoglobin band is approximately 40 nm. A narrower filter, 40 nm fwhm or less, centered at 630 nm should give more precise estimates of methemoglobin absorbance.

One possible filter selection might include three 20-nm band pass filters at 650, 570, and 630 nm. If the apparent absorbances (log $(1/R)$) of the three filters are A_{650}, A_{570}, and A_{630} respectively (Figure 39), then the burn depth (D) is estimated by

$$D = (A_{630} - A_{650}) / (A_{570} - A_{650}) \qquad (39)$$

The discrimination point, calculated the same way as the discrimination plane for the rotated PCA scores, was found to be 0.104. Injuries for which D is greater than 0.104 were deep and the rest were shallow. One hundred one (92%) of the sites were correctly classified by this model, and 97 (88%) were classified during cross validation. This model was significantly more accurate (88%) than the IBDI simulation (79%) for the 104 sites simulated ($P < 0.06$ for paired data). Small variations in the band width or mean

wavelength of the filters do not significantly affect prediction ability, indicating that an instrument using this algorithm would be relatively tolerant of manufacturing variations.

Although binary predictions (shallow or deep) are convenient, it is often useful to rank injuries on a continuous scale, so that the size of the burn and patient comfort often may be weighted against the estimated healing potential. The proposed algorithm can be used to produces a continuous·scale (D) as well as binary predictions. For sites which were known to have healed in the third and fourth weeks post burn, there is roughly a linear correlation between instrument response and healing time (Figure 40). The estimated number of days required for healing (H) is

$$H = 30\,D + 15 \tag{40}$$

This relationship is not applicable to sites which heal in less than two or more than four weeks, but such information would rarely be important in management decisions.

For sites which heal between 14 and 28 days, the error in this model ($\pm$ 3 days) is comparable to the uncertainty of the reference method ($\pm$ 2 days). Whether or not a wound was healed (entirely reepethilialized) is difficult to determine precisely. Even among the Burn Center staff, opinions differed by a day or two. For wounds whose outcomes were described by patients over the phone or extrapolated from the nurses' last observations, the uncertainty was about $\pm$3 days.

CONCLUSIONS

With the LT spectrometer we are able to observe absorbance bands from most of the major constituents of skin. The instrument is sensitive enough to monitor changes as small as those induced by only a few degrees elevation in surface temperature. The techniques used are completely non-invasive, non-contacting, and non-destructive and require only a few minutes, making them suitable for use on burn patients.

In spite of the non-linear effects of light scattering and multiple layers, hemoglobin speciation can be estimated from visible reflectance measurements of burn wounds. Further, these estimates correlate to the depth of the injury. Severely elevated levels of methemoglobin have been observed in deep partial thickness and full thickness burns. This suggests that the Imaging Burn Depth Indicator estimates burn depth by analyzing the small color changes caused by the presence of methemoglobin. The IBDI, initially designed to measure deoxyhemoglobin, can be significantly improved by optimizing its filters to detect methemoglobin. The resulting instrument would be fast, accurate, non-invasive, and non-contacting and could produce a map of a wound, color-coded to indicate healing potential. This improved instrument could be used as a practical guide for burn treatment decisions and may assist in the study of burn physiology.

FUNDAMENTAL STUDIES OF WATER

INTRODUCTION

In order to understand the real factors that lead to the changes in reflection spectra from the burn sites, we have to investigate the temperature dependence of the water combination bands in the wavelength range used in our *in vivo* studies of human tissue. The main goal of these studies is to understand the structure of the observed peaks and the kinetics of the real molecules and structures that causes the observed changes in spectra. Another problem arises from the nonlinear dependence of the reflection spectra on the extinction and scattering of the tissue. In order to build a realistic model for temperature dependent reflection spectra, we need to find the "pure components" of the spectra and their behavior upon change of temperature. As long as water is the dominant component of tissue, understanding the structure of water and specifically how hydrogen bonding affects NIR spectra is one of the prominent problems in biophysics.

The structure of liquid water remains a most puzzling problem in the chemistry of solutions and electrolytes. Despite numerous attempts to build a consistent model of water through empirical data collected over the last 60 years, it must be admitted that no single description satisfactorily explains the majority of the collected data.[44] In principle, vibrational spectroscopy provides a precise tool for elucidation of the various species existing in water and water solutions. However, even in such a straightforward endeavor as deriving thermodynamic properties from IR absorption spectrophotometry and Raman-spectroscopy, the results are in poor agreement with each other and with other methods such as calorimetry. The main source of this ambiguity in spectra interpretation is concerned with the problems of the baseline determination[45] and with the difficulty of interpolation and deconvolution of broad bands which undergo subtle changes. A

number of investigators have attempted to deconvolve the absorption bands into an arbitrary number of gaussian bands. There is no theoretical reason for this procedure and the results are not consistent with any known theory. Recent advances in short wavelength NIR spectroscopy, driven by new technology for multichannel silicon detectors, makes this region of the water spectra, where only overtone and combination bands exist, very attractive for investigation. Indeed, many models of water explaining different features of the SW-NIR exist in the literature.[46-54]

The first studies of NIR combination bands were done more than three decades ago by Suhrmann and Breyer.[46,47] More recent investigation of NIR bands and a suggestion of a model containing three water species have been described by G.R.Choppin and K.Buijs in the early 60's.[49-50] They proposed that three bands can be distinguished in the absorption band of water between 1100 and 1300 nm, giving the spectral assignments and the extinction coefficients for each band. The concentration of each of the three absorbing species was calculated as a function of water temperature. Using this model and the concentration of each species, a number of the properties of water were calculated. The species were assumed to be non-bonded (monomer) and hydrogen bonded (dimer and trimer) intramolecular complexes. Their enthalpies were calculated from Van't Hoff equilibrium equations. Subsequently, different authors proposed models of water with two[50] and even five species[50] and many theoretical papers examining different models appeared in the last three decades. The most popular is the model proposed by Choppin and Buijs, and later elaborated by Senior and Vand[52], that explains the spectroscopic data in terms of bonded and nonbonded groups of molecules in water, is referred to as a mixture model. Opposed to this model are continuous models of the water structure.[53-54] The proponents of continuum theories emphasize the continuous evolution of the broad bands, rather than trying to deconvolve

them into substructures. From our point of view, the discrepancy between these two classes of the theoretical models appears to be more semantic, and they are supplementary rather than contradictory. In recent study of infrared spectra of aqueous dispersions Hübner et al.[55] have pointed out the danger of interpreting complex spectral bands solely on the basis of spectral shifts. They cite examples where deconvolution of the complex band explains the spectral shift in terms of discrete components, while the frequency shift of overall line contour leads to the opposite conclusions about the phase transition studied. The main argument against the structural (mixture) models of water is based on a statement that those models are not able to explain the entire collection of empirical data from spectroscopy, thermodynamic, and neutron diffraction. Nevertheless, in some recent papers[56-57], spectroscopic studies of the $2v_1 + v_3$ combination band (960 nm) in a wide range of pressures and temperatures has led to a reconsideration of the mixture model involving three species. In these papers, certain features of the continuum model are retained by use of the concept of energy bands[52] rather than discrete sharp energy levels. This model proposes a distribution of the hydrogen bond energies grouped around three component bands S_0, S_1 and S_2, i.e. a model featuring a relatively small number of distinguishable molecular species with continuous distribution of hydrogen bond length and angles associated with each specie. The combination band peak has been resolved into three gaussians with constant positions and widths.[58-57] Similar results have been presented by V.Fornes and J.Chaussidon[58] for the $v_2 + v_3$ first combination tone of water molecules. Both groups elaborate quantitative results for the energy of the hydrogen bond formation (rupture). All of the above mentioned investigators derived their data by fitting the spectral bands to the sum of two or more gaussians, in most cases with the aid of an analog "curve resolver".

Recent advances in multivariate statistics and low-noise NIR spectrometers

provides an impetus for restudy of the spectra of pure water as a function of temperature. Coupled with advances in instrumentation for high precision data acquisition are advances in data analysis. At present, there seems to be no existing methodology for quantitatively deciding the number of species contributing to water spectra. Clearly, arguments based upon the existence or absence of isosbestic point do not appear definitive nor do observations of spectral shifts of the mean position of complex peaks.

It is the purpose of this study to describe a technique for obtaining a lower bound to the number of species contributing to a series of spectra taken as a function of some external variable(e.g. temperature, pressure) within the linear additivity constraint. This technique which we call "Chemical Regression" was first proposed by Box and later described fully by Lawton and Sylvestre.[59,60] The method to be described more fully in the theory section relies on a description of the spectra in form of linear combination of the eigenvectors of the spectral data matrix. Criteria are available to determine a lower limit to the number of eigenspectra required to describe the signal variance while eliminating the noise variance. If the number of eigenspectra is small it can be argued that the mixture model has merit. On the other hand, a finding that a large number of basis vectors must be retained might be used to bolster the continuum model. Not only can a lower bound to the number of components be found, but also estimates of the spectra associated with each species can be obtained. This is accomplished by rotation of the abstract eigenvectors into a set of vectors which obey physical constrains appropriate to the problem. Thus the necessity to assume that the spectral shapes of the components is gaussian is eliminated and the spectral profiles are derived directly from the data. Constraints may be imposed not only on the spectra, e.g. positivity, but may also be imposed upon the way in which the intensity varies with the external variable (i.e. we may postulate a model for the effect of physical variance and derive the physical

parameters by least square fitting). Thus it would appear that chemical regression potentially provides further insight into the mechanism for spectral changes of water with temperature, yielding estimates for the number of species involved, the thermodynamic parameters governing their interrelationship and estimates of the spectra of each.

In this study we have used this new method to reexamine the 960 nm combination band in pure water. This band demonstrates a strong dependence on temperature changes and has a well defined isosbestic point, that could be a sign of the presence of two or more species in pure water. Another important reason for choosing the SW-NIR range for examining the structural model of water is connected to the evident fact that in this range the shift between the spectral components-species, if they do exist, would be more distinguishable[45], and their separation could be less ambiguous.

EXPERIMENTAL

The measurements were made with an in-house constructed SW-NIR diode-array spectrometer[61] and a 4-cm optical path length quartz cell, and repeated with the Hewlett Packard diode array spectrometer HP-6582A and a 2-cm cell inside the HP-spectrometer. In the case of the home-made spectrometer, the radiation was delivered to the cell with a fiber optic, which made temperature control more convenient and reduced fog on the windows. Temperature control was achieved by equilibrating the sample cell in a water bath at a fixed temperature. The temperature of the cell was measured with a thermocouple and the signal was digitized and registered on the computer's hard disk simultaneously with the digitized spectroscopic data from NIR spectrometer. The measured temperatures are believed to be correct to within $0.5°C$. The spectra of the pure distilled and deionized water in the spectral range 850-1100 nm were taken over the temperature range 10 - 80 °C. The cell filled with CCl_4 was used as reference. The

spectra are depicted in Figure 41. The spectra contain visible baseline offset and a slope. The nature of this bias and it's subtraction are discussed below. Nevertheless, we did not take special measures to improve the absolute measurements of the temperature, but the rate of the spectral scanning (60 scans per second) allowed us to reduce the noise by repetitive averaging. We believe that our experimental data for the studied combination band are the most precise at this time.

RESULTS

The temperature dependent offset could be referred to the changes of refractive index of water with the temperature. Fresnel reflection R changes according to the expression:

$$R = (n-1)^2/(n+1)^2 \tag{41}$$

where $n = n_q/n_w$, n_q and n_w are refractive indexes of quartz and water respectively. The changes in n_w in the entire temperature range are less than 1.5% and corresponding change in R are of order of 0.01. Taking into account that the cell has two interfaces with water and the effective absorbance will increase with the temperature (the refractive index and the reflectance are respectively decreasing), the baseline shift is estimated to be within 0.02 absorbance units, in good agreement with observed data. Now, understanding the nature of the baseline offset we can subtract it. The bias that is due to the strong absorption bands existing in the vicinity of the investigated peak could be approximated by the straight line and subtracted in the same way. After subtracting the offset and the slope the spectra appear more regular (Figure 42). We have taken into account the changes of the water density with the temperature. These small corrections are within 1.5% of the absorbance value.

In order to build a realistic model of water we need to determine the number of

latent variables that can describe the variance in the obtained spectra. There are different approaches to this problem. Most of them are based on the mathematical procedure of separating the noise or the bias from the real variance. This mathematical procedure is called Singular Value Decomposition (SVD). It consists of representation of the spectral matrix of absorption **A** in the form:

$$\mathbf{A} = \mathbf{USV'} \tag{42}$$

where **S** is diagonal matrix with the nonnegative diagonal elements in decreasing order, and **U** and **V** are unitary matrices, **V'** denotes the transposed **V** matrix. The columns of **A** represents the spectral vectors at a fixed temperature. The rows of **A** contain information about the variation in absorption at a fixed wavelength. We can also represent the experimental matrix **A** in the form

$$\mathbf{A} = \mathbf{DC} + \mathbf{E} \tag{43}$$

where matrix **D** contains only spectral components of the mixture and, the matrix **C** represents the concentration of the different components depending on the variable parameter (in our case the temperature). Matrix **E** contains experimental noise. From Equations 42 and 43 we can derive an equation:

$$\mathbf{DC} = \mathbf{USV'} \tag{44}$$

where **U**, **S**, and **V** are truncated matrices containing only the vectors and eigenvalues which are meaningful for the problem, namely they take into account the variance in the spectral matrix **A** and reject the noise. The representation of the experimental matrix **A** in the form of Equations 43 and 44 is well known as Principal Component Analysis (PCA).[62] PCA is a powerful tool in separating the noise from the real spectral components and estimating the most likely number of latent variables (meaningful singular eigenvalues) in the matrix **A**, that can describe the variance in **A** with reasonable precision. Since the determination of the number of "real" Principal Components and

elimination of those which describe the variance of the noise is an ambiguous task, we use auxiliary techniques, such as Evolving Factor Analysis[63]. The main concept of EFA is a graphical representation in which normalized (divided by the trace) singular values of the submatrices of matrix S in descending order versus the constituent, are displayed and examined for "emerging" eigenvalues. EFA has been used to analyze spectra, consisting of strongly overlapped peaks[62]. The normalized eigenvalues usually are depicted on a logarithmic scale. For the matrix A, corresponding to the spectra shown in Figure 42, EFA evidently shows three emerging eigenvalues. The results of EFA are illustrated in Figure 43. The investigation of the next spectral eigenvectors from matrix U shows that they contain much more noise than the first three, and hence they are useless for constructing the set of real spectral components. Therefore, PCA analysis suggests the same rank of three. Consistent with the estimation of rank three is the structure of the spectral eigenvectors as shown in Figure 44. These eigenvectors are largely free of noise. Examination of the higher eigenvectors showed them to be highly contaminated with noise (Figure 45) and too irreproducible to be of value in representation of our data set. Hence within our current signal level and reproducibility, a basis set of three components seems defensible. Now, starting with the assumption of three components, we can try to rotate our spectral eigenvectors (Figure 44) to the set of real spectral peaks. The procedure of nonlinear regression based on the postulated reaction has been described by Shrager[64,65]. This procedure of recovering the real spectral components and concentrations (titration), namely calculating the matrices D and C from the matrices U, S and V implies that one makes some reasonable assumptions about the kinetics of the system under consideration, and then finds the transformation which fits the rotated vectors of the V-matrix (so called "scores") to the imposed model. After making the decision about the rank of the data, the next step is to postulate a model for the kinetics

of the reaction. This will, in turn, provide the means for recovery of the pure spectral components and the equilibrium constants. From the above described analysis of the rank of our spectroscopic data, it follows that there are three distinguishable molecular species in pure water. The postulation of thermodynamic equilibrium among all three species leads to a set of equations for the concentrations C_j of different species :

$$C_2 = C_1 \exp(-\Delta H_{12}/RT + \Delta S_2)$$

$$C_3 = C_1 \exp(-\Delta H_{13}/RT + \Delta S_3) \tag{45}$$

$$C_1 + C_2 + C_3 = 1$$

where the ΔH_{ij} and ΔS_j are the relevant enthalpies and entropies of the imposed reaction. The equilibrium constants are: $K_1 = C_2/C_1$, $K_2 = C_1/C_3$, $K_3 = C_2/C_3 = K_1 K_2$, and $\log(K_j)$ versus reciprocal temperatures $1/T$ are linear functions. Under these assumptions we can rotate the titration eigenvectors from V with the aid of 3 by 3 matrix T, in order to yield the equation:

$$V' = TC \tag{46}$$

Comparing Equations 42 and 44 we can derive the matrix D, containing the pure spectral components,

$$D = UST \tag{47}$$

The problem of calculating the transformation matrix T is central to this nonlinear regression procedure. We used the Nelder-Mead simplex optimization algorithm, that solved Equation 46 with four unknown nonlinear parameters ΔH_{12}, ΔH_{13}, ΔS_2 and ΔS_3, and nine unknown linear parameters, that actually determine the matrix T, in the least square sense. The routine returns the unknown parameters and the norm of the difference vector between the functions C_j from Equation 45 and rotated vectors V, that serves as a measure for this nonlinear fitting. The original "scores" from the V matrix and rotated to the real concentration C_j are depicted in Figures 46 and 47 respectively. Now after

calculating the **T** matrix we can recover the pure spectral components with the aid of Equation 47. Three spectral components shown in the Figure 48 were recovered with the above described nonlinear regression technique. Figure 49 shows the spectral components recovered from different data, obtained from different spectrometers, and demonstrates the level of confidence in recovering the spectral components with the chemical regression. The returned enthalpies for the reactions ΔH_{ij} are: $\Delta H_{12}=2.6$ kcal/mol, $\Delta H_{31}=3.6$ kcal/mol. The first one corresponds to the well known value of the heat of hydrogen bond formation in pure water. The latter is probably the heat of formation of the intermediate form of hydrogen bonded specie in water. This dependence is very sensitive to the recovered nonlinear parameters and should viewed qualitatively rather than reflecting real entropies and enthalpies of the hydrogen bond formation. Stability analysis of this nonlinear regression procedure have been made, by adding artificial random noise to the experimental spectral data. The routine of chemical regression demonstrates high stability in recovering spectral components but fairly poor reproducibility for concentrations. This feature of chemical regression is not unknown but has to be understand in terms of illposed problems[60]. The values cited above correspond to the spectral components depicted in Figure 48 and are probably not very reliable, but the shape of the recovered spectral components are reproducible for different sets of data and demonstrates high stability upon small random perturbation of the initial spectral data. Using pseudoinverse operator and recovered spectral components we were able to calculate the experimental concentration matrix $\mathbf{C}_{exp}$ (closed circles in Figure 47) from the matrix **D**.

$$\mathbf{C}_{exp} = pinv(D)A \tag{48}$$

pinv in Equation 48 denotes operation of pseudoinversion, according to definition **pinv(A)A** = **I**, were **I** is a unity matrix.

The spectrum which belongs to the specie which dominates at high temperature is the most blue shifted and narrowest of the spectral components, indicating the least amount of hydrogen bonding. The spectrum from the specie which exist through the range of temperatures is intermediate in spectral shift and width. The low temperature specie is the most red shifted and broadest consistent with a high degree of hydrogen bonding, and reflects the statistical nature of the different length of hydrogen bonds in water clusters. Thus the evolution of the spectra is in agreement with the many studies of effect of hydrogen bonding on spectra.

Our analysis of the temperature dependent spectra of the 960 nm combination tone peak demonstrates that the three spectrally and structurally distinguishable species are needed to explain the evolution of the spectra within the framework of a simple thermodynamic model. The attempt to deconvolve the spectra imposing a two species model (bonded and nonbonded structures, being in thermodynamic equilibrium) derives unrealistic spectra of the components and thermodynamic parameters. It seems very probable that more precise spectral data and absolute temperature measurements would lead us to reconsideration of the minimal number of species needed and consequently the imposed thermodynamic model. Such studies would demand a substantial improvement of the spectroscopic apparatus and probably a more diverse approach to this problem, exploiting different methods of CARS spectroscopy of Raman-active vibrational transitions or more precise investigation of lower overtones in the NIR range of water spectra. Such studies are complicated by the high level of noise due to the high extinction coefficient and problems of temperature and flow control inside very thin cells.

CONCLUSIONS

In this study we, for the first time, applied the powerful technique of multivariate

statistics and nonlinear regression to the problem of water structure. Our findings support the mixture model of water with at least three species. For the first time, we recovered the pure spectra of these species from an imposed explicit physical model. Nevertheless, at this time we don't have a clear understanding of the physical nature of these species and the relevant energies of reactions. However, this model can be used as an analytical approach to the interpretation of water spectra and even for measuring the temperature of the water-containing samples. The obtained spectral components can be exploited for developing a statistical theory of hydrogen bonding in water and can be helpful in verification of the numerous theories[66,67] which try to calculate the shape of the absorption and Raman band in pure water. The pure components found from the temperature dependent spectra of pure water could be used for interpretation of the temperature dependence of the NIR spectra of human tissue and for improving of the quantitative prediction of the depth of burn wounds.

MONTE CARLO SIMULATION OF HETEROGENEOUS TISSUE

The study of light propagation and reflection from tissue is central to many medical and biomedical applications of light. For diagnostic purposes, such as noninvasive optical spectroscopy, the light that is diffusely reflected from or transmitted through the tissue may be measured to probe the metabolic, physiologic, or possibly the structural status of the tissue. In previous sections of this report, we stated that Beer's laws and multivariate were used to analyze reflection of light from tissue, a medium in which scattering and absorption occur. Beer's Law is particularly troublesome when both scattering and absorption are strong. Any further improvement of our predictions based on a multivariate statistics will depend on a proper algorithm of reflectance spectra evaluation, involving subtraction of temperature dependent water spectra and comparison of the transmittance in vivo and reflectance spectra of oxy - and deoxy- hemoglobin.

The problem of the deconvolution of the remittance spectra of tissue have been discussed in many papers.[68] It is well known that changes in the distribution of scattered light in the skin that result from variations in the hematocrit and volume fraction of blood contained in the dermis may affect the calibration of the instruments used in pulse blood oximetry or burn wound evaluation. It could be extremely difficult to perform controlled experimental studies of these effects, especially in the frequency domain. Therefore mathematical models and computer simulations of light propagation and diffusive reflection from tissue are essential to guide current applications and to promote further developments in biomedical optics.

The three most common mathematical approaches to the study of light propagation in tissue are based on the Kubelka-Munk, random walk, and radiative-transport model. Most of the studies have been done for the semi-infinite homogeneous model of tissue, and for fixed scattering parameters and a given

wavelength of light. The importance of modeling in the wide wavelength domain follows from our simple simulations made for continuous homogeneous medium with the aid of analytical expressions obtained by Wilson.[69] We have used the spectra of oxy-, deoxy-, and met- hemoglobin obtained during our in vitro studies, and have calculated the extinction spectra that would be measured by our methods in tissue. The original and simulated spectra are shown in

Figure 50. Solid lines represent original spectra, and dashed lines represent simulated tissue spectra.

Even this simplistic approach shows the significant difference in spectral shape, and emphasizes the importance of evaluating reflectance spectra properly in order to improve our quantitative interpretation.

Our plan for research included following steps:

1. Development of a working program for simulations of photon transport in a random scattering heterogeneous medium with inclusions (i.e., veins) with different scattering and absorption parameters.

2. Numerical simulations of light distribution inside and outside homogeneous scattering medium for a fixed wavelength and for a wide range of wavelengths.

3. Comparison of our numerical simulations with the existing experimental and theoretical studies.

4. Numerical simulations of the reflected light distribution from the multilayer heterogeneous medium with inclusions for the wide wavelength range of visible and SW-NIR light (so-called "therapeutic window").

5. Numerical and theoretical studies of the pulse response from the heterogeneous media.

We were not able to fulfil this program because of the termination of funding, but

even the preliminary results appear promising and informative.

The basic principles of four different types of remittance spectrophotometry could be understood from Figure 51.[68] We developed a working program in FORTRAN language, that was able to run on different computers: VAX/VMS, IBM-6000/RS, and HP-6000. The program was able to simulate the random walk of photons in a scattering medium with inclusions taking into account such effects as internal reflection and refraction due to the different indices of refraction of tissue and air. Monte Carlo simulations that include effects of geometrical optics have not yet been discussed in any of the numerous published studies. We used as a guideline for our Monte Carlo simulations a model by Bonner[70]. Basic steps in the calculation of the single photon path are obvious from Figure 52. The term "weighting" in Figure 52 refers to the "intensity" of the photons, which decreases with path travelled according to the assumed absorption coefficients in the medium. The computer code in FORTRAN is listed in the Appendix B. The program was structured in several subroutines that made it flexible for fast changes of parameters, shape of the light source, and the number and shape of inclusions. The shape of inclusions could be given by algebraic equation or numerically. We used basically two types of light sources, point and a radial source with a homogeneous distribution of intensity. The typical number of inserted photons that gave a reproducible intensity distribution inside and outside the tissue was 100000. The simulations were time consuming. One run (for the fixed set of scattering parameters) took typically 6-8 hrs. on the VAX computer and 0.5 hours of CPU time on an IBM-6000 workstation with performance of 2-3 Mflops per second.

The model of the heterogeneous tissue with radial inclusions is shown in Figure 53. The results of the simulations were plotted as intensity contour lines. Figures 54-56 demonstrate the intensity distribution for a point light source just inside the homogeneous

medium for the case without inclusions, one radial inclusion, and two radial inclusions, respectively. The scattering parameters are shown on the plots. The intensity distributions for a radial source in the homogeneous medium without inclusions and with one radial inclusion are depicted in Figures 57-58. Figures 59-60 demonstrate the spatial and temporal behavior of the reflected light, corresponding to Figure 57.

Therefore, in this chapter we report an innovative computer code for Monte Carlo simulations of light remittance from heterogeneous media. Our results obtained over a comparably short period of time with comparably modest computer resources could be an impetus for further studies in this new and promising field of biomedical research.

BIBLIOGRAPHY

1.   Johnson, C.L.; O'Shaughnessy, E.J.; Ostergren, G. *Burn Management*, **1981**, Raven Press, N.Y., NY.

2.   Engrav, L.H.; Heimbach, D.M.; et. al. *J Trauma*, **1983**, *23*, 1001-1004.

3.   Heimbach, D.M.; Engrav. L.H. *Surgical Management of the Burn Wound*, **1984**, Raven Press, N.Y., NY, Ch.1.

4.   Godina, M.; Derganc, M.; Brcic, A. *Burns*, **1978**, *4*, 92-96.

5.   Panke, T.W.; McLeod, C.G. *Pathology of Thermal Injury: A Practical Approach*, **1985**, Grune & Stratton, N.Y., NY.

6.   Gürsu, K.G. *Burns*, **1978**, *4*, 97-103.

7.   Patey, D.H.; Scarff, R.W. *Brit J Surg*, **1944**, *32*, 32-35.

8.   Davies, M.R.Q.; Adendorff, D.; Rode, H.; van der Riet, R. leS. *Burns*, **1980**, *6*, 156-159.

9.   Bennett, J.E.; Dingman, R.O. *Plastic and Reconstructive Surgery*, **1957**, *20*, 261-272.

10.   Bauer, J.A.; Sauer, T. *Burns*, **1989**, *15*, 49-51.

11.   Cole, R.P; Jones, S.G.; Shakespeare, P.G. *Burns*, **1990**, *16(1)*, 60-63.

12.   Newman, P; Pollock, M.; Reid, W.J.; James, W.B. *Burns*, **1981**, *8*, 59-63.

13.   Bardakjian, V.B.; Kenney, J.G.; et. al. *J Burn Care Rehab*, **1988**, *9(1)*, 63-65.

14.   Green, M.; Holloway, G.A.; Heimbach, D.M. *J Burn Care Rehab*, **1988**, *9(1)*, 57-62.

15.   O'Reilly, T.J.; Spence, R.J.; Taylor, R.M.; Scheulen, J.J. *J Burn Care Rehab*, **1989**, *10(1)*, 1-6.

16.   Anselmo, V.J.; Zawacki, B.E. *Proceedings of the Society of Photo-Optical Instrumentation Engineers, Quantitative Imagery in the Biomedical Sciences -- II*, **1973**, *80*, 181.

17.   Anselmo, V.J.; Zawacki, B.E. *Annals of Biomedical Engineering*, **1977**, *5*, 179-193.

18.   Heimbach, D.M.; Afromowitz, M.A.; Engrav, L.H.; Marvin, J.A; Perry,B. *J Trauma*, **1984**, *24(5)*, 373-378.

19. Afromowitz, M.A.; Van Liew, G.S.; Heimbach, D.M. *IEEE*, **1987**, *BME-34(2)*, 114-126.

20. Afromowitz, M.A.; Callis, J.B.; Heimbach, D.M.; DeSoto, L.A.; Norton, M.K. *IEEE*, **1988**, *BME-35(10)*, 842-849.

21. DeSoto, L.A. *A Burn Depth Imaging System* **1986**, University of Washington M.S. thesis.

22. Moore, M.K *A Clinical Evaluation of the Imaging Burn Depth Indicator*, **1987**, University of Washington, MS thesis.

23. Van Liew, G.S. *A Statistical and Optical Analysis of Light Reflectances of Burn Injured Skin*, **1984**, University of Washington, M.S. thesis.

24. Nelcor Inc., Hayward, CA.

25. Shapiro, B.A.; Cane, R.D. *Crit Care Med*, **1989**, *17*, 573-581.

26. Wyatt, J.S.; Cope, M.; et.al. *Lancet*, **1986**, 1063-66.

27. Cope, M.; Delpy, D.T. *Med & Biol Eng & Comput*, **1988**, *26*, 289-294.

28. Barbour, R. *Instrumentation Research*, **1985**, *March*, 59-64.

29. Hampson, N.B.; Piantadosi, C.A. *J Appl Physiol*, **1988**, *64(6)*, 2449-2457.

30. *Near-Infrared Technology in the Agricultural and Food Industries*, **1987**, William, P.; Norris, K., Eds.; American Association of Cereal Chemists, St.Paul, MN.

31. Stark, E.; Luchtir, K.; Margoshes, M. *Appl Spec Rev*, **1986**, *22(4)*, 335-399.

32. MATLAB, The Math Works, Inc., Cochituate Place, 24 Prime Park Way, Natick, MA 01760, 1990.

33. Hampson, N.B.; Piantadosi, C.A. *J Appl Physiol* **1988**, *64(6)*, 2449-2457.

34 LT Industries, __, MD.

35. Strang, G. *Linear Algebra and Its Applications* **1980**, Academic Press: Florida, 137-145.

36. Thomas. E.V.; Haaland, D.M. *Annal. Chem.* **1990**, *62*, 1091-1099.

37. Brown, C.W.; Lynch, P.F.; Obremski, R.J.; Lavery, D.S. *Anal. Chem.* **1982**, *54*, 1472-

1479.

38.   Haaland, D.M.; Thomas, E.V. *Anal. Chem.* **1988**, *60*, 1193-1202.

39.   Wold, S.; Esbensen, K.; Geladi, P. *Chemom Intell Lab Syst* **1987**, *2*, 37-52.

40.   Sharaf, M.A.; Illman, D.L.; Kowalski, B.R. *Chemometrics* **1986**, John Wiley & Sons: New York.

41.   Balkenhol, M.B. *NIR and Visible Spectroscopy of Irregular Solids*, **1992**, University of Washington, PhD thesis.

42.   "Pirouette", Infometrics, Seattle, WA.

43.   Afromowitz, M.A.; Callis, J.D. *Spectroscopy of Burn Wounds* **1991**, Annual report to the U.S. Army Medical Research & Development Command, Contract #DAMD17-88-C-8125.

44.   *Water, A Comprehensive Treatise*, v.7; Franks F.; Ed.; Plenum: N.Y.,1981.

45.   *Structure of Water and Aqueous Solutions*; Luck Ed.; Verlag Chemie and Physik Verlag, Weinheim/Bergstr, 1974.

46.   Suhrmann, R.; Breyer, F. *Z. Physik. Chem.* **1933** *B20*, 17.

47.   Buijs, K.; Choppin, G. R. *J. Chem. Phys.* **1963**, *39*, 2035.

48.   Choppin, G. R.; Buijs, K. *J. Chem. Phys.* **1963**, *39*, 2042.

49.   Choppin, G. R.; Violante, M. R. *J. Chem. Phys.* **1971**, *56*, 590.

50.   Paquette, J.; Jolicoeur, C. *J. Solution. Chem.* **1977**, *6*, 403.

51.   Nemethy, G.; Sheraga, H. A. *J. Chem. Phys.* **1964**, *41*, 680.

52.   Senior, W. A.; Vand, V. *J. Chem. Phys.* **1965**, *43*, 1869.

53.   Eisenberg D.; Kauzmann, W. *The Structure and Properties of Water*; Oxford Univ.: N.Y. and Oxford, 1969.

54.   *Water and Aqueous Solutions: Structure, Thermodynamics, and Transport Process*; Horne, E.A., Ed. John Wiley & Sons: N.Y.,London, Sydney, Toronto, 1972.

55.   Hubner, W; Mantsch, H. H.; Casal, H. L. *Appl.Spectrosc.* **1990**, *44*, 732.

56.   Inoue, A.; Kojima, T.; Taniguchi, Y; Suzuki, K. *J. Solution Chem.* **1984**, *13*, 811.

57.   Inoue, A.; Kojima, T.; Taniguchi, Y; Suzuki, K. *J. Solution Chem.* **1987**, *16*, 727.

58.   Fornes, V.; Chaussidon, J. *J.Chem.Phys.* **1978**, *68*, 4667.

59.   Lawton, W. H.; Sylvestre, E. A. *Technometrics.* **1971**, *13*, 617.

60.   Sylvestre, E. A.;Lawton, W. H.; Maggio, M.S. *Technometrics.***1974**, *16*,353.

61.   Mayes D.M.; Callis, J.B. *Appl.Spectr.* **1989**, *43*, 27.

62.   Sharaf, M. A.; Illman, D.L.; Kowallski, B.R. *Chemometrics*; John Wiley & Sons; N.Y, 1986.

63.   Maeder, M. *Anal.Chem.* **1987**, *59*, 52.

64.   Shrager, R.I.; Hendler, R. W. *Annal.Chem.* **1982**, *54*, 1147.

65.   Shrager, R. I. *SIAM J.Alg.Disc. Meth.* **1984**, *5*, 351.

66.   Coker, D. F.; Watts R. O. *J.Phys.Chem.* **1987**, *91*, 2513.

67.   Reimers, J. R.; Watts, R. O. *Chem.Phys.* **1984**, *85*, 83.

68.   B. C. Wilson, B.C.; Jacques, S.L. *IEEE Journal of Quantum Electronics*, **1990**, *26*, 2186-2199.

69.   Wilson, B.C.; Adam, G. *Medical Physics* **1983**, *10*, 824-830.

70.   Bonner, R.F.; Nossal, R.; Havlin, S.; Weiss, G.H. *JOSA A*, **1987**, *4*, 423-432.

TABLE I.

Table of Assignments.

1764	Fat	CH_2 stretch, 1st overtone
1731	Fat	CH_2 stretch, 1st overtone
1728	Collagen	
1708	Fat	CH_3 stretch, 1st overtone
1689	Collagen	
1460	Water (0th derivative)	OH stretch, 1st overtone
1400	Water (2nd derivative)	
1275	Collagen?	
1213	Fat	CH_3 stretch, 2nd overtone
1189	Fat	CH_3 stretch, 2nd overtone
1188	Protein in muscle tissue	
1153	Water	OH combination
1038	Fat	CH_2 combination
1014	Fat	CH_3 combination
958	Water	OH stretch, 2nd overtone
929	Fat	CH_2 stretch, 3rd overtone
760	Deoxyhemoglobin	
576	Oxyhemoglobin	
555	Deoxyhemoglobin	
541	Oxyhemoglobin	

Spectra of Hemoglobin
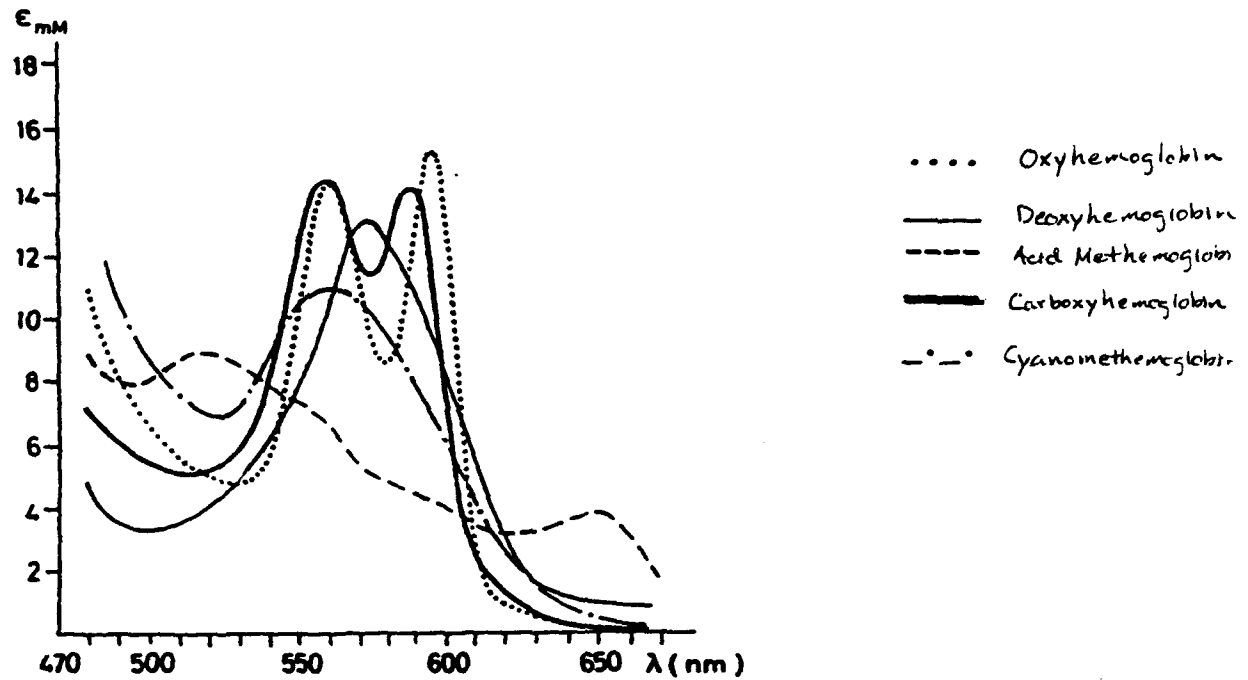
Figure 1a: Visible Spectra of Hemoglobin Derivatives
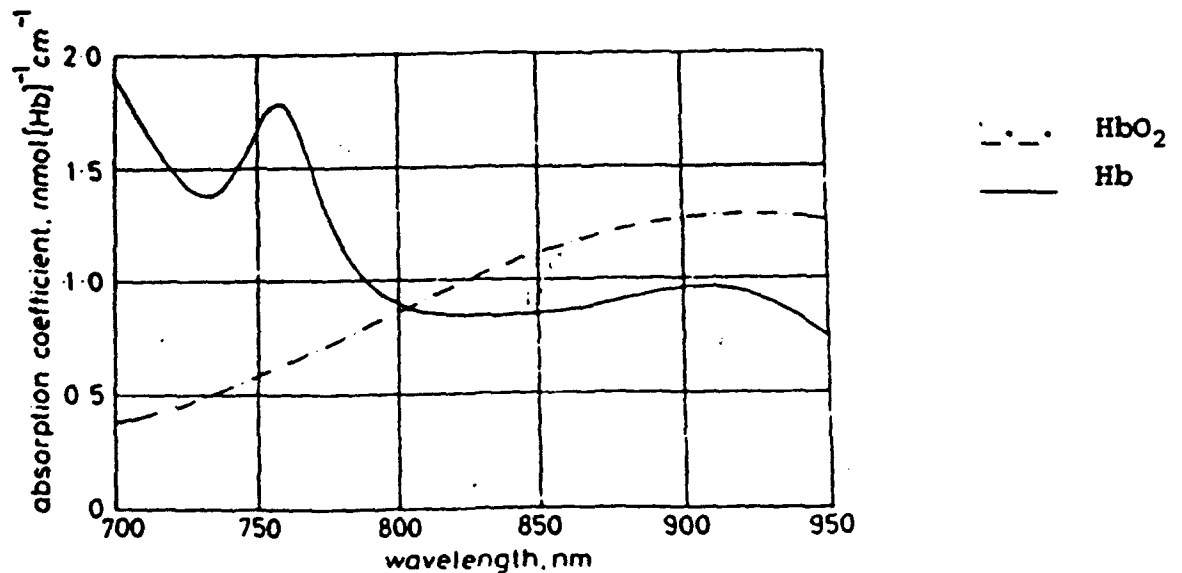
Figure 1b: Short-wave Near-infrared Spectra of Hemoglobin

Instrumentation

Figure 2

Water

Second Derivative
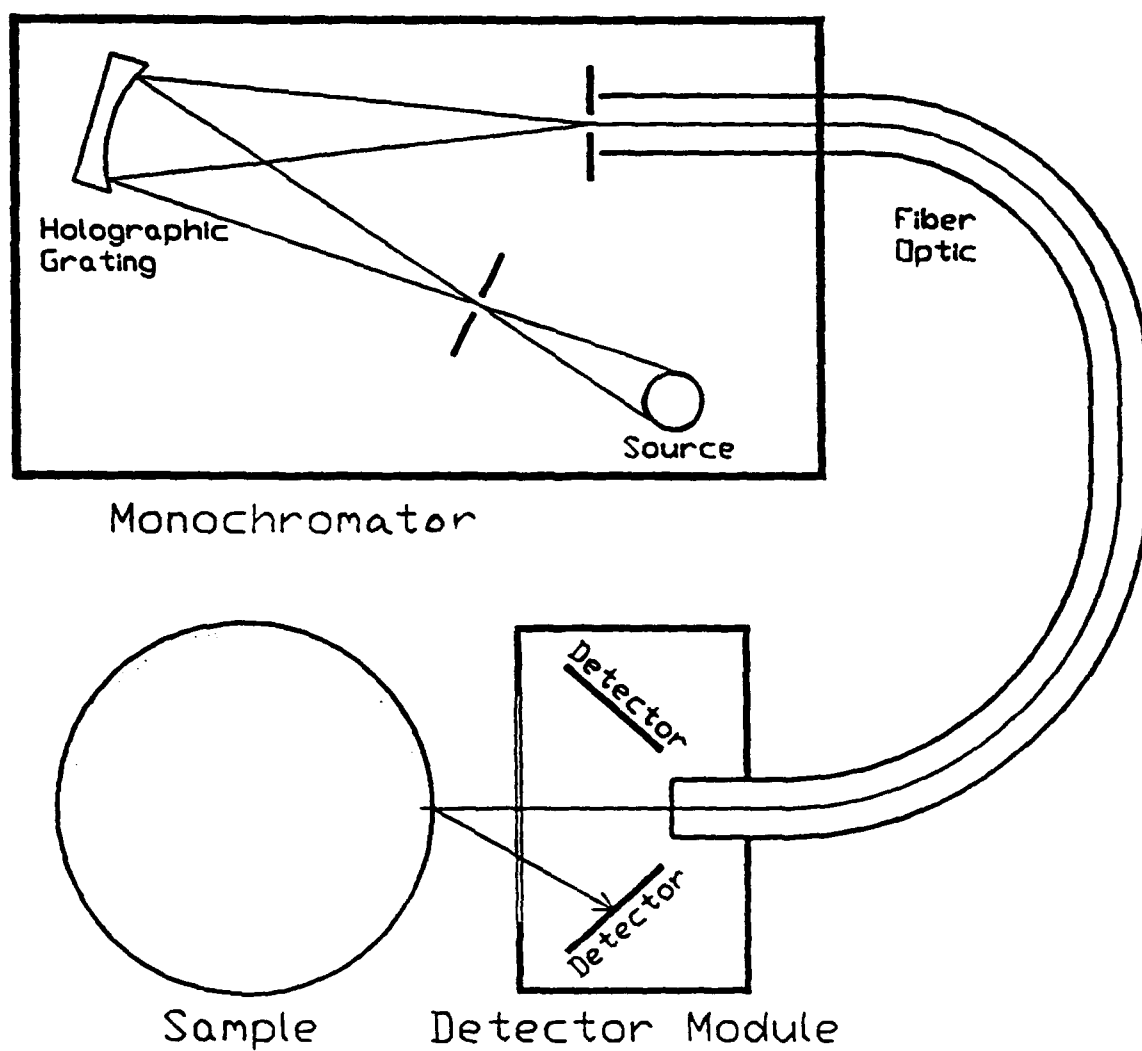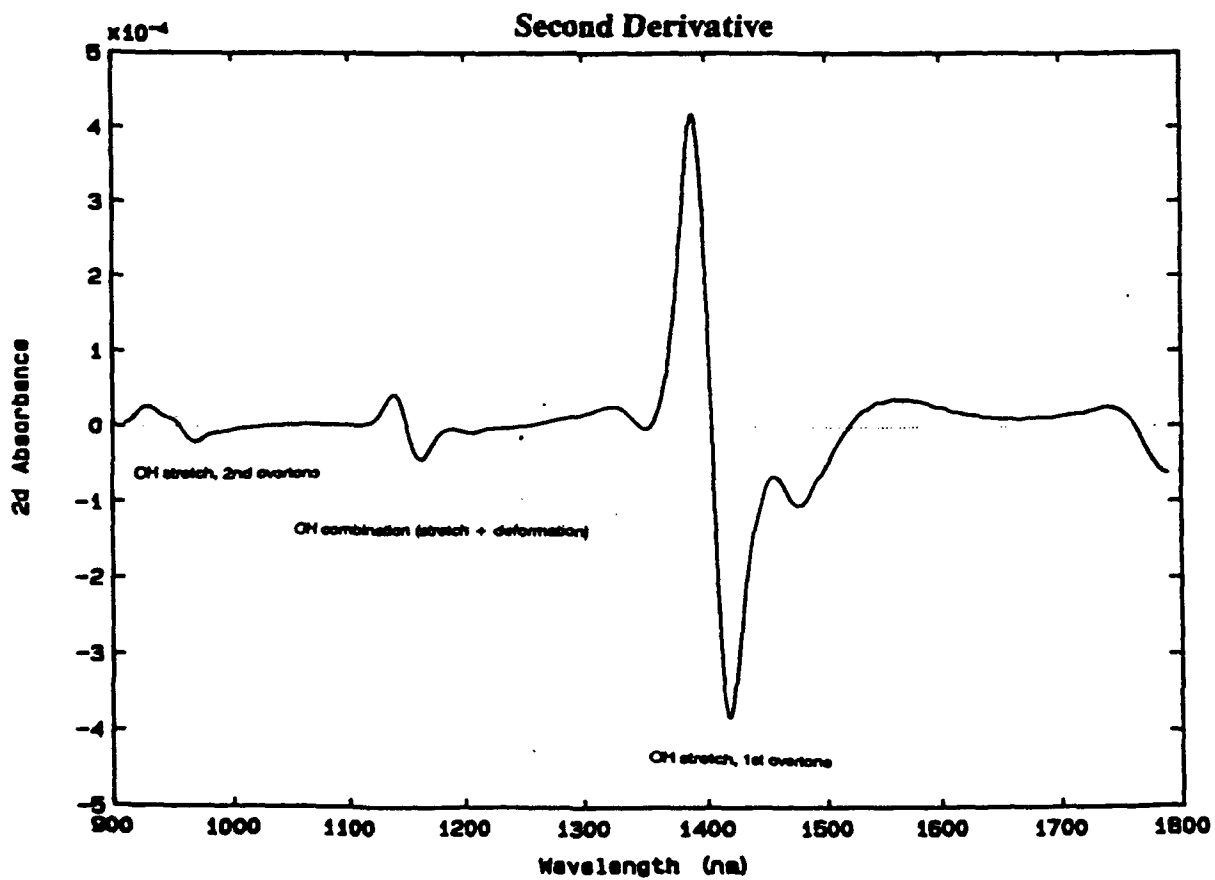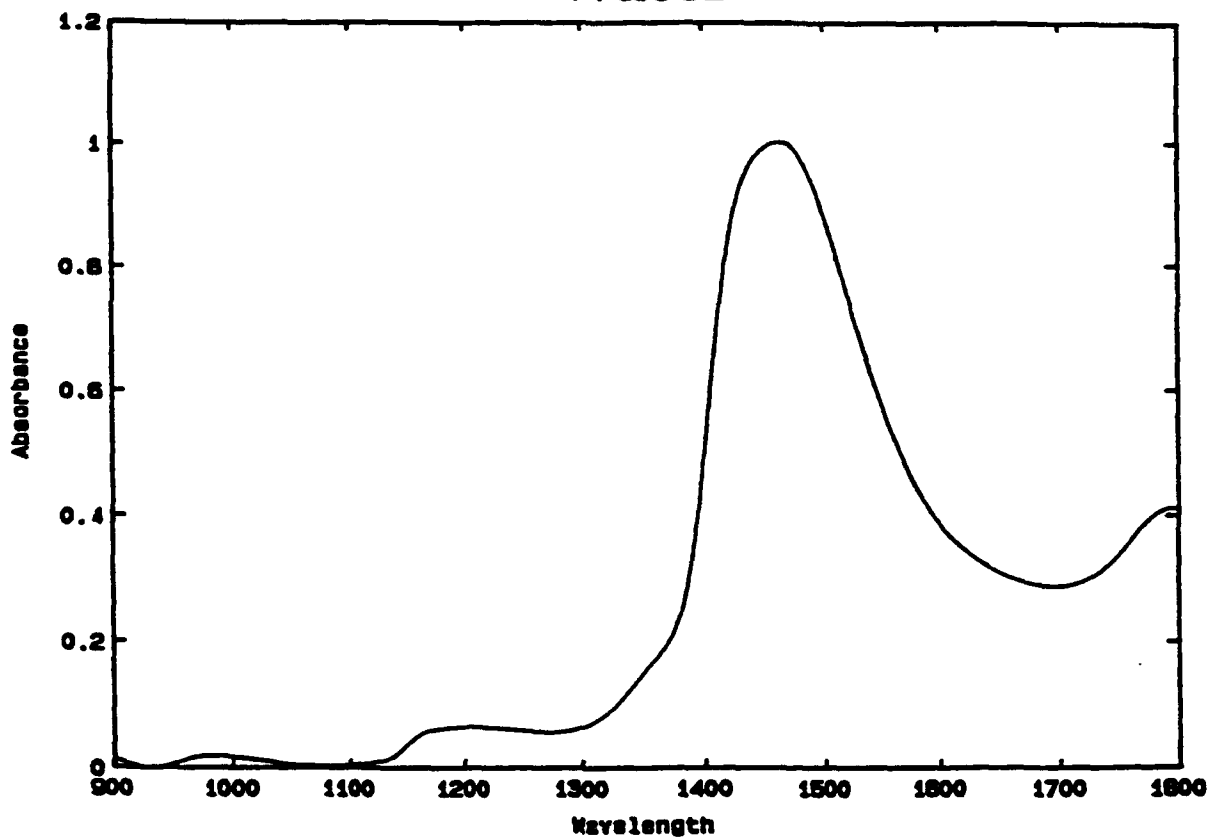
Figure 3

Mineral Oil

Figure 4

Collagen

Second Derivative
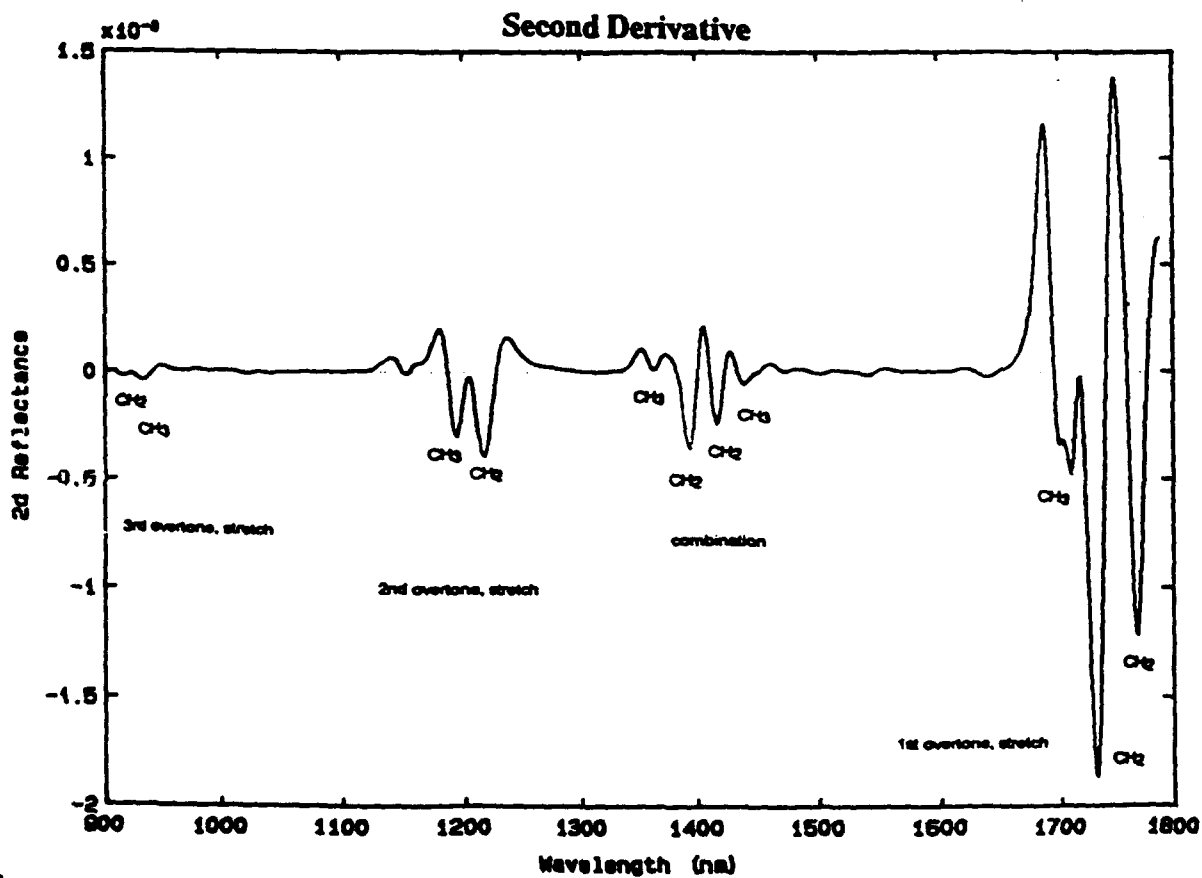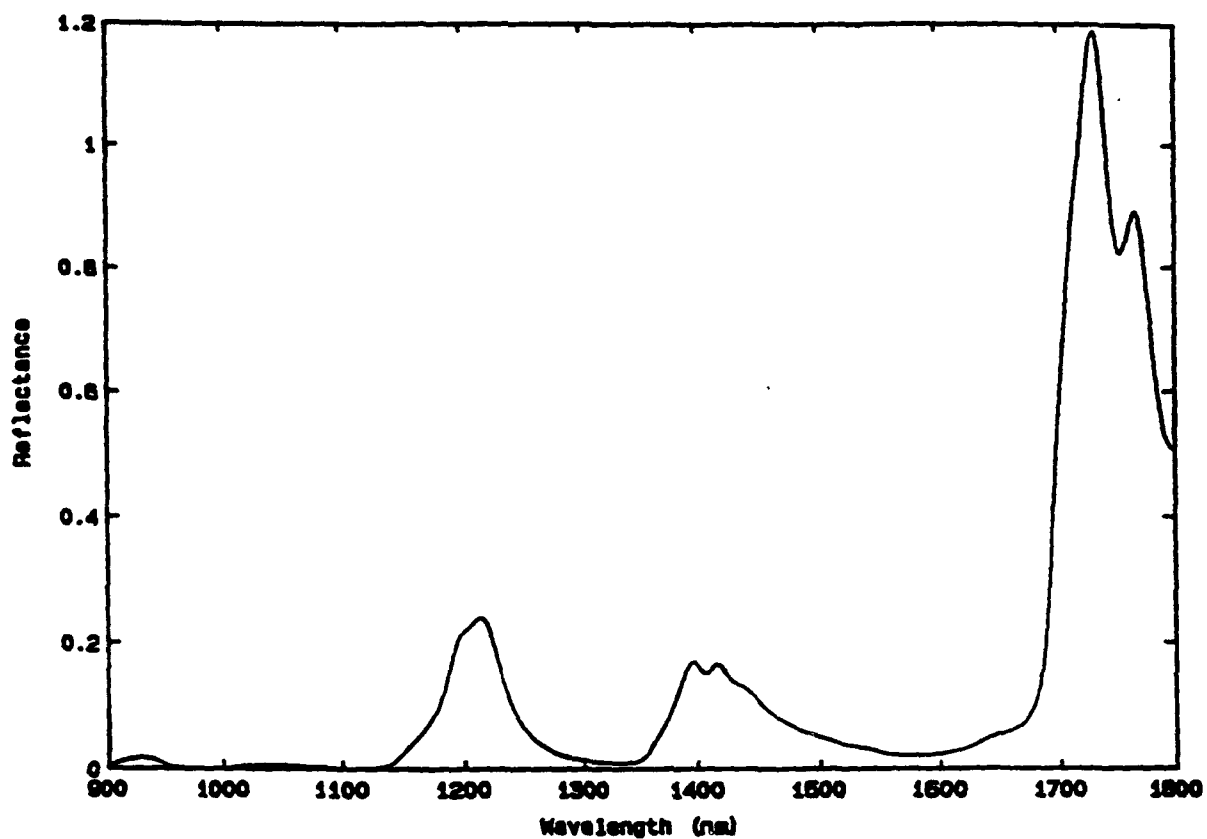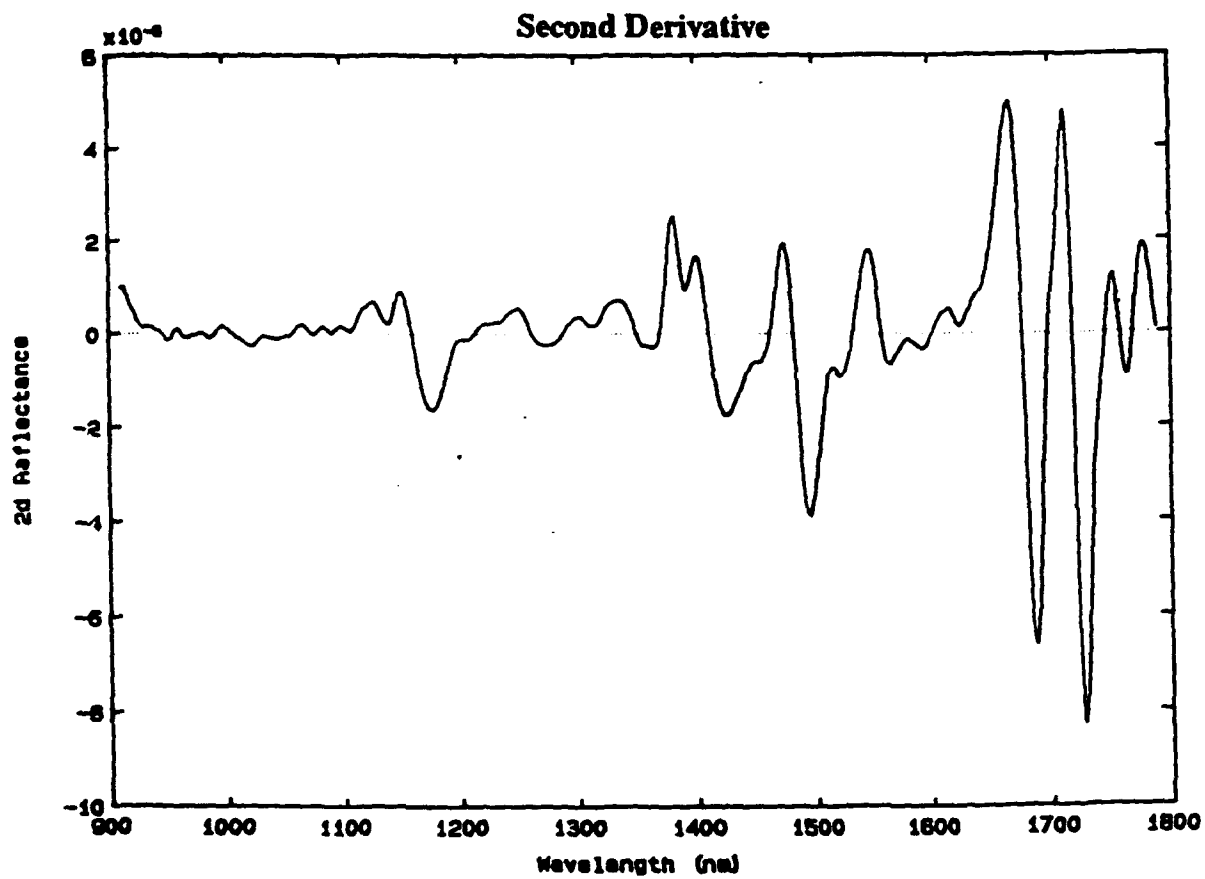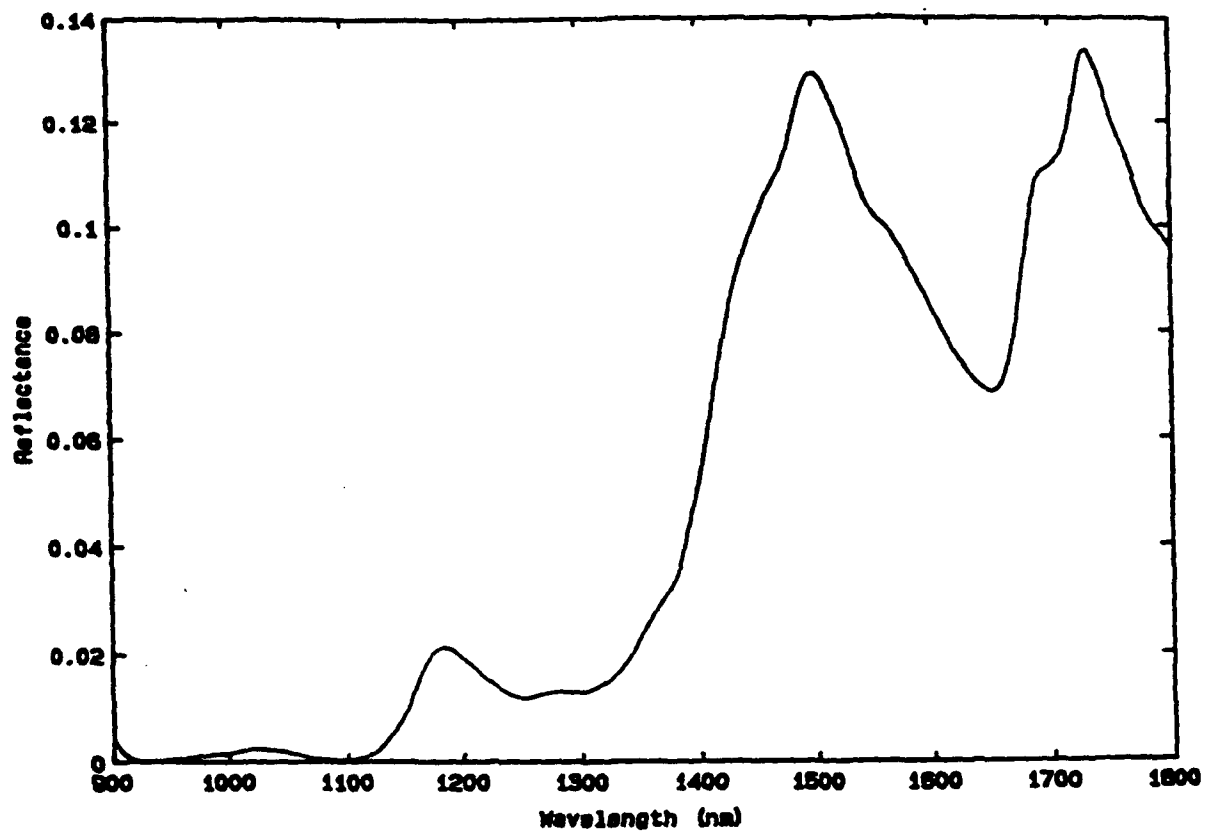
Figure 5

Water and Hemoglobin

Absorbance vs. Wavelength (nm)
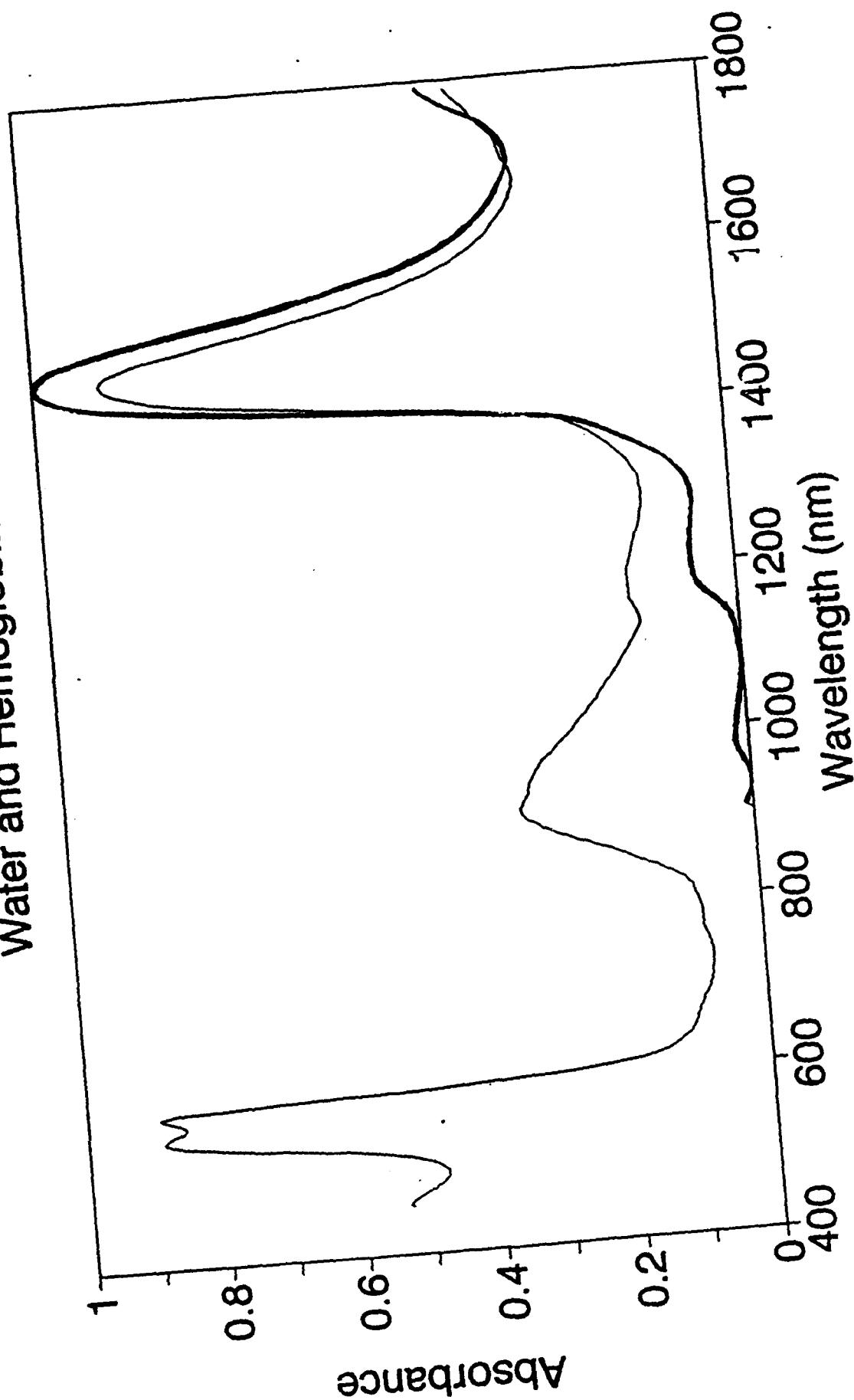
— Water   — Venous blood

Figure 6

Fat

Second Derivative
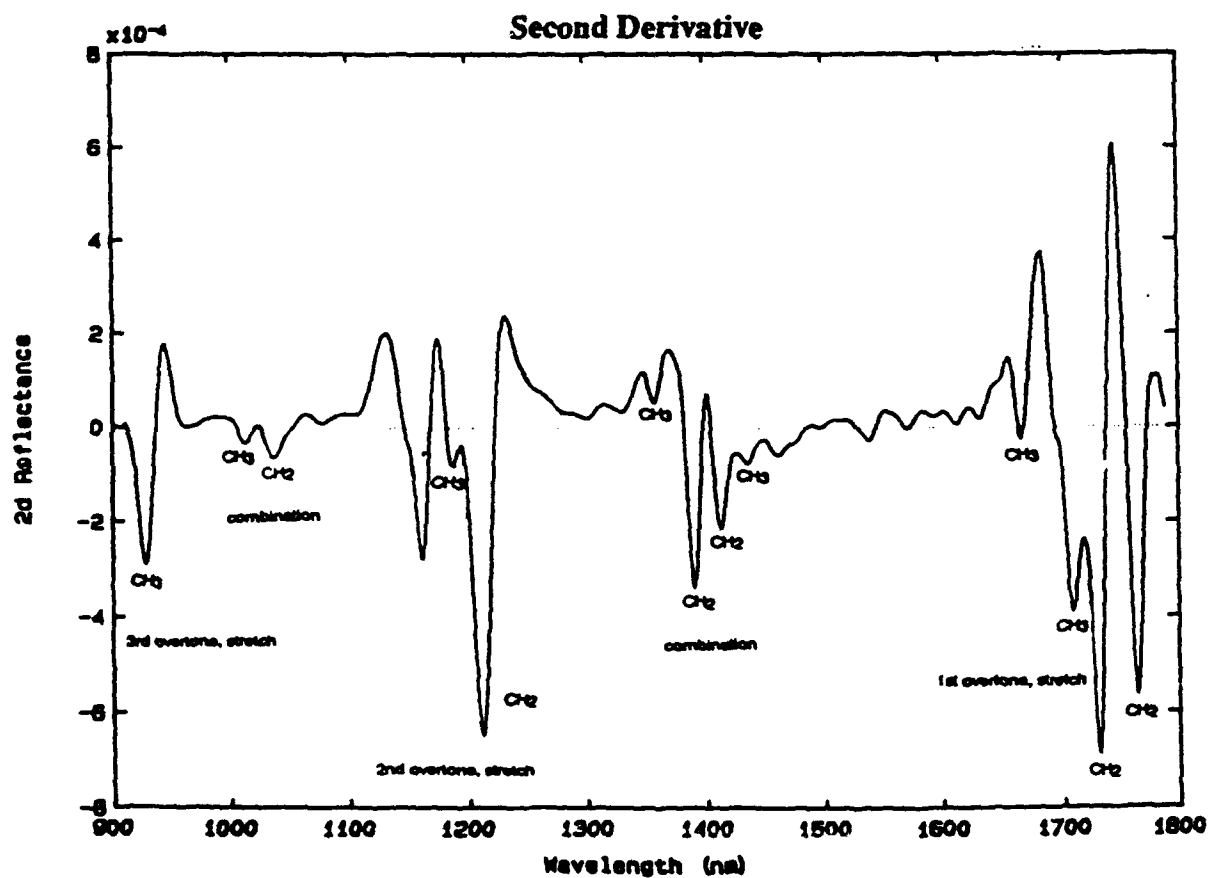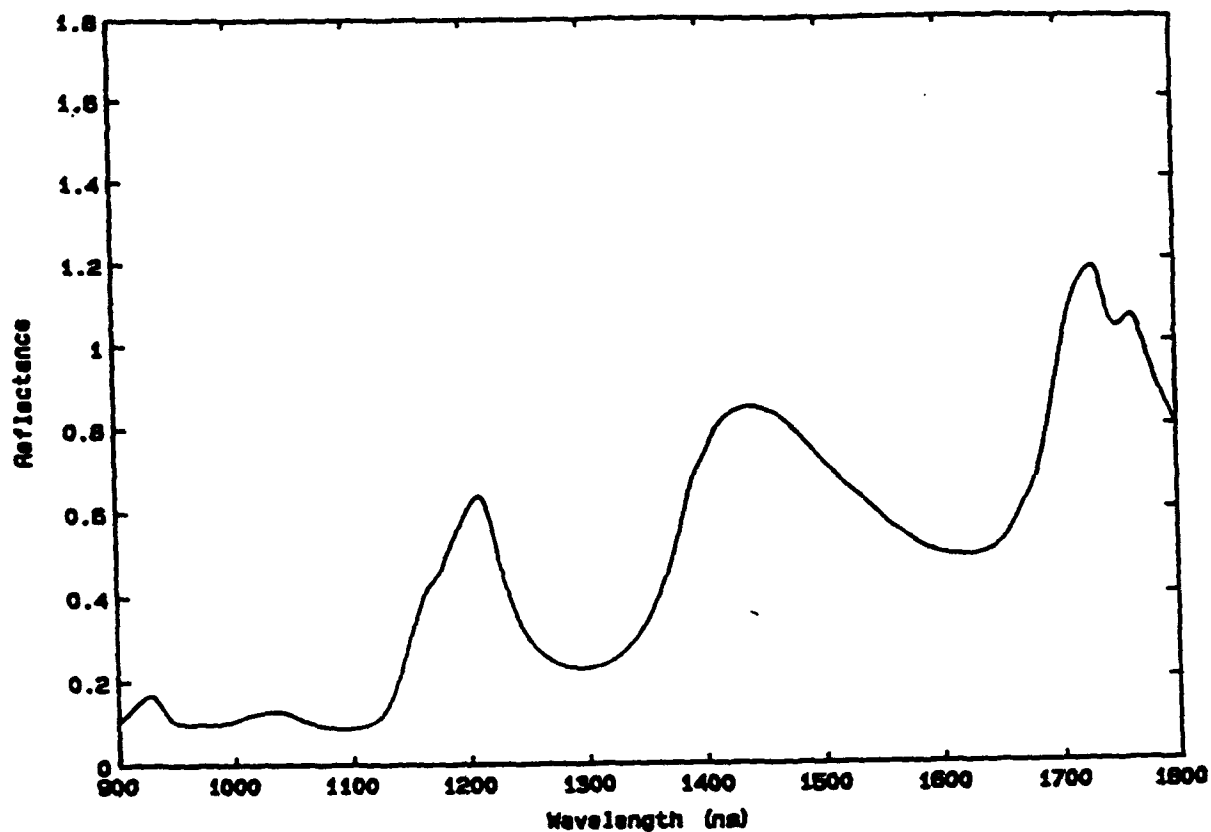
Figure 7

Muscle Tissue
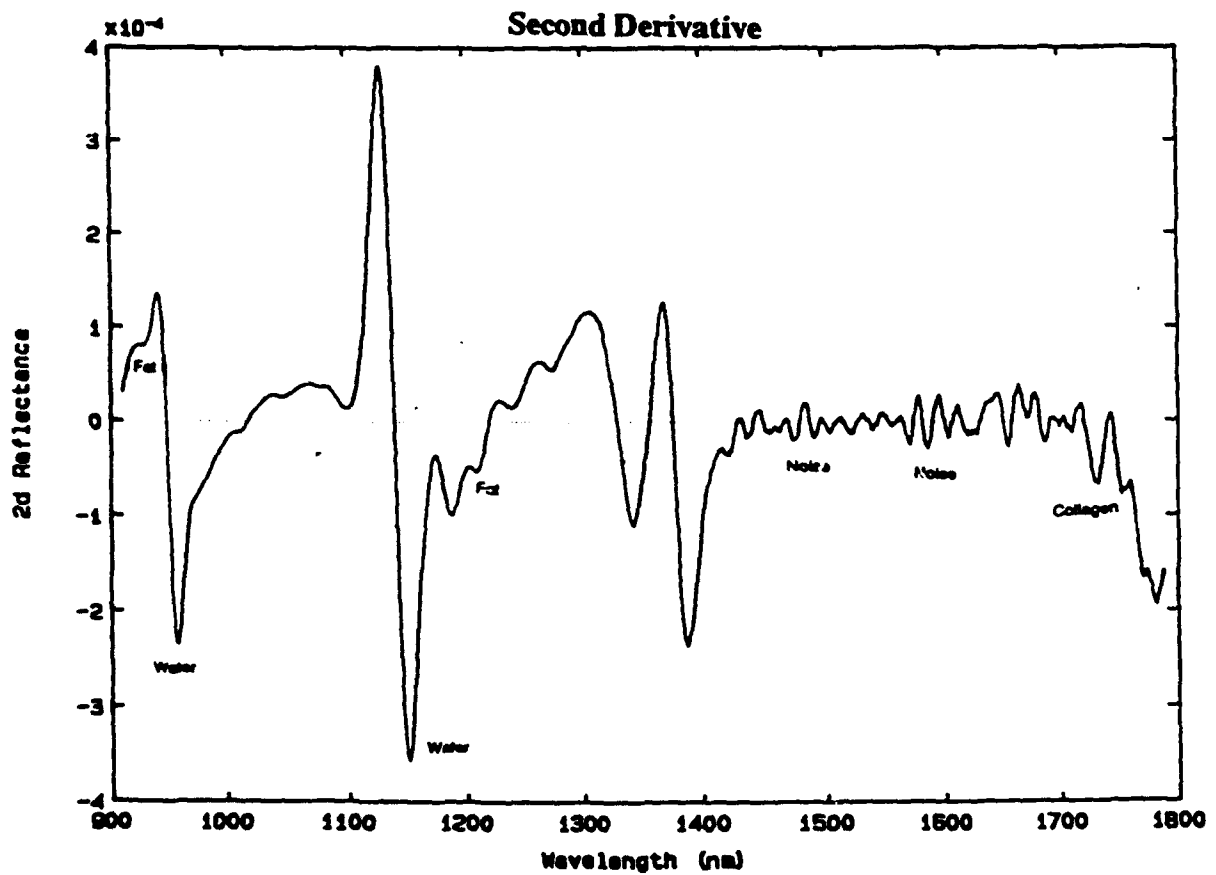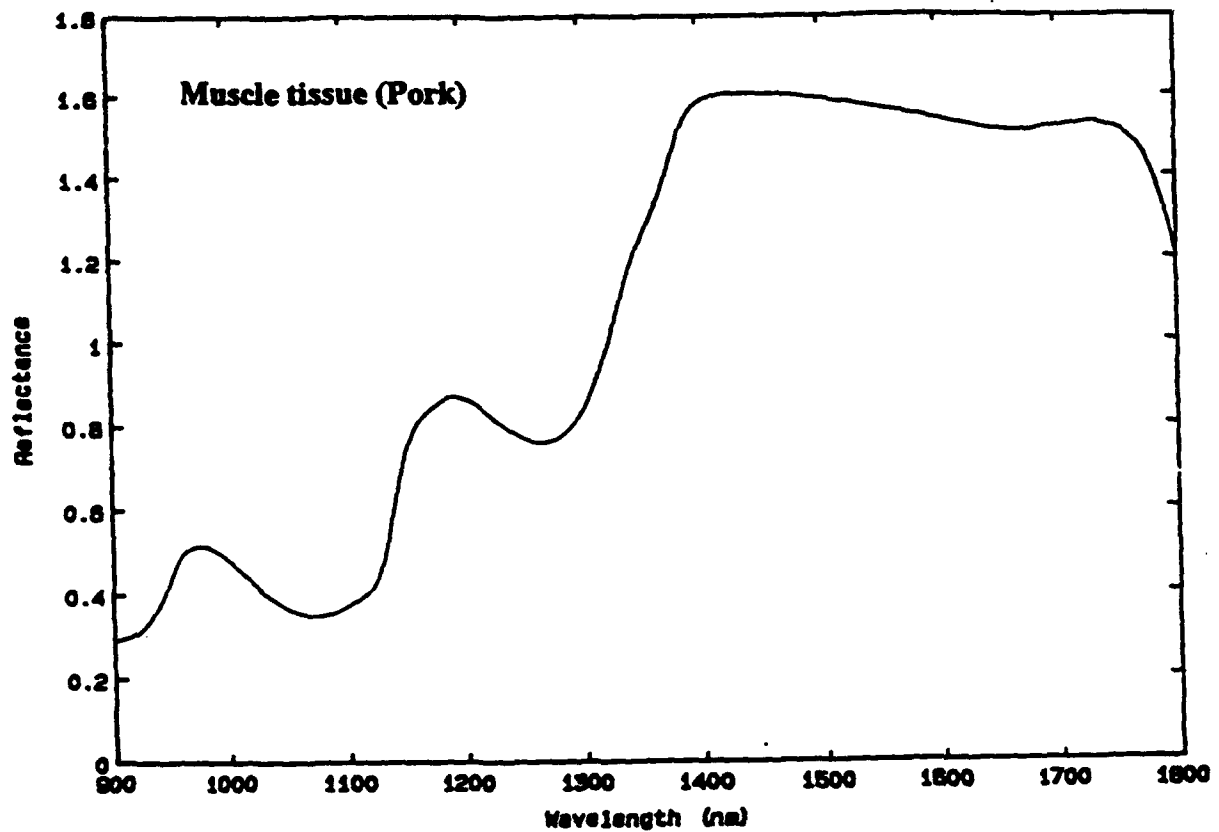
Figure 8

Tendon
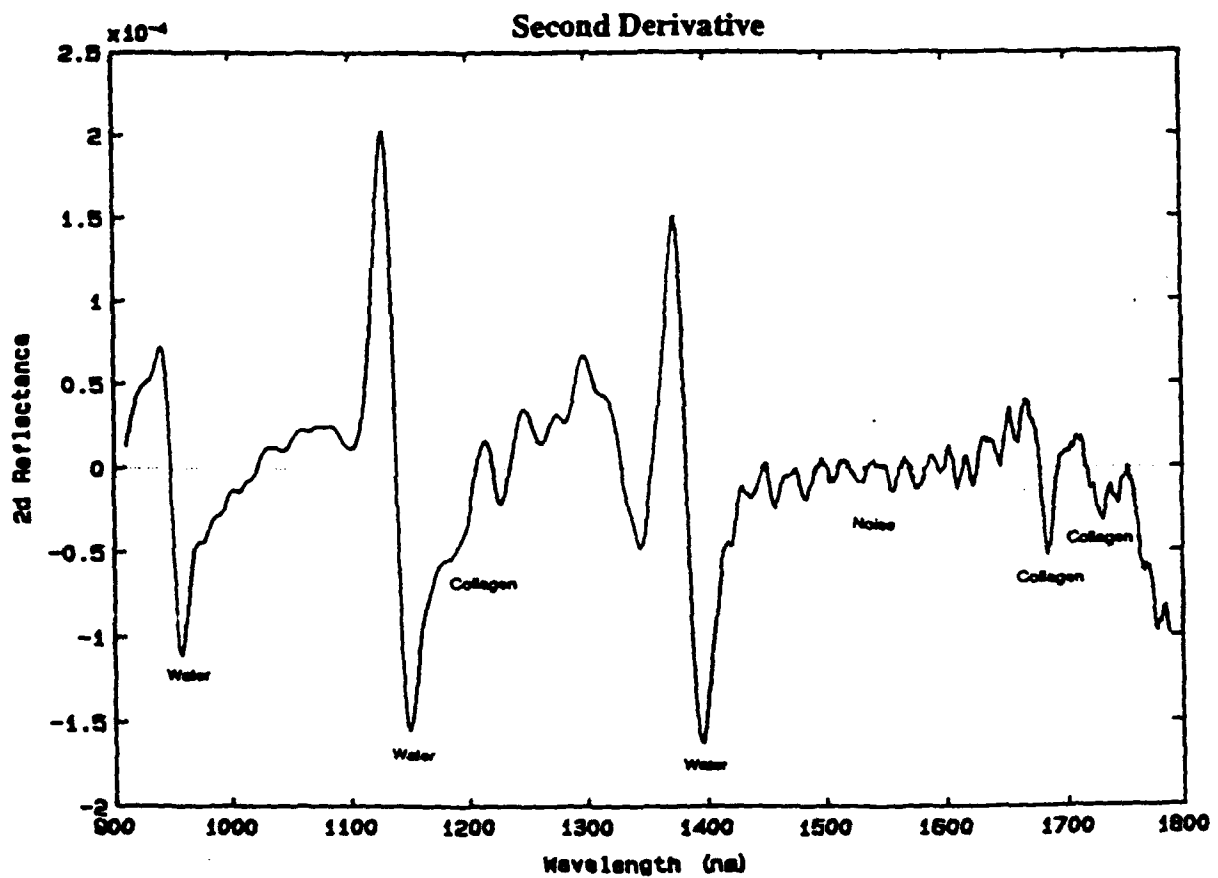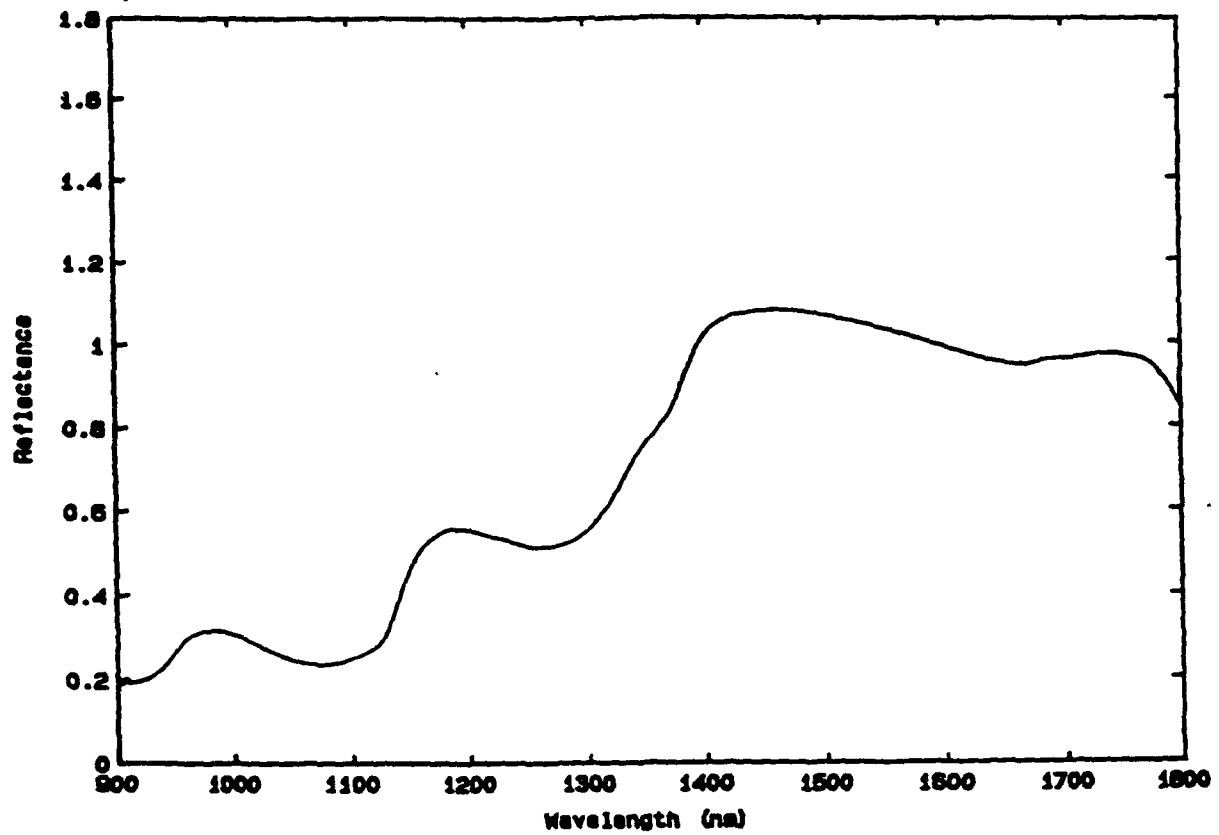
Figure 9

Skin in vivo, Human
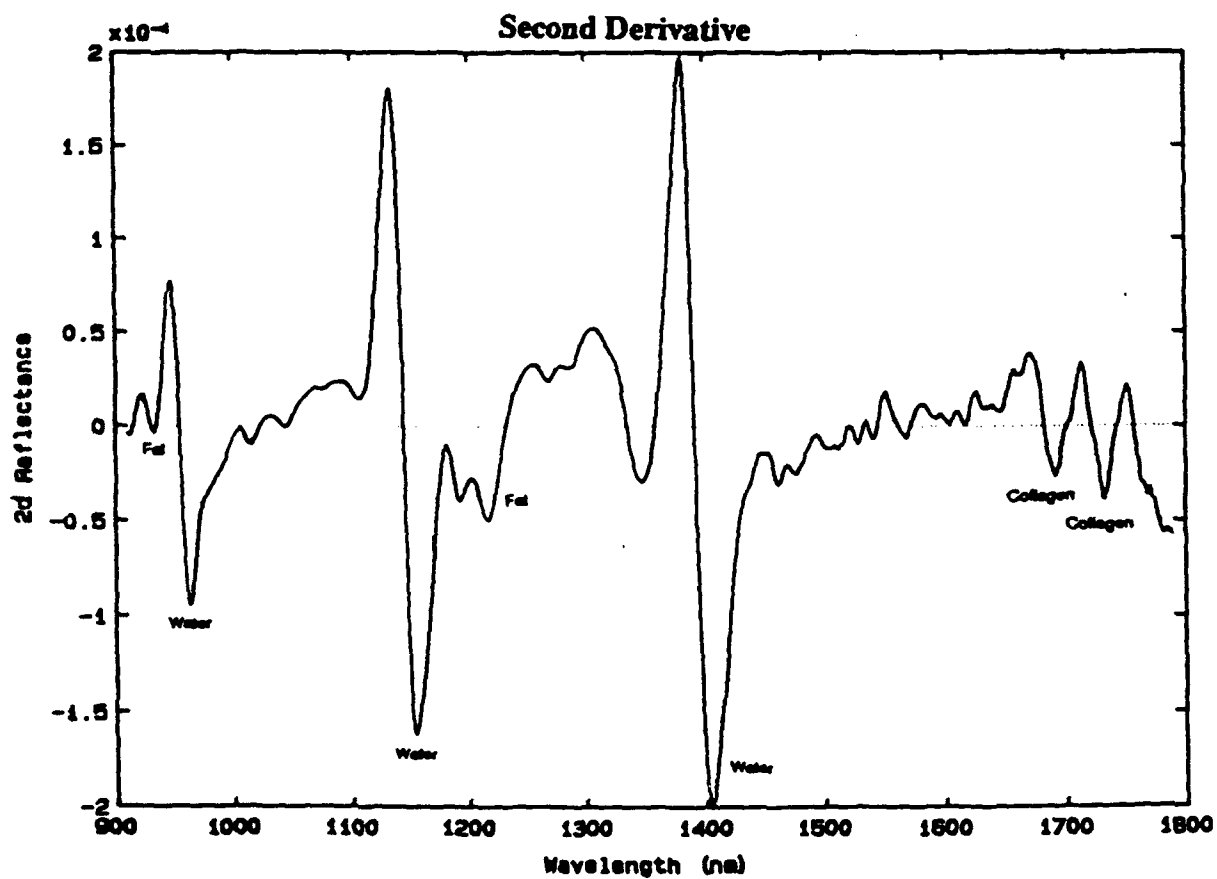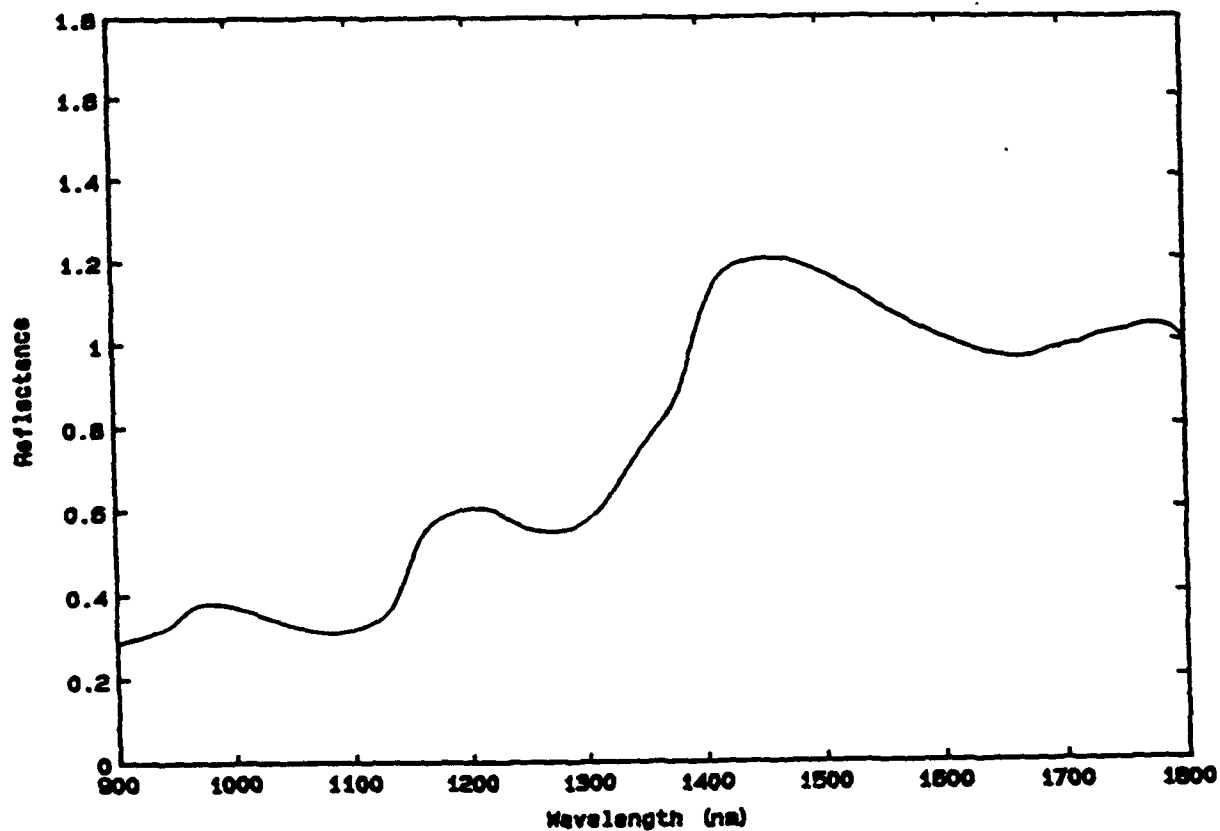
Figure 10

Skin Temparature
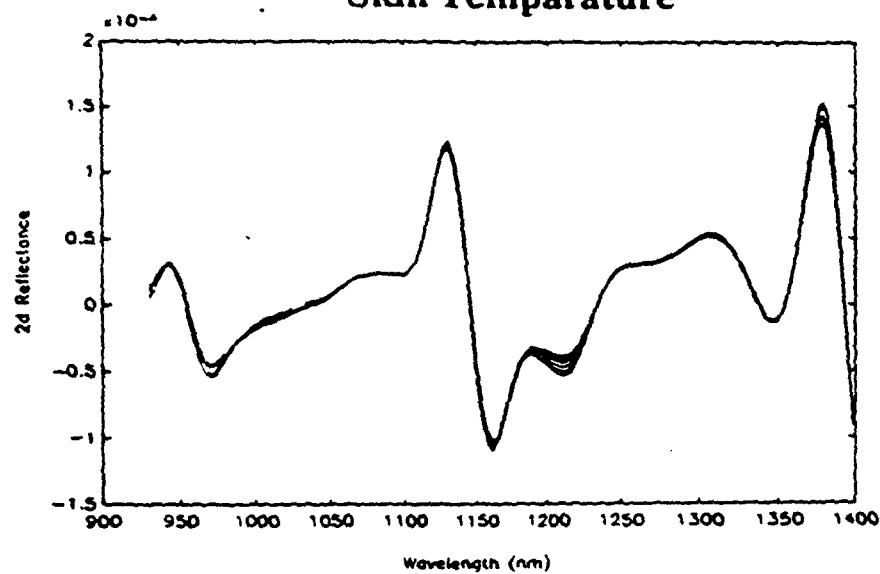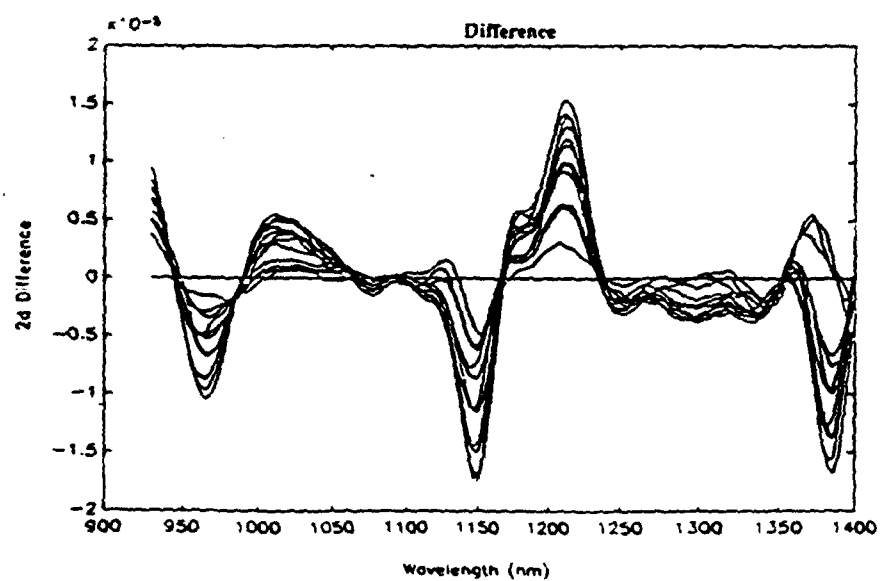
Figure 11a

Figure 11b
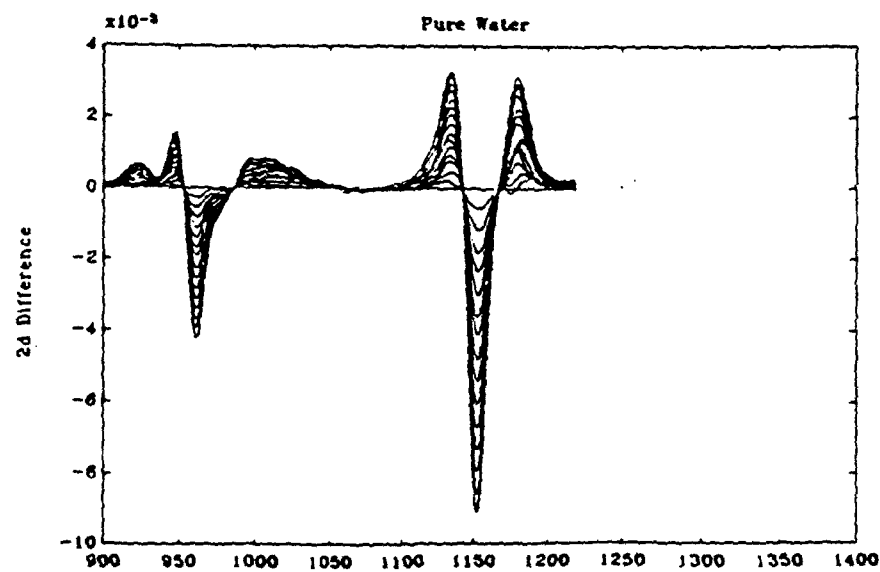
Figure 11c

Skin Temperature

Figure 12

□ Calibration   + Prediction   Measured

Ischemia

2d Reflectance

Wavelength (nm)
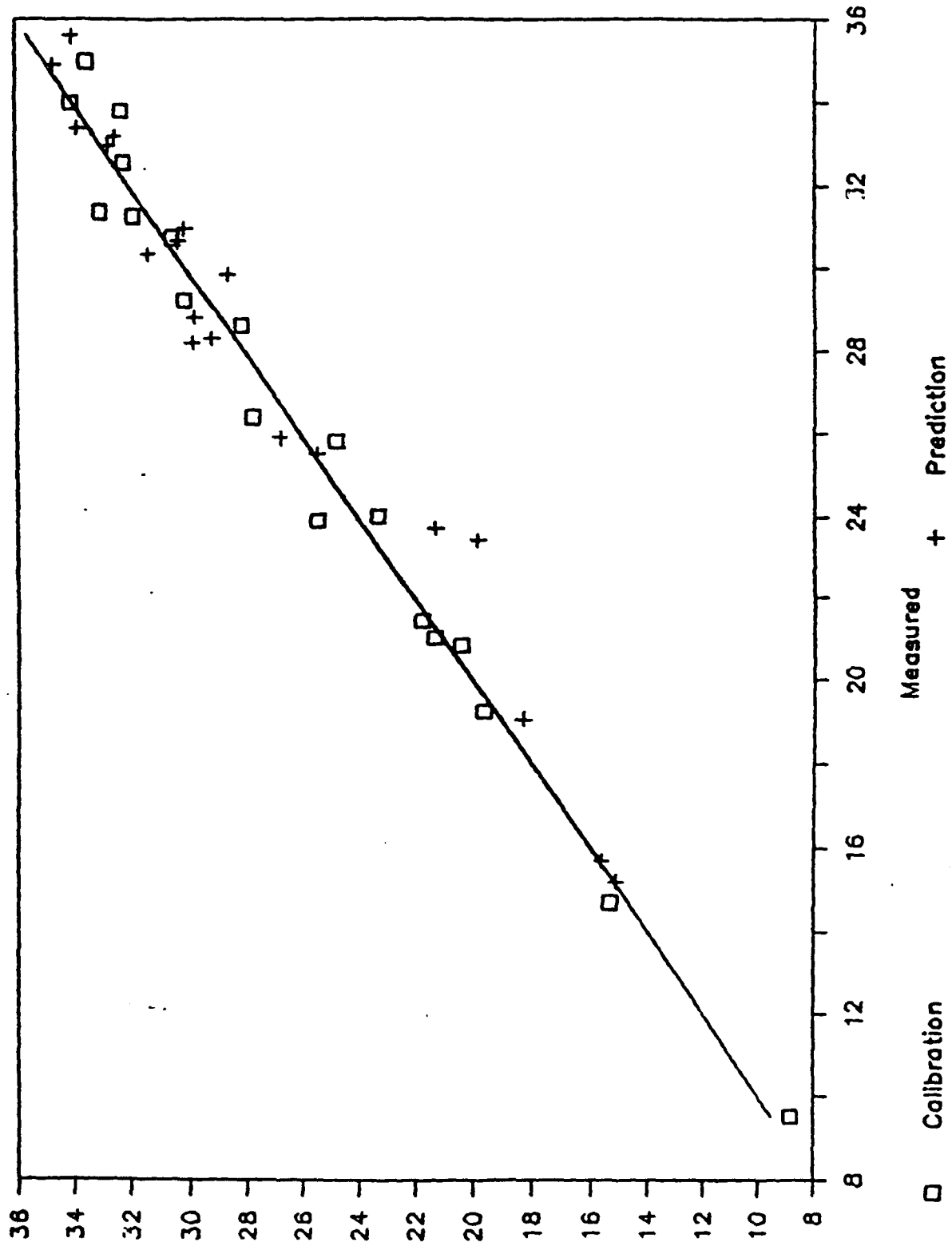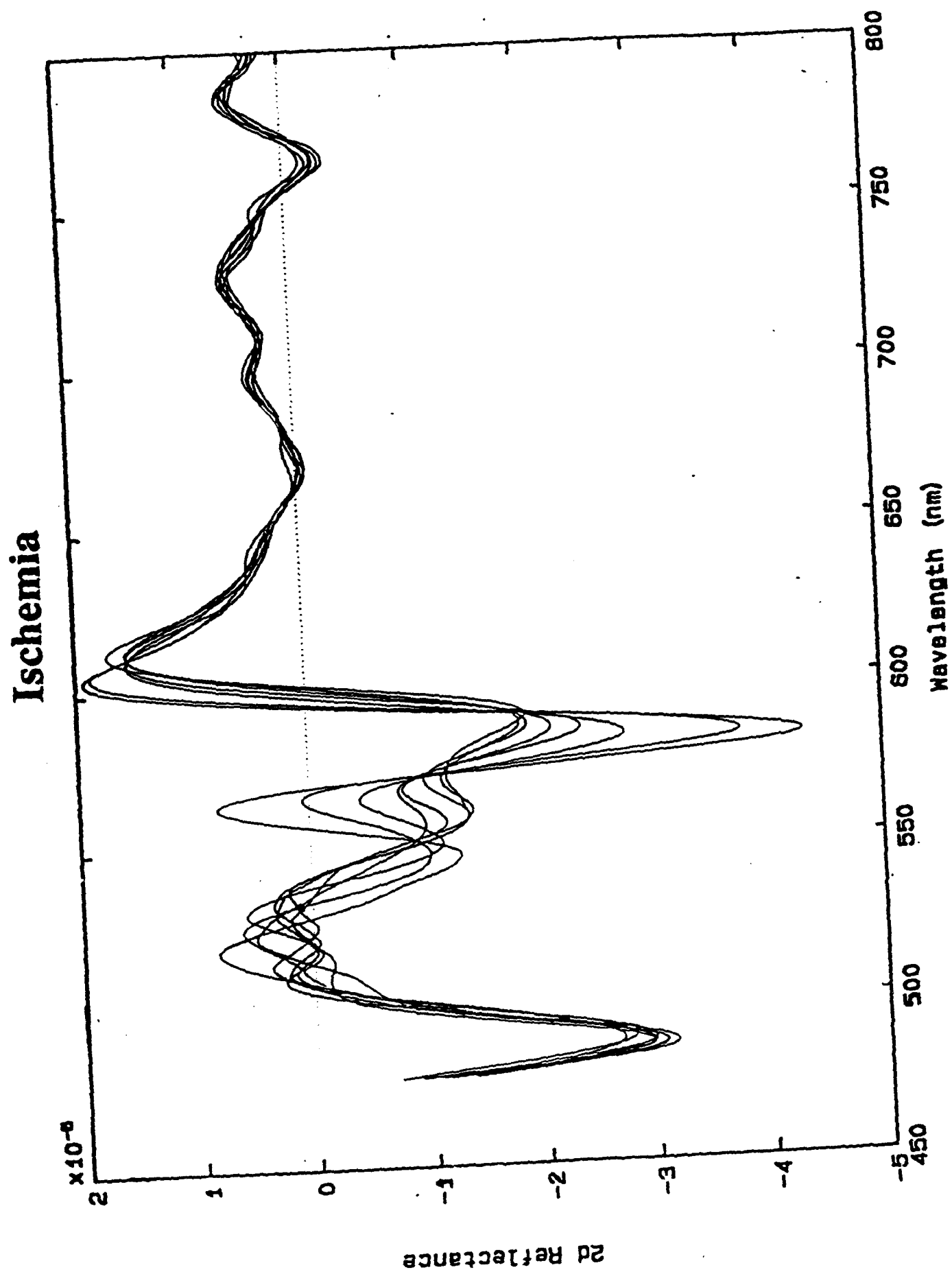
Figure 13

PCA of Ischemia
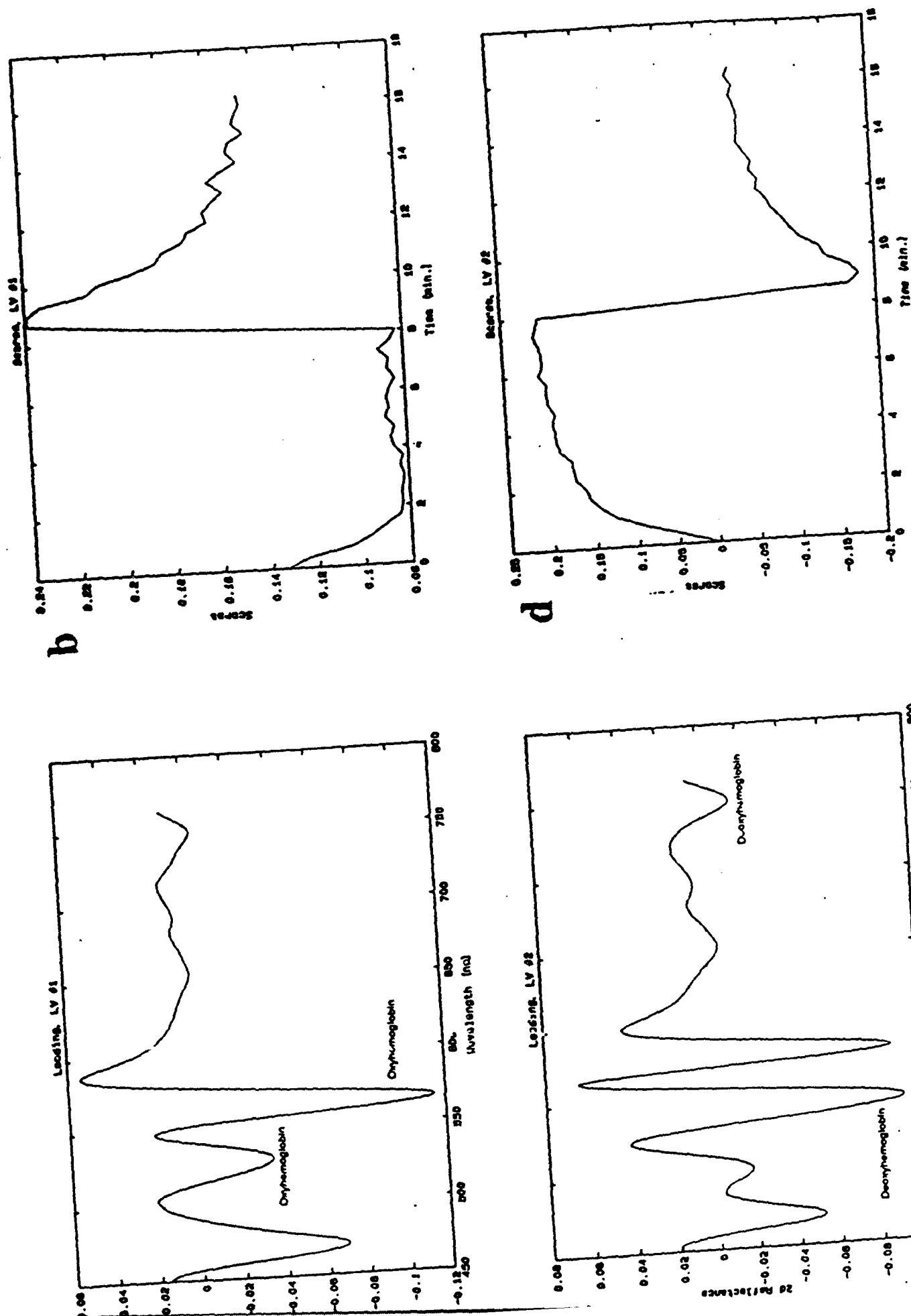
Figure 14
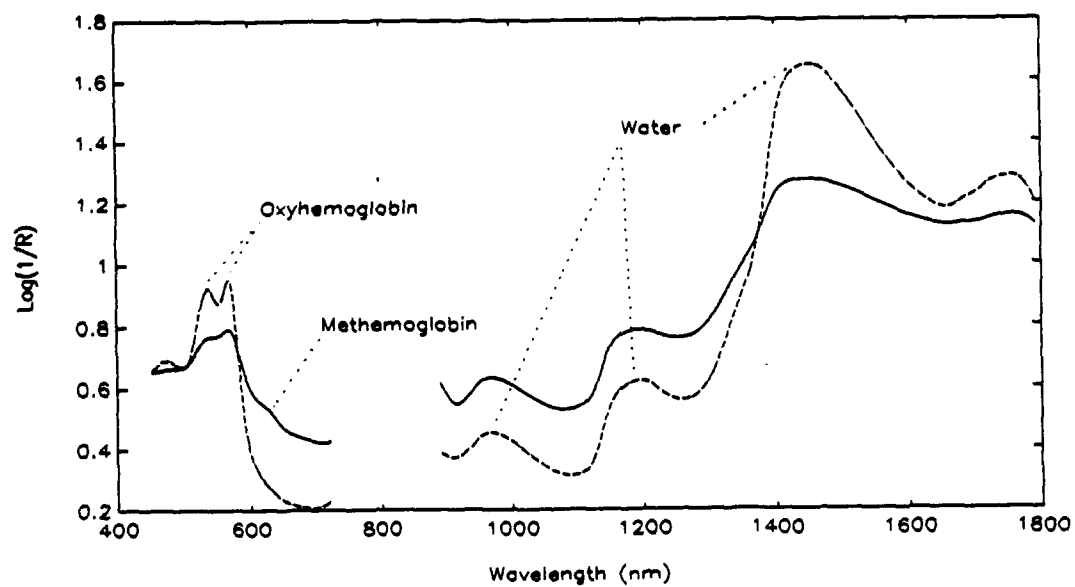
Figure 15. Typical spectra of burn wounds. (--) shallow and (—) deep injuries.
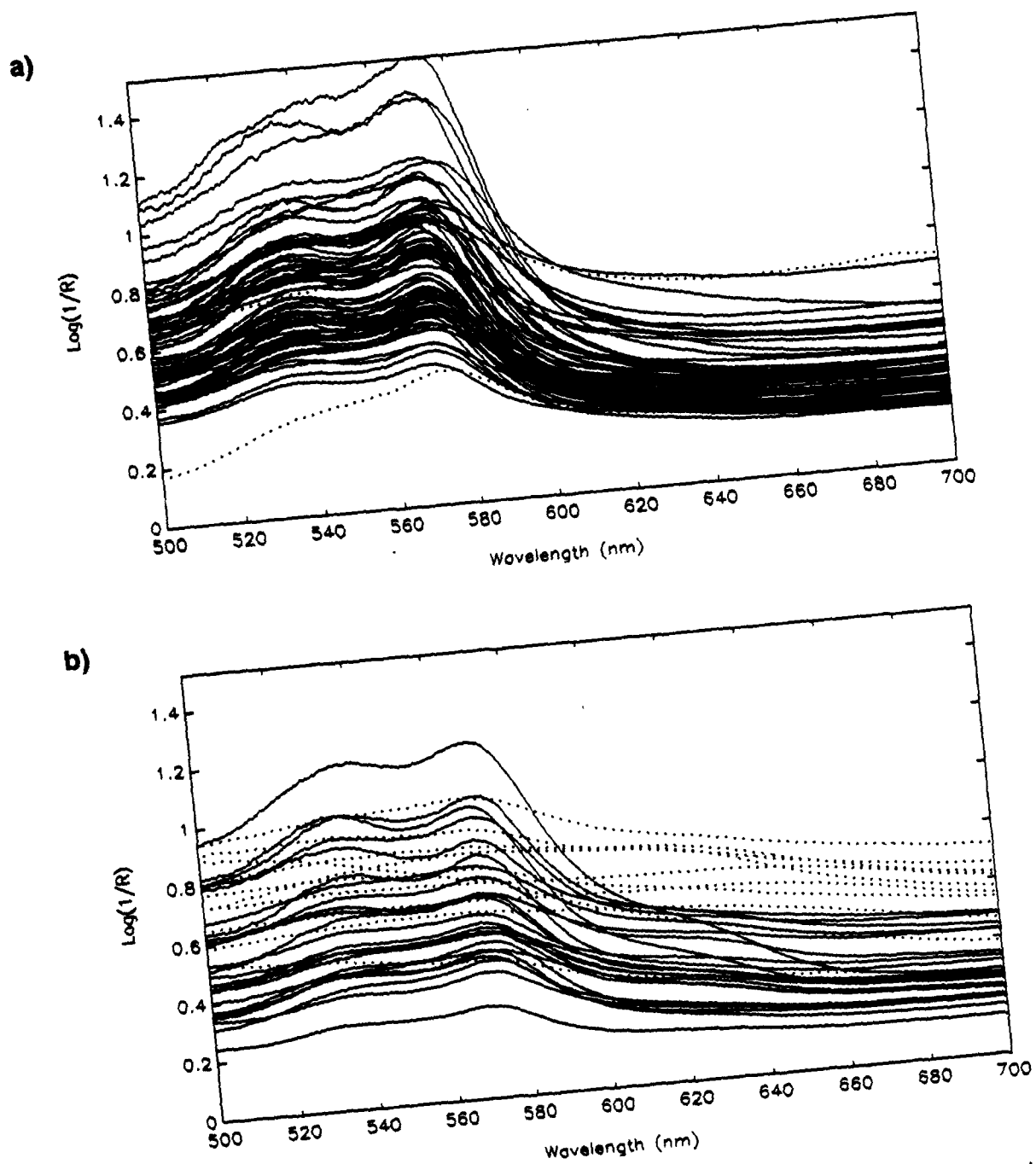
Figure 16. Aggregate spectra of burn wounds. a) shallow and b) deep injuries.
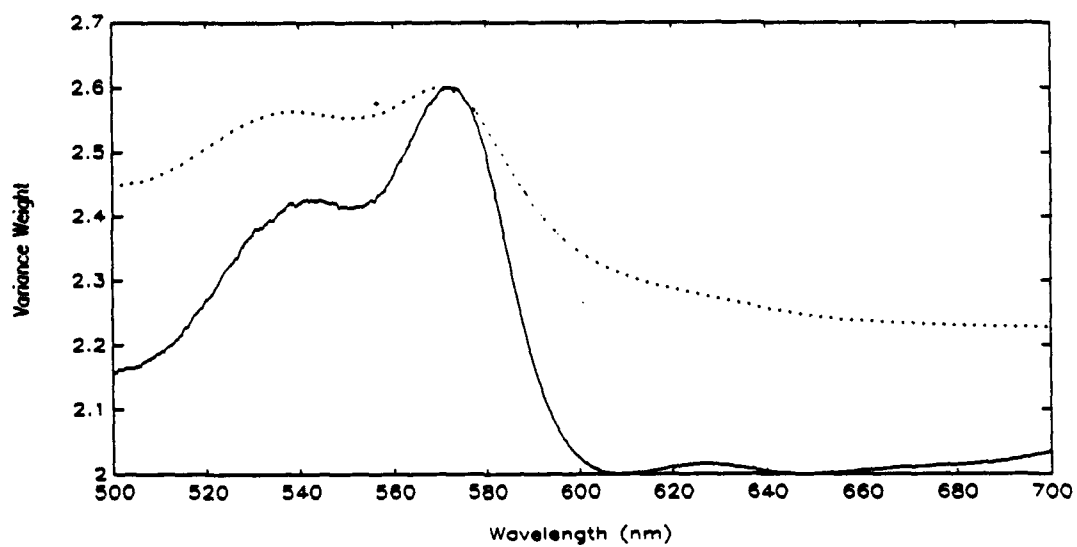
Figure 17. Variance weigths of raw spectra. (—) variance weights (· ·) mean spectrum.

a)

b)
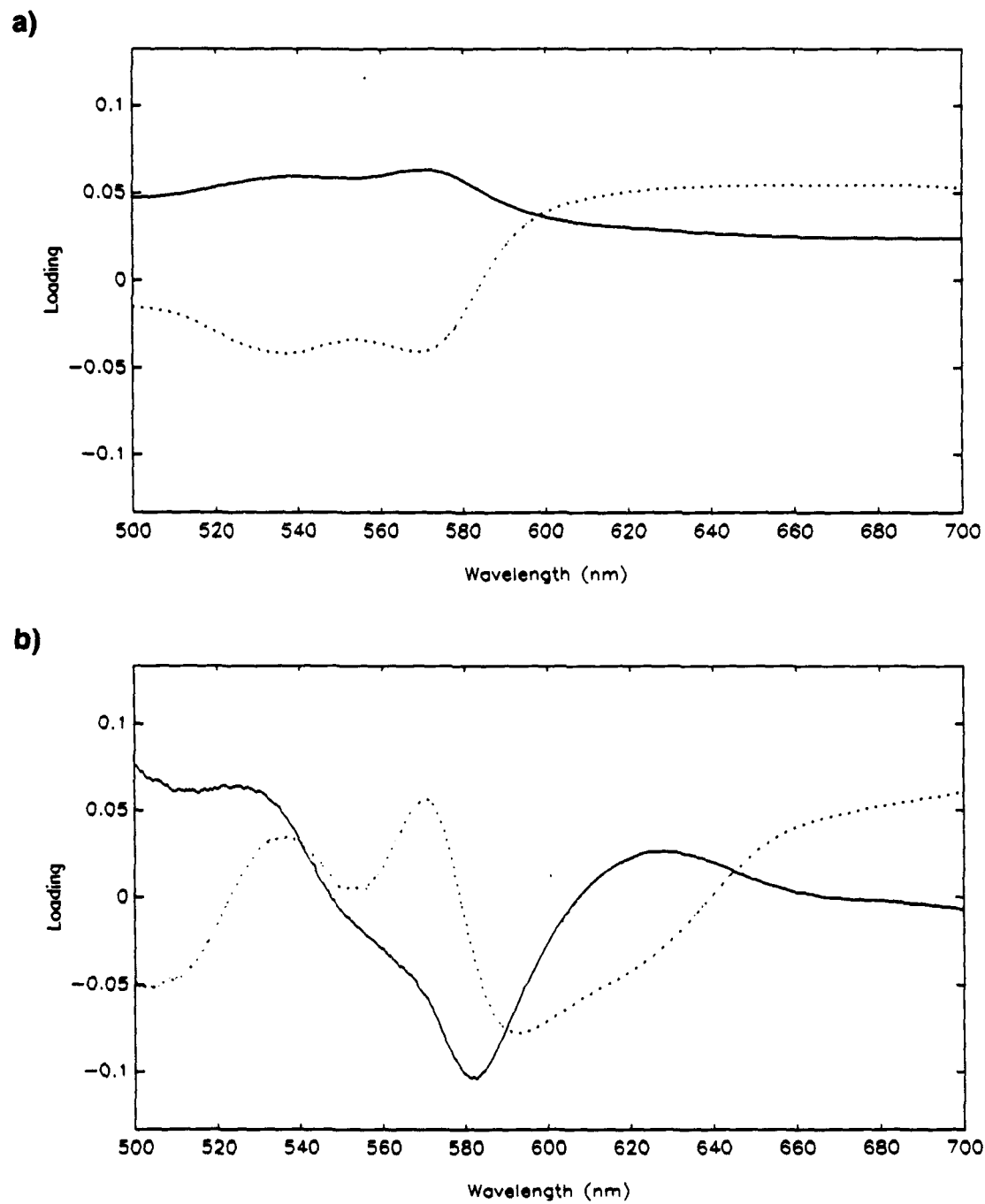
Figure 18. Loadings from principal component analysis of raw spectra. Eigenvectors c) 1 and 2, d) 3 and 4. Eigenvectors (-) 1 and 3 (...) 2 and 4.

c)

d)
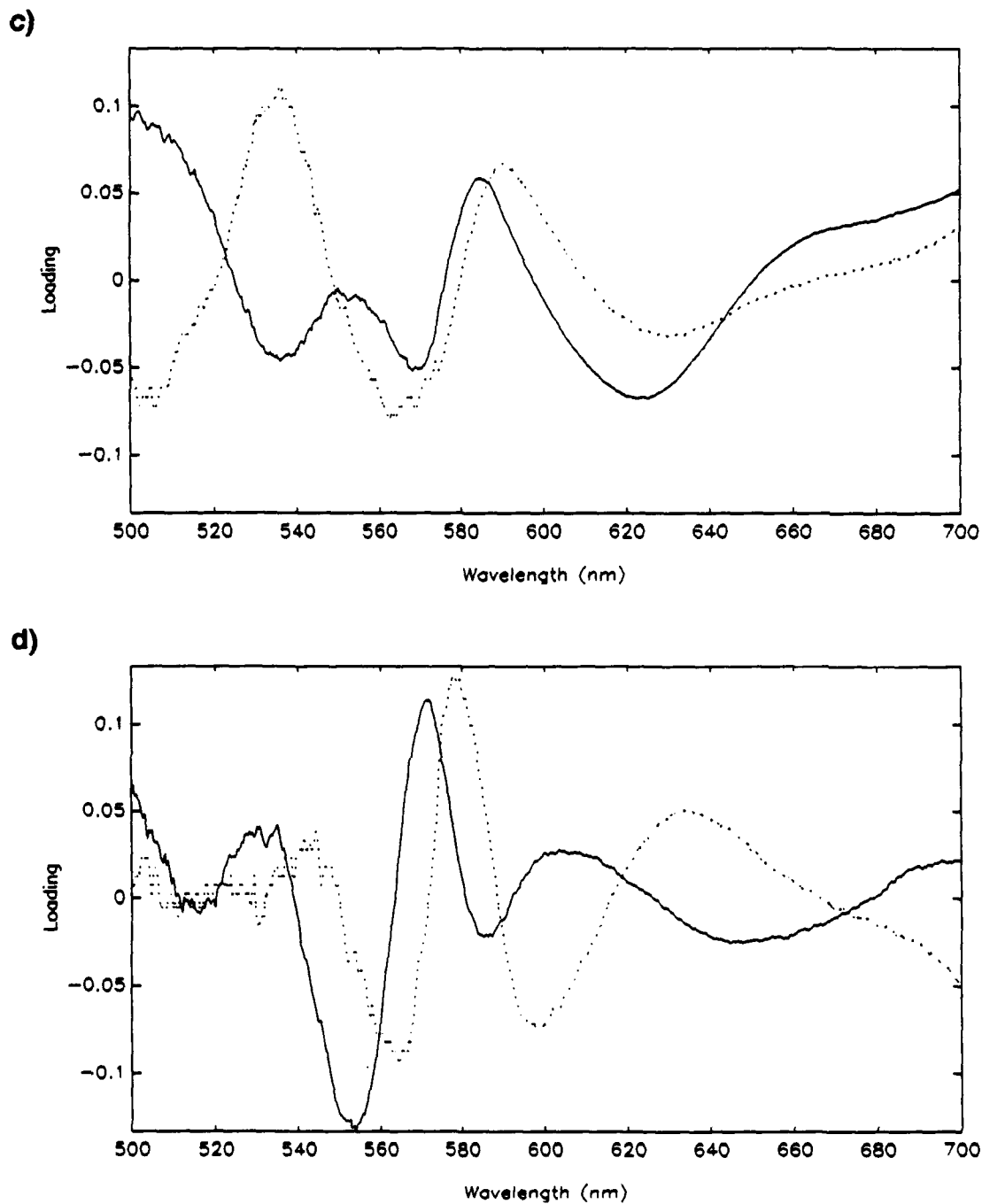
Figure 18. Loadings from principal component analysis of raw spectra. Eigenvectors a) 5 and 6, b) 7 and 8. Eigenvectors (-) 5 and 7 (...) 6 and 8.
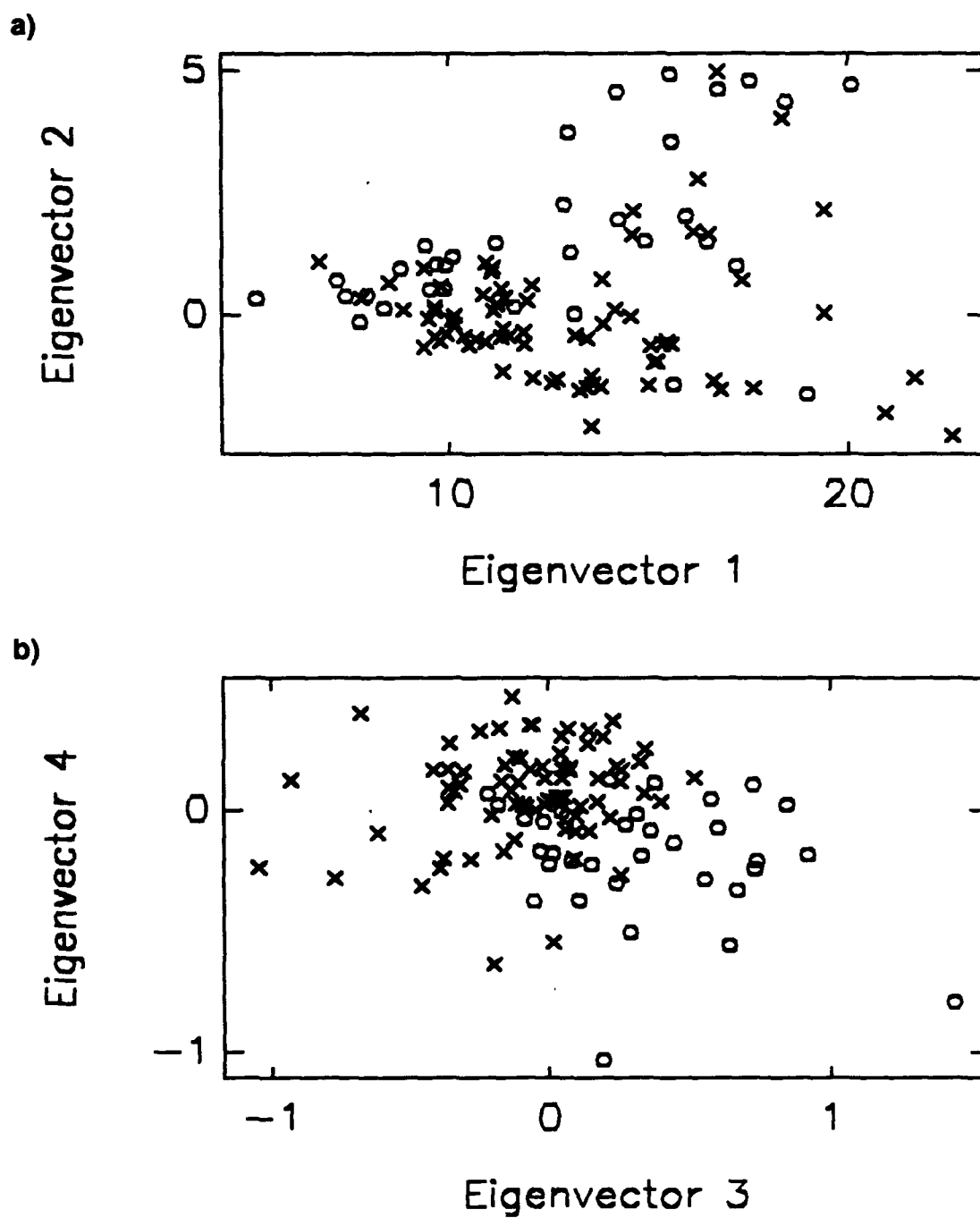
Figure 19. Scores from principal component analysis of raw spectra. (x) shallow and (o) deep injuries.

c)

d)
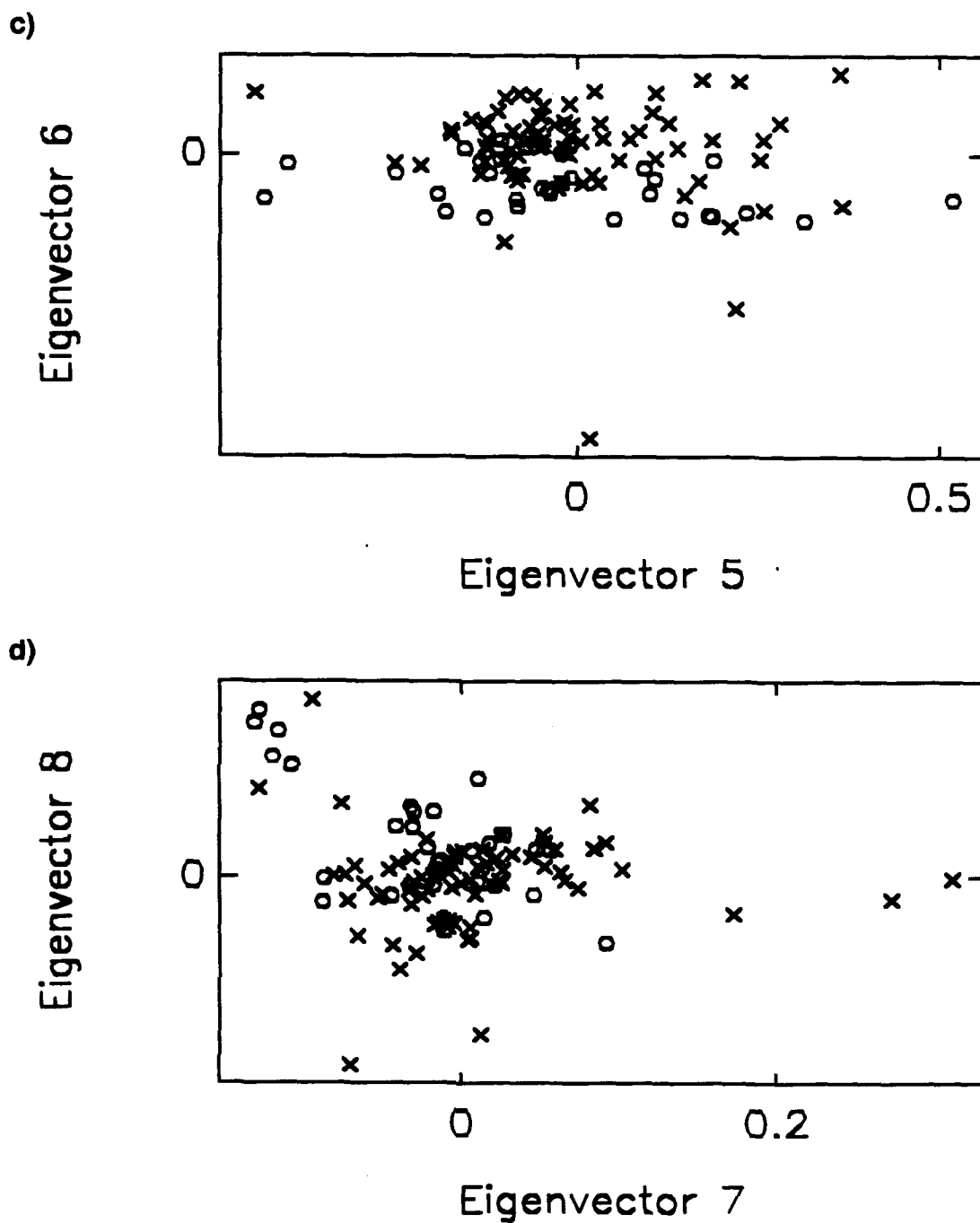
Figure 19. Scores from principal component analysis of raw spectra. (x) shallow and (o) deep injuries.
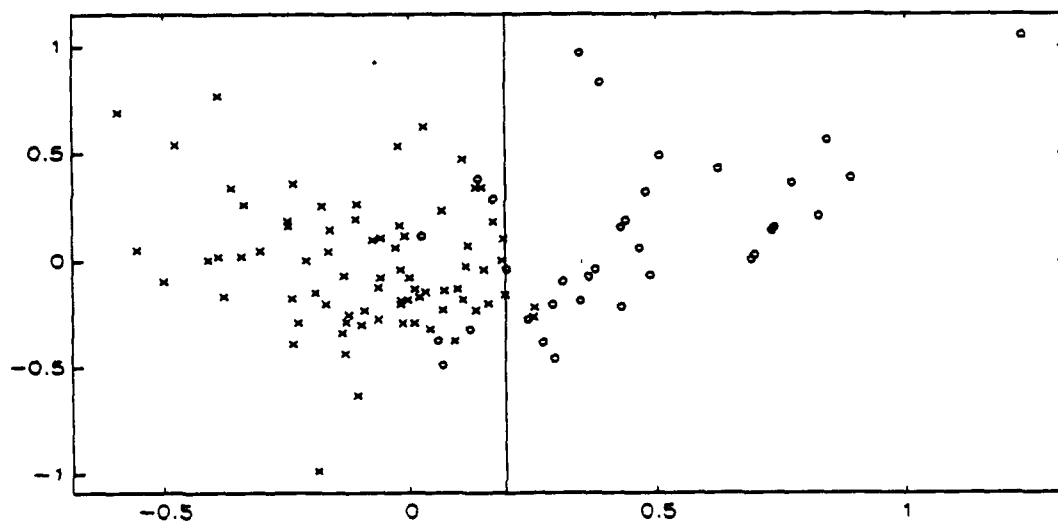
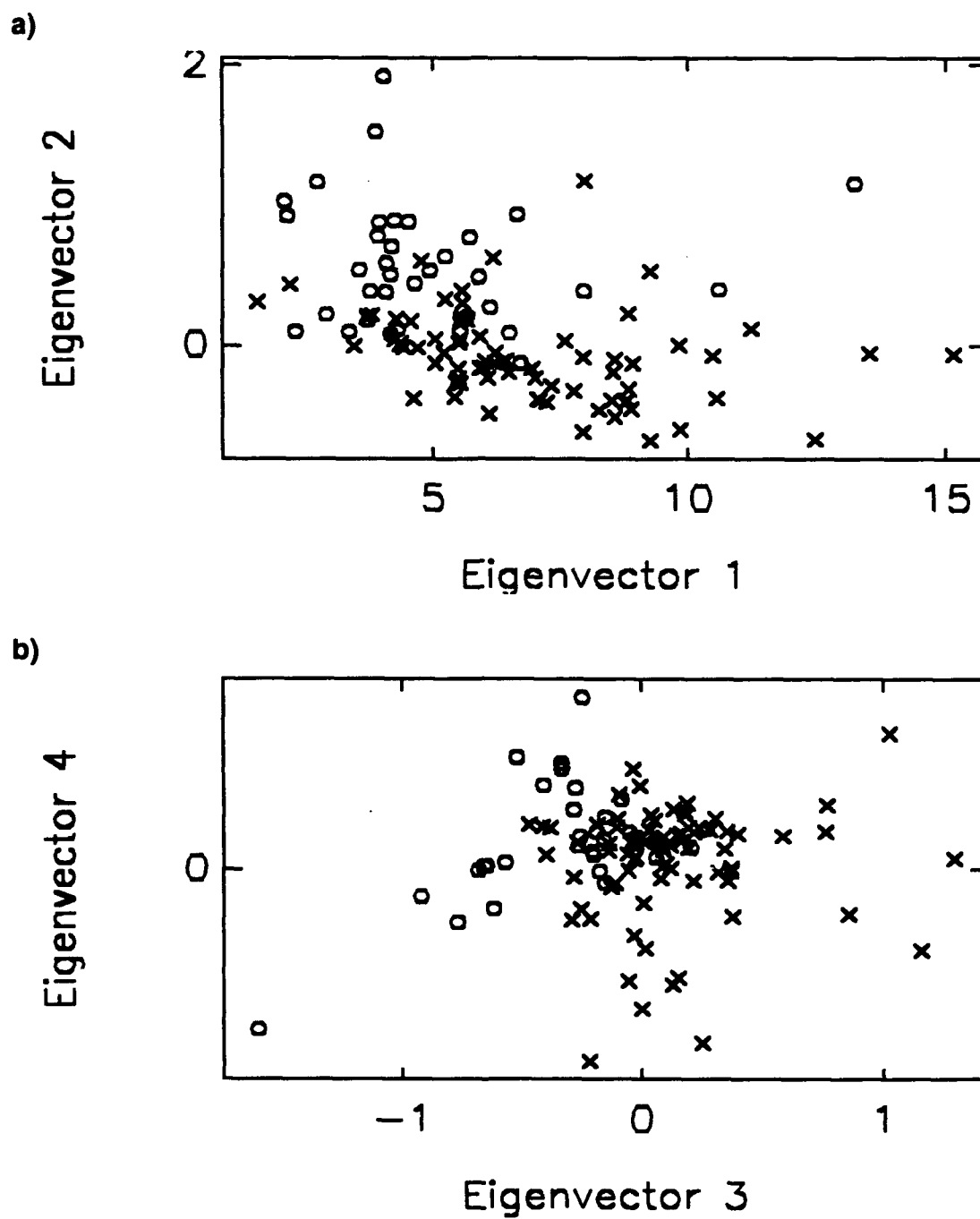**Figure 20.** Rotated PCA scores from raw spectra. (x) shallow and (o) deep injuries.
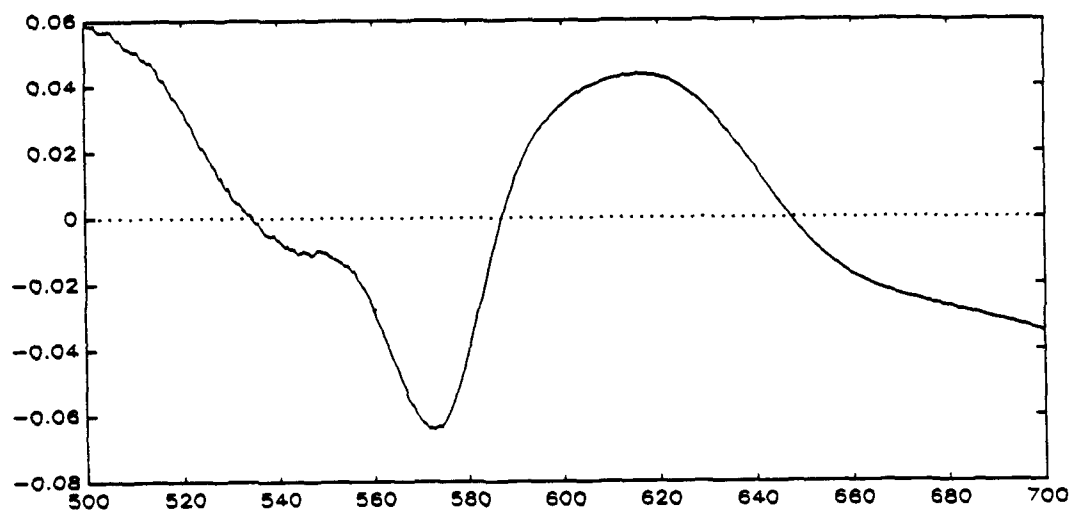
Figure 21. First rotated PCA loading from raw spectra.
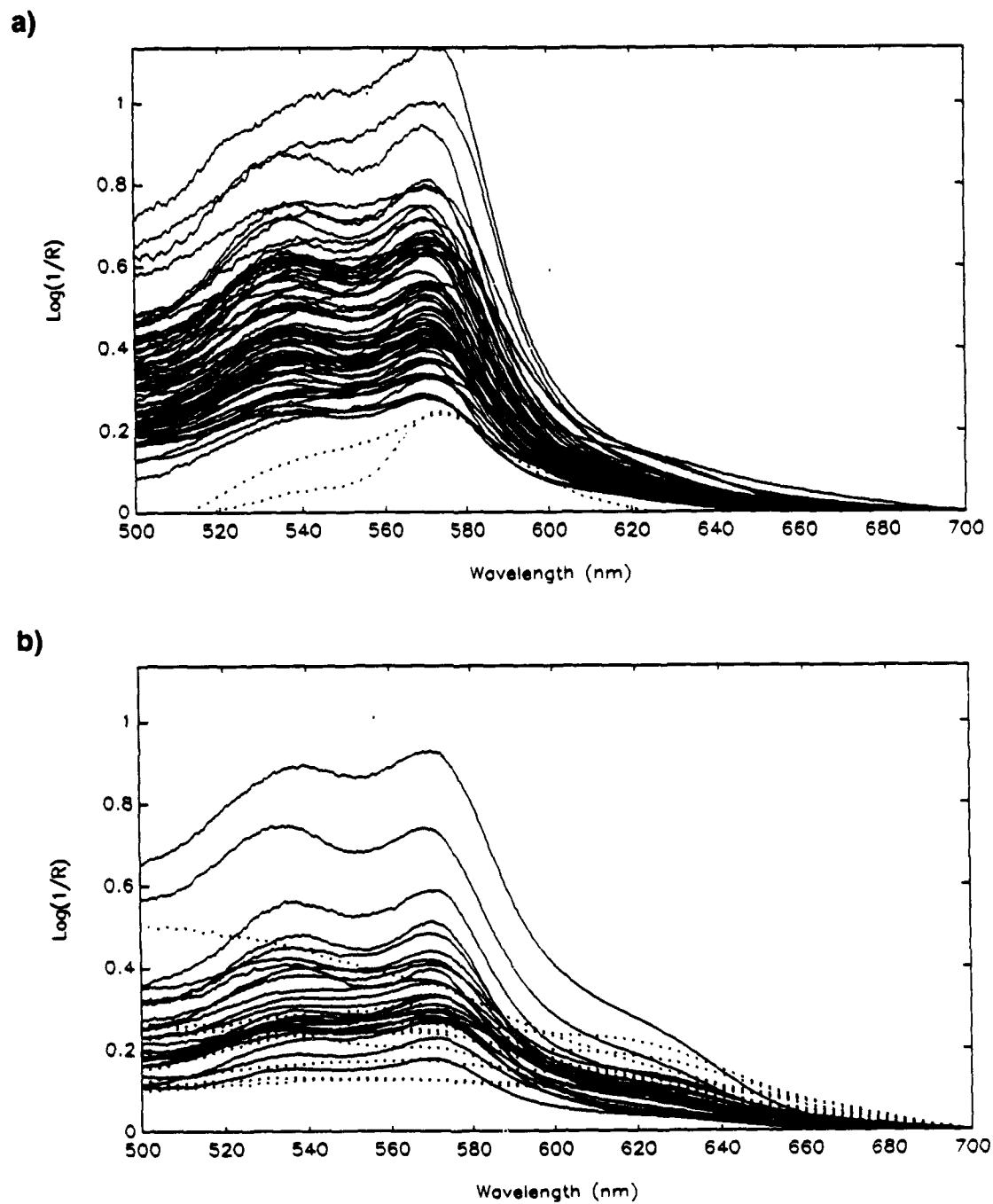
Figure 22. Baseline-subtracted spectra. a) shallow and b) deep injuries.
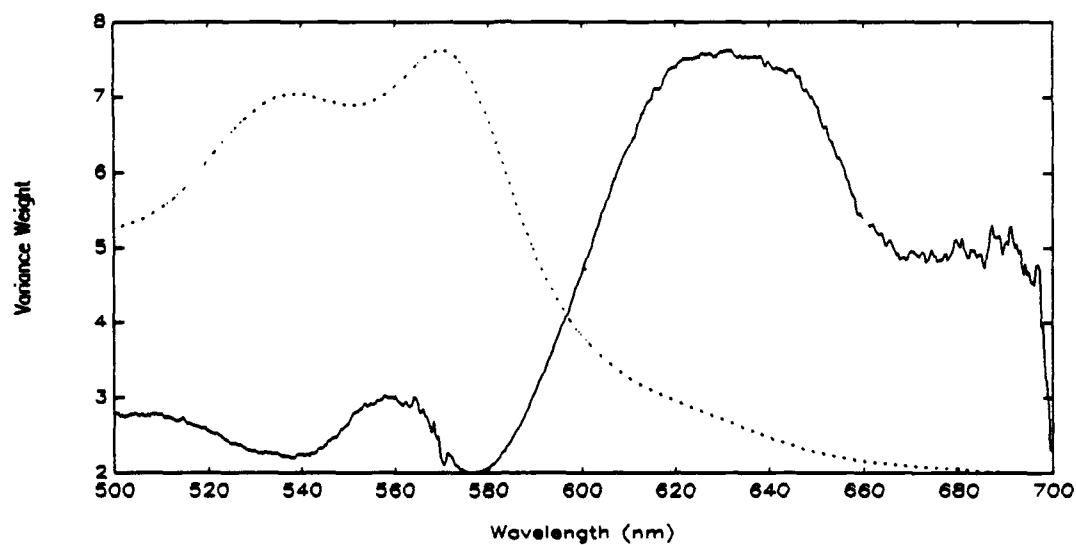
a)

b)
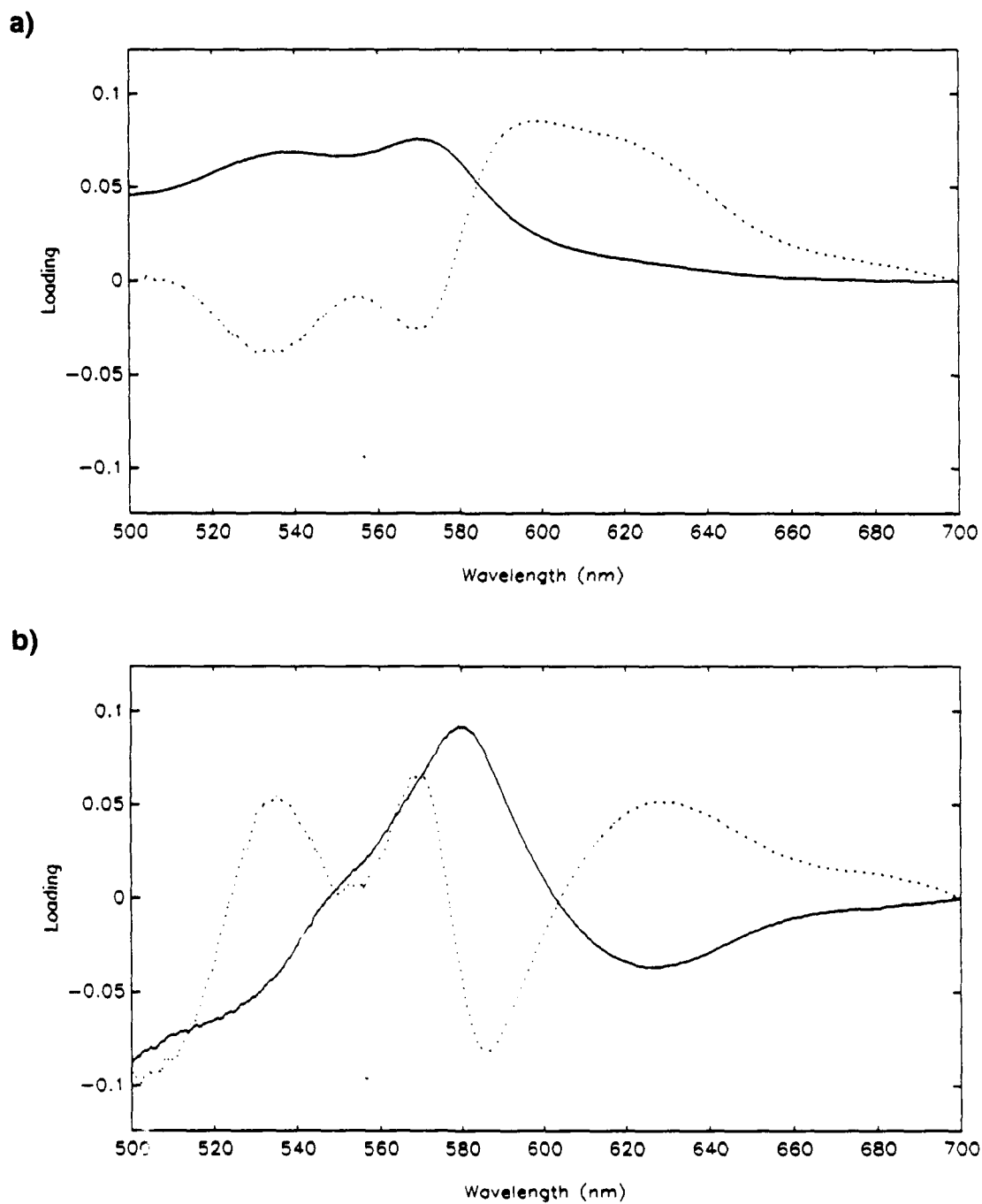
Figure 23. Loadings from principal component analysis of baseline-subtracted spectra. Eigenvectors a) 1 and 2, b) 3 and 4. Eigenvectors (-) 1 and 3 and (...) 2 and 4.
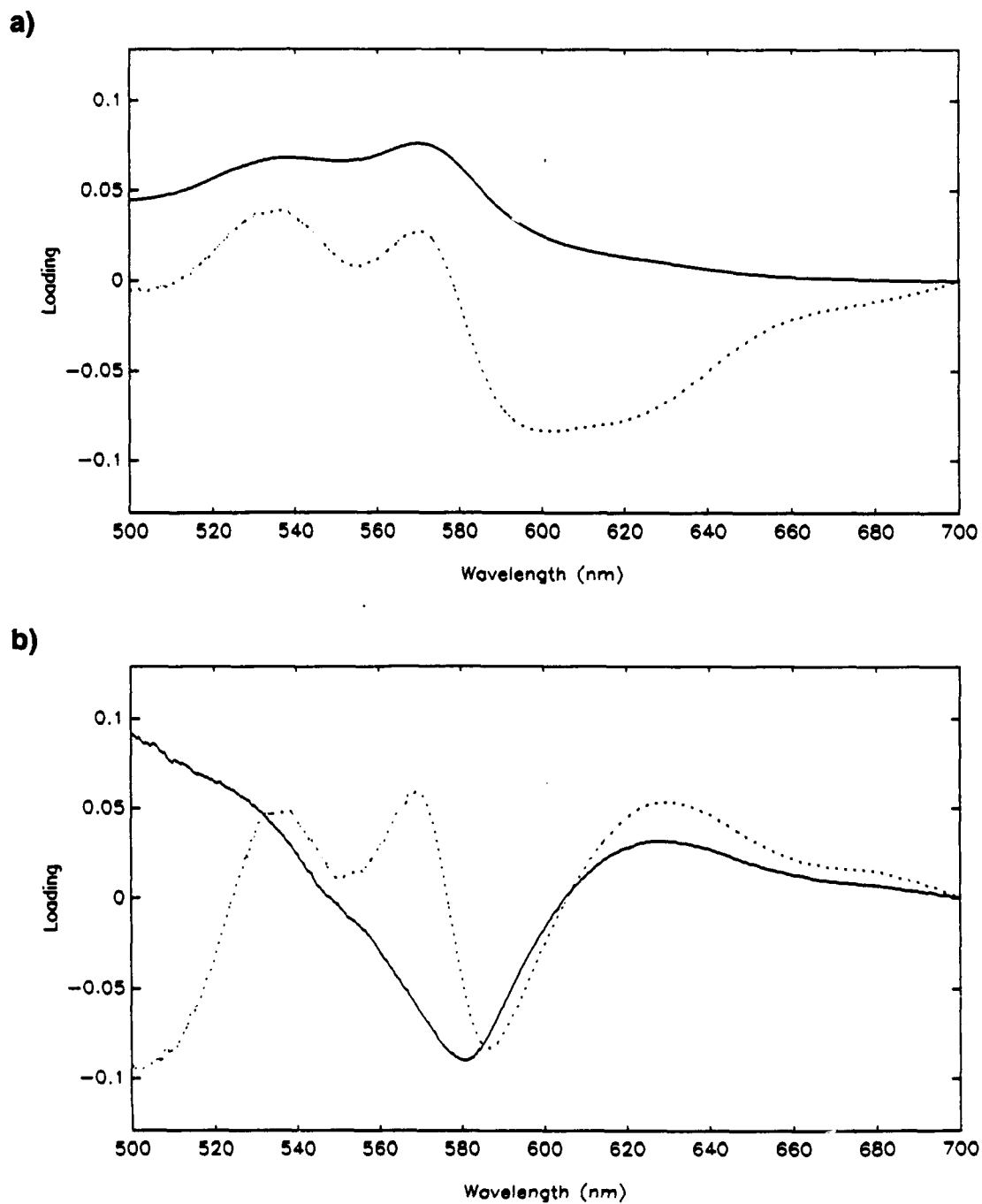
a)

b)

Figure 24. Scores from principal component analysis of baseline-subtracted spectra. (x) shallow and (o) deep injuries.
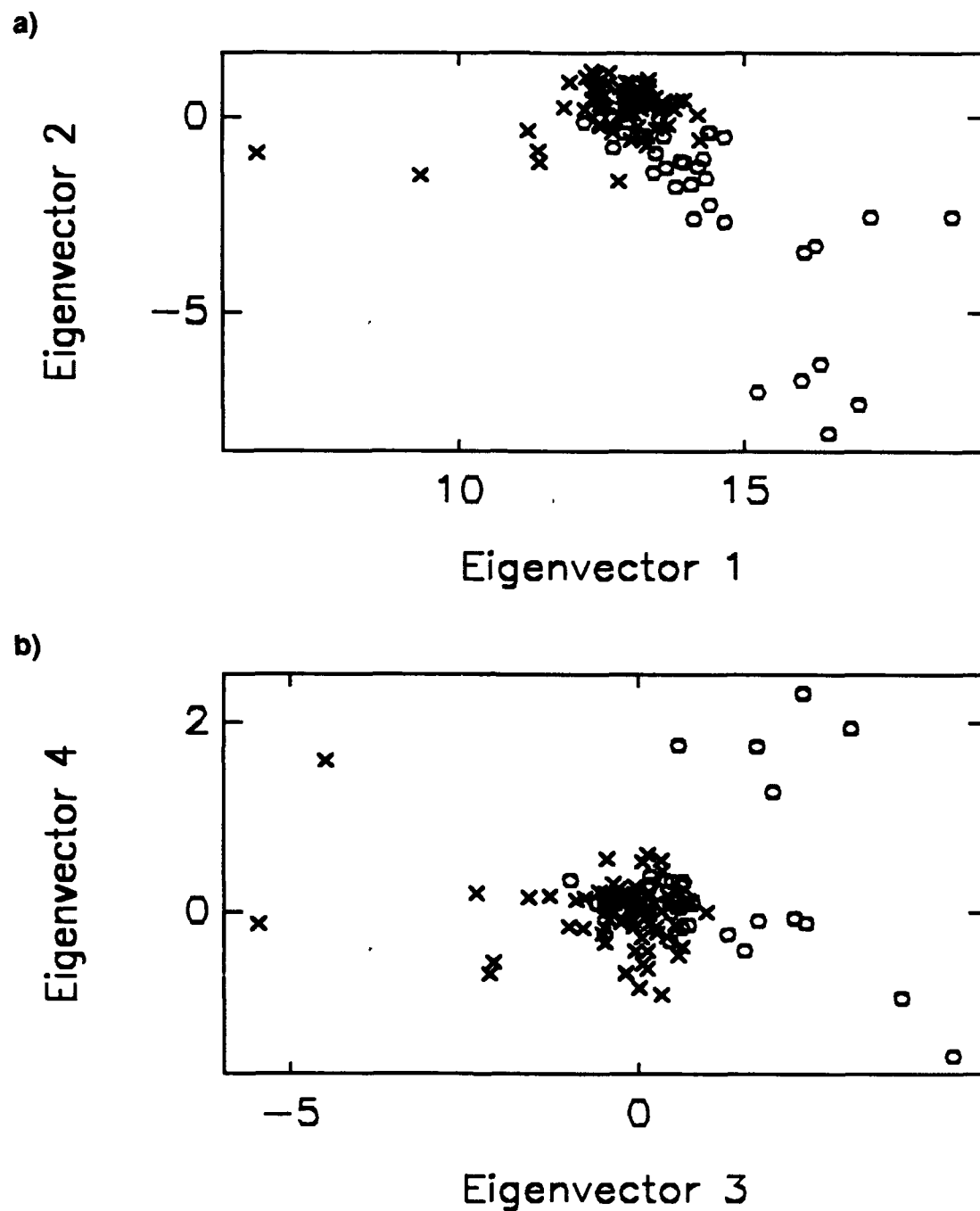
a)

b)
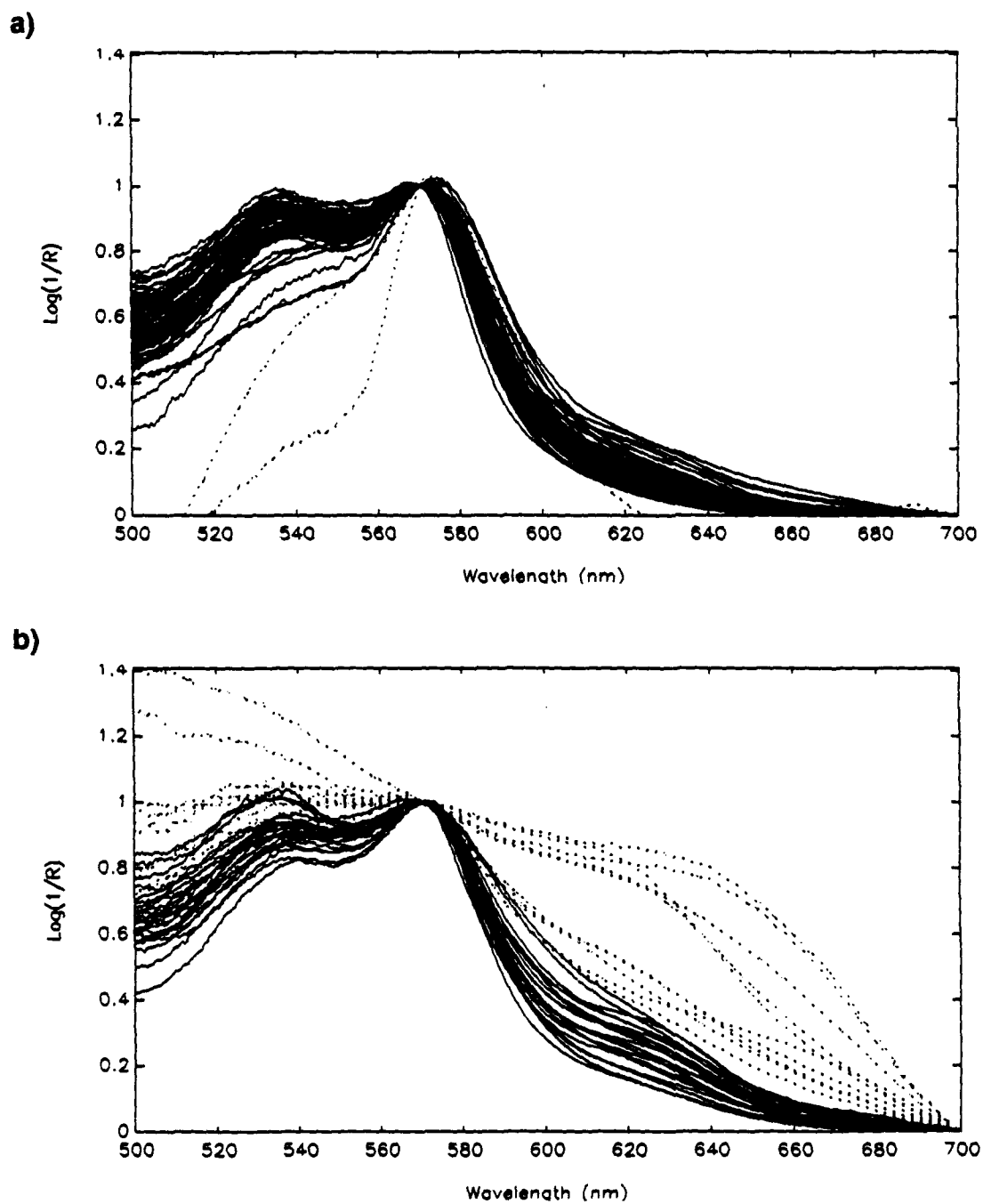
Figure 25. Normalized spectra of burn wounds. a) shallow and b) deep injuries.

Figure 26. Variance weigths of single-wavelength normalized spectra. (—) variance weights (· ·) mean spectrum.

a)

b)

Figure 27. Loadings from principal component analysis of normalized spectra. Eigenvectors a) 1 and 2, b) 3 and 4. Eigenvectors (-) 1 and 3, (...) 2 and 4.

a)

b)

Figure 28. Scores from principal component analysis of normalized spectra. (x) shallow and (o) deep injuries.
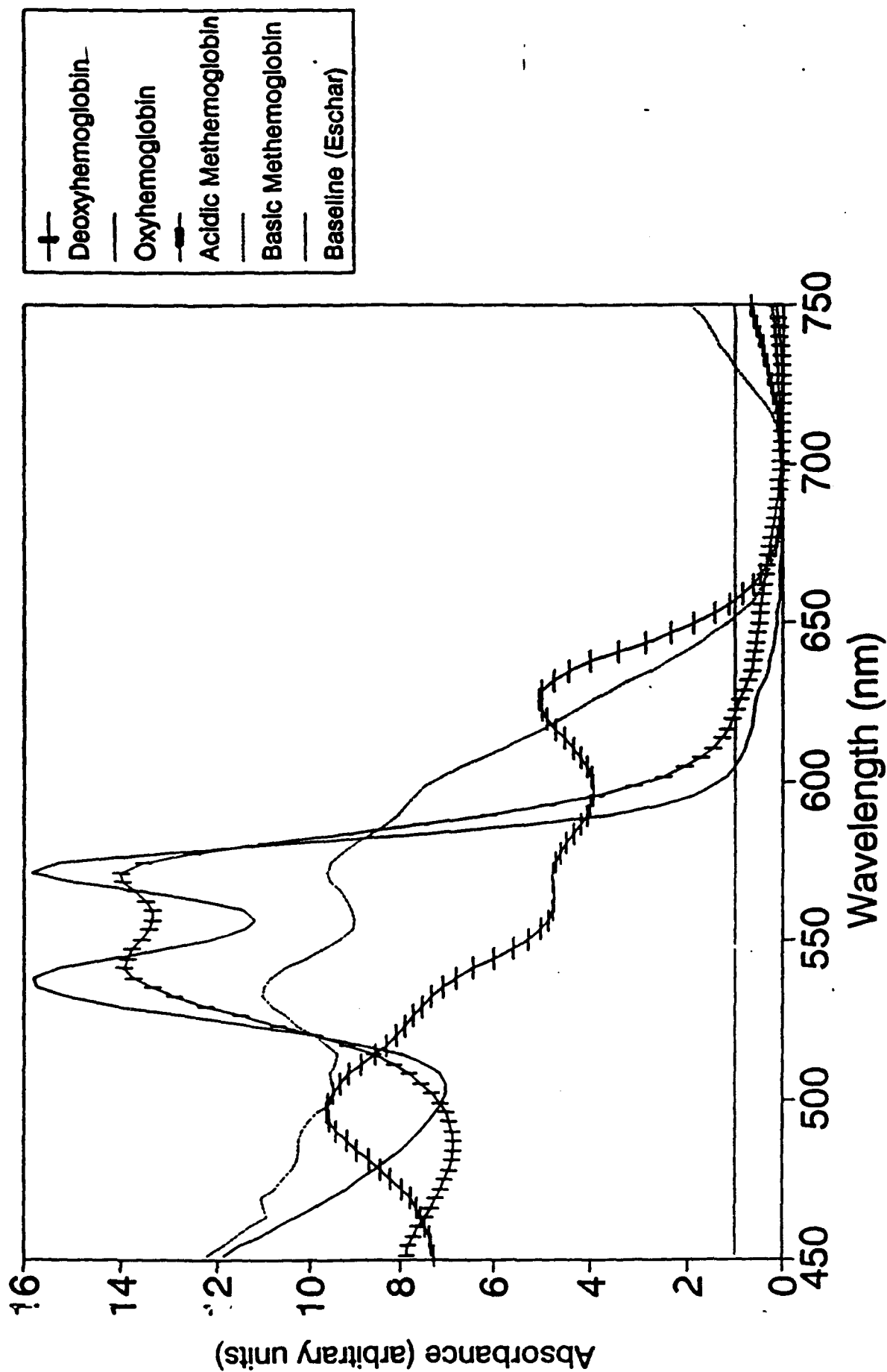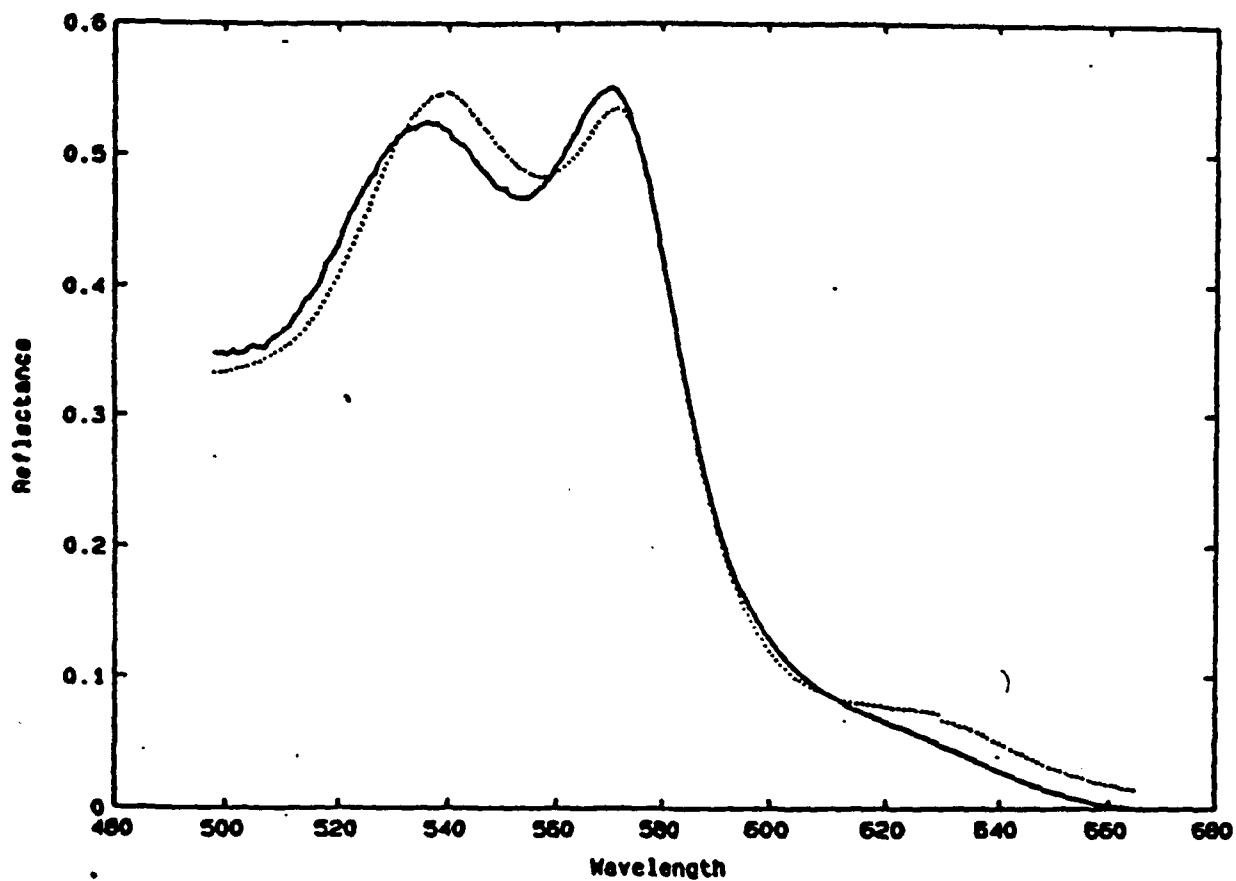
Hemoglobin Spectra Model, basis spectra

Legend:
- ┼ Deoxyhemoglobin
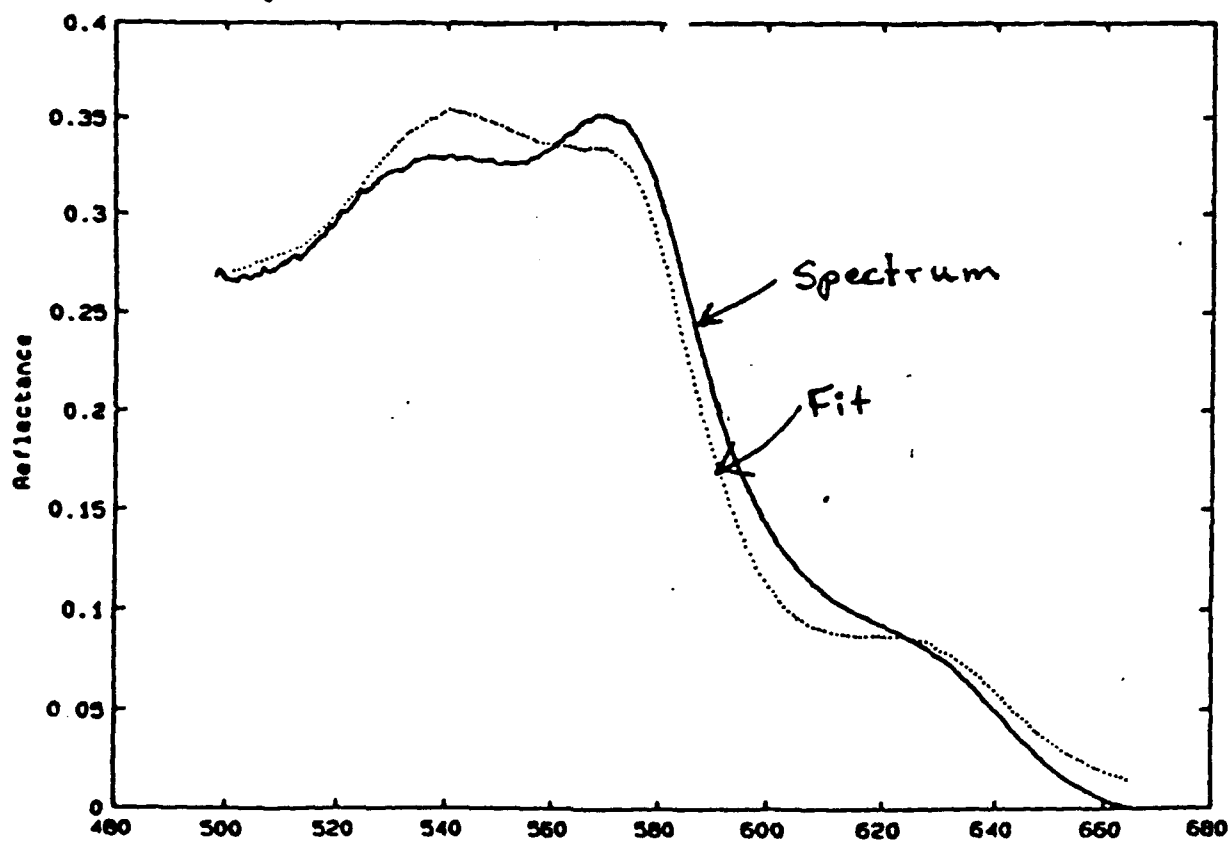- Oxyhemoglobin
- ▬ Acidic Methemoglobin
- Basic Methemoglobin
- Baseline (Eschar)

X-axis: Wavelength (nm)
Y-axis: Absorbance (arbitrary units)

Figure 29

86

Shallow

Deep

Figure 30

Hemoglobin Basis Set

baseline

acid methemoglobin

base methemoglobin

oxyhemoglobin

deoxyhemoglobin

Wavelength (nm)

Specular Reflectance Basis Set

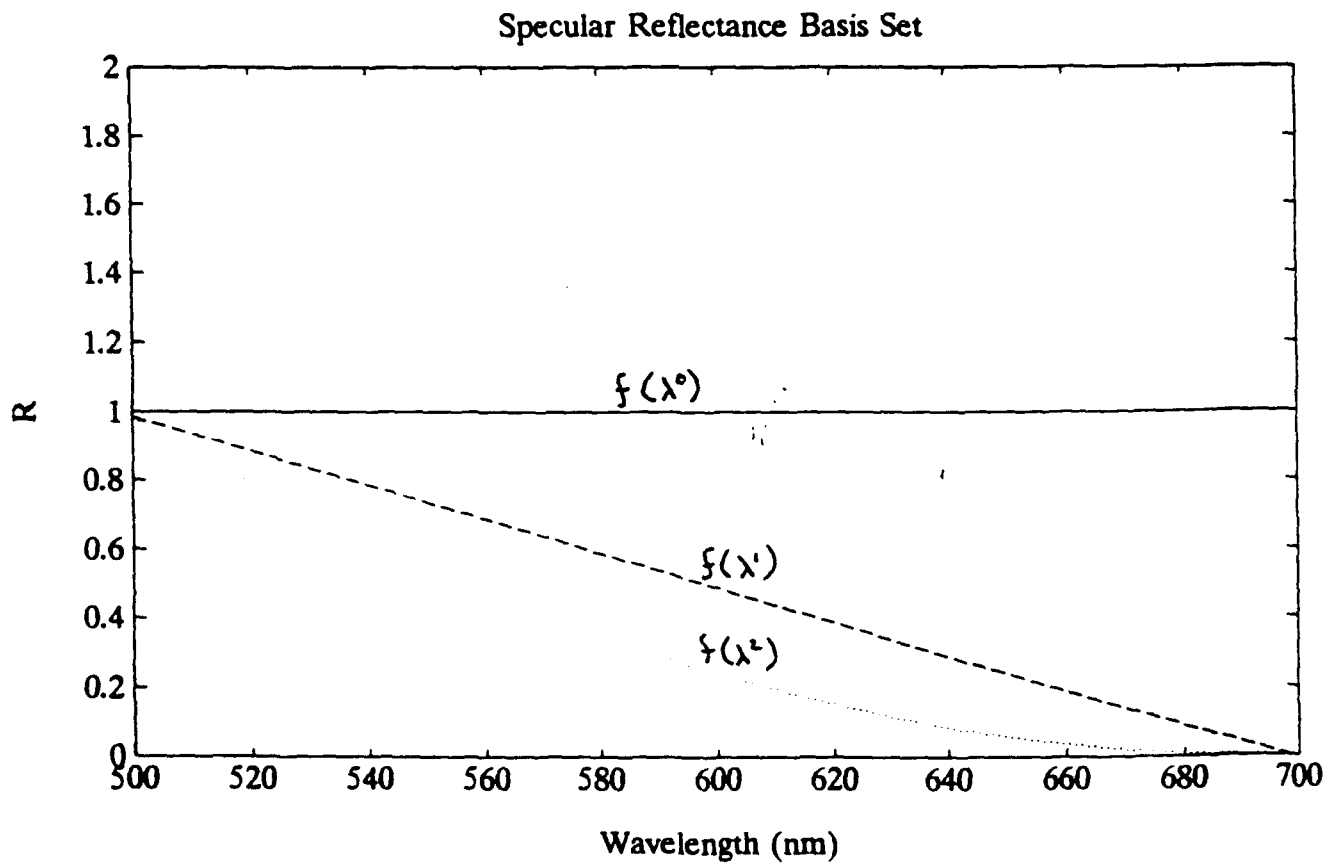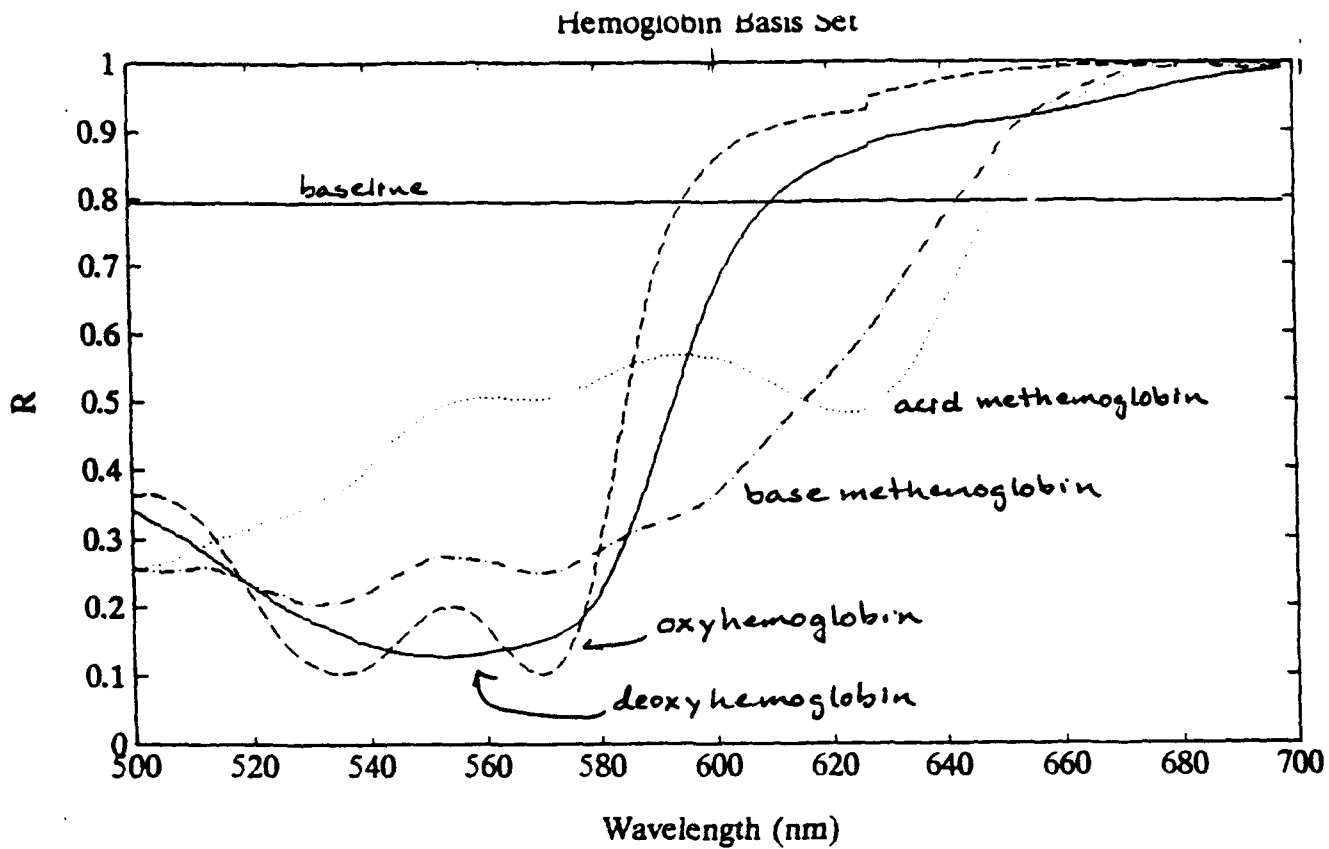$f(\lambda^0)$
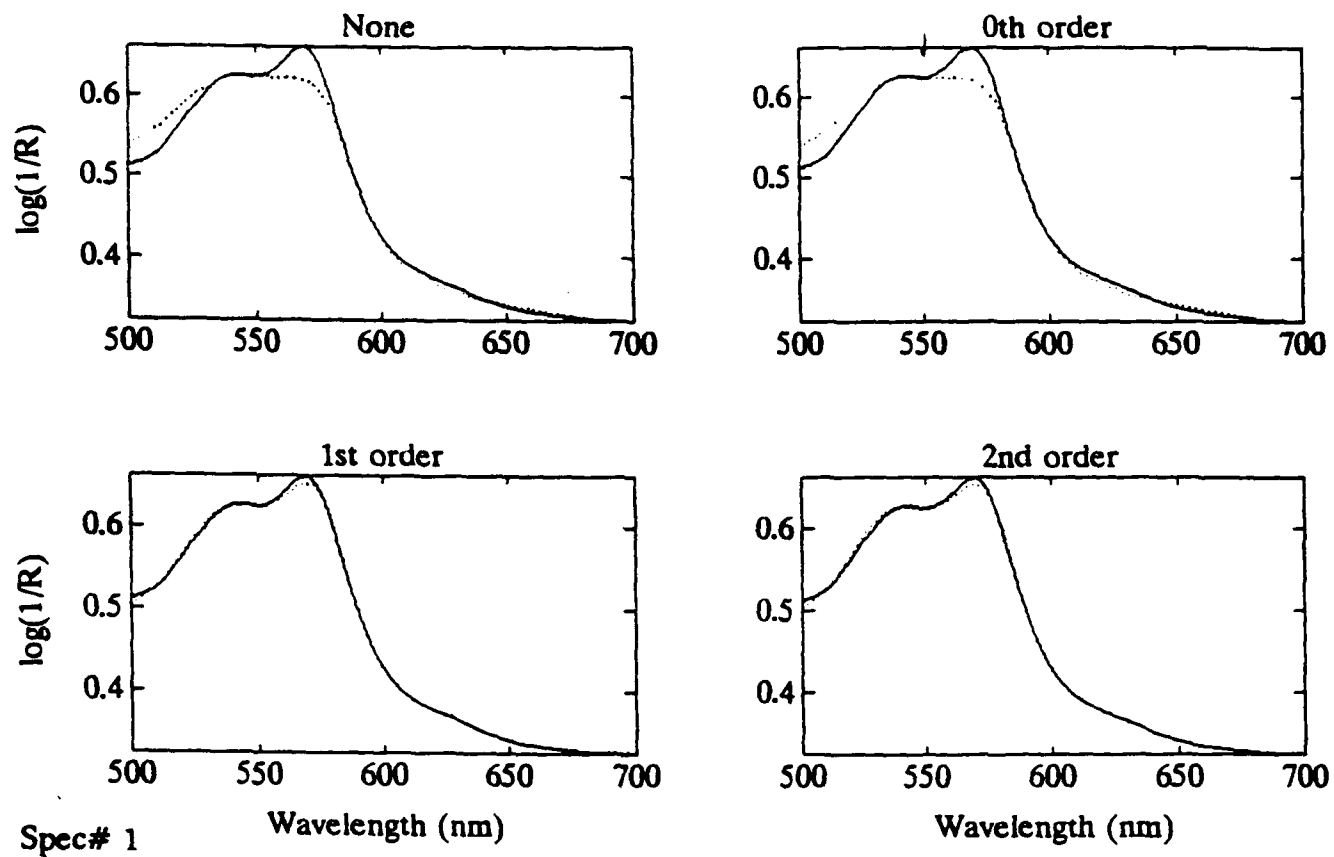
$f(\lambda^1)$

$f(\lambda^2)$

Wavelength (nm)

Figure 31

Figure 32   (—) burn spectrum, (···) reconstructed spectrum

None

0th order

1st order

2nd order

Spec# 39
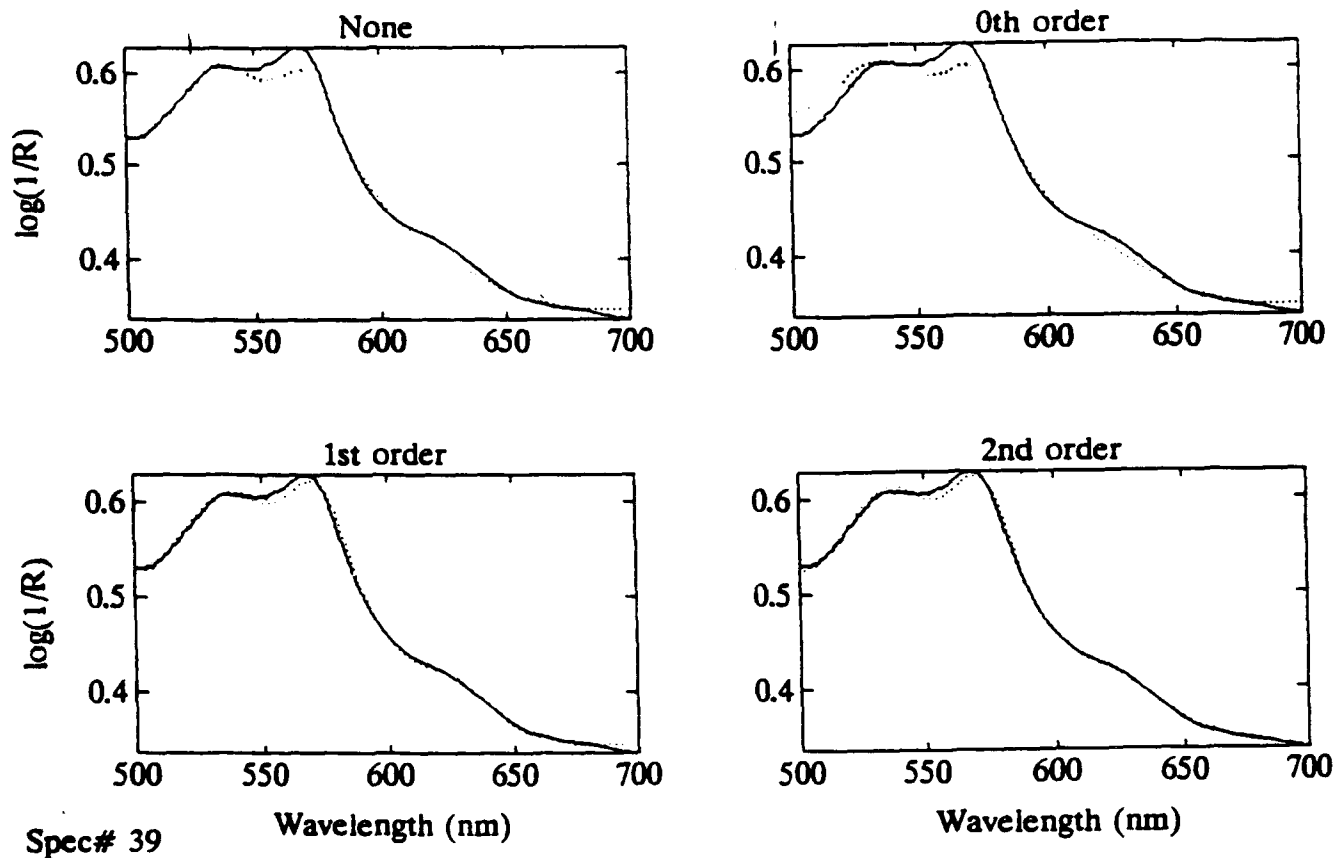
Figure 33 (—) spectrum of deep burn, (...) reconstructed spectrum
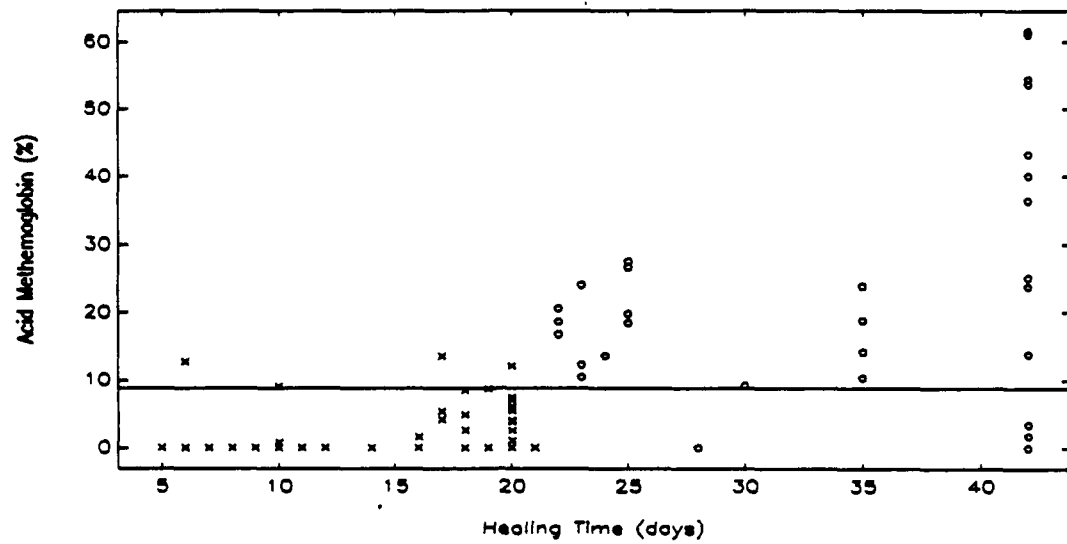
Figure 34. Relative acid methemoglobin concentration. (x) shallow and (o) deep injuries.

A
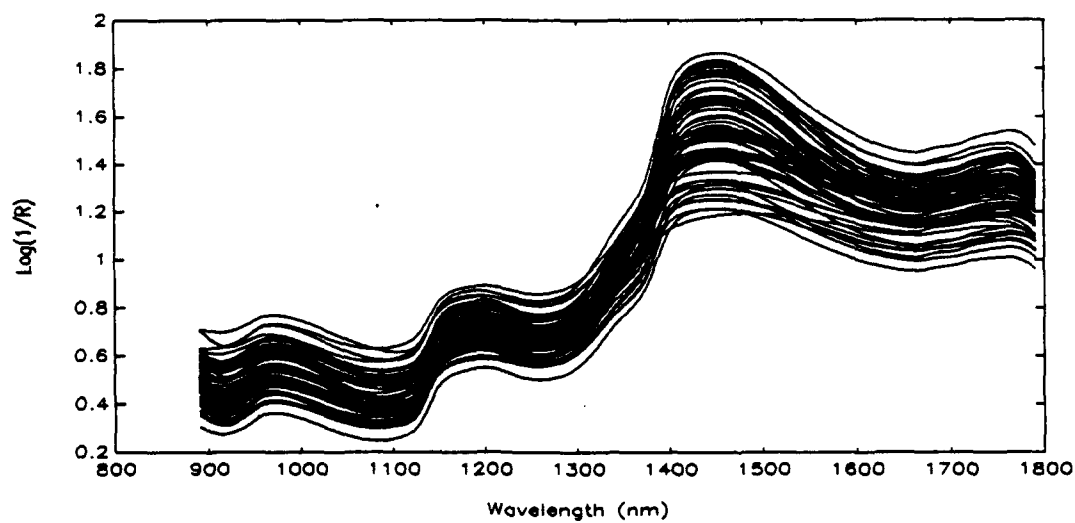
B
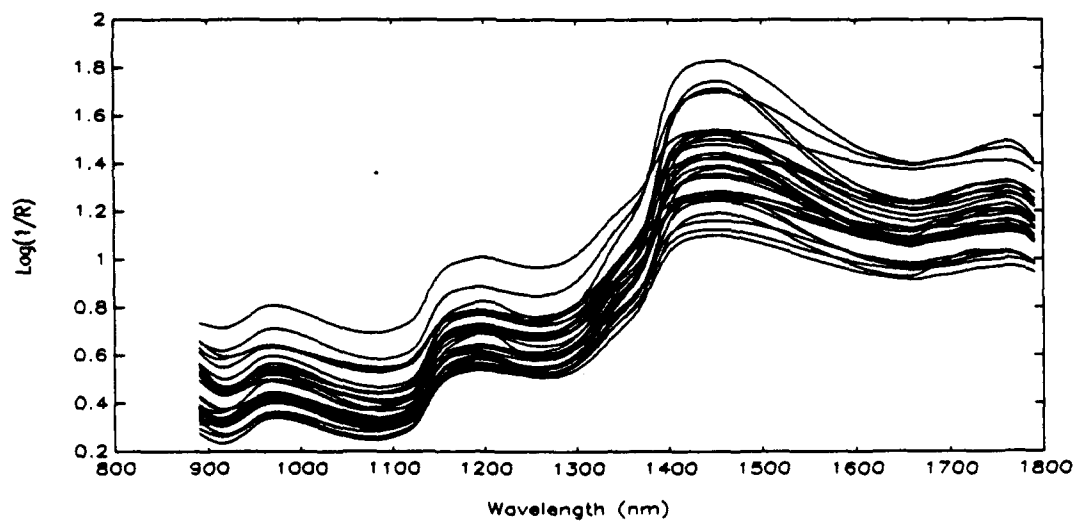
Figure 35.

Near infrared spectra of burn wounds. (a) shallow and (b) deep burns.
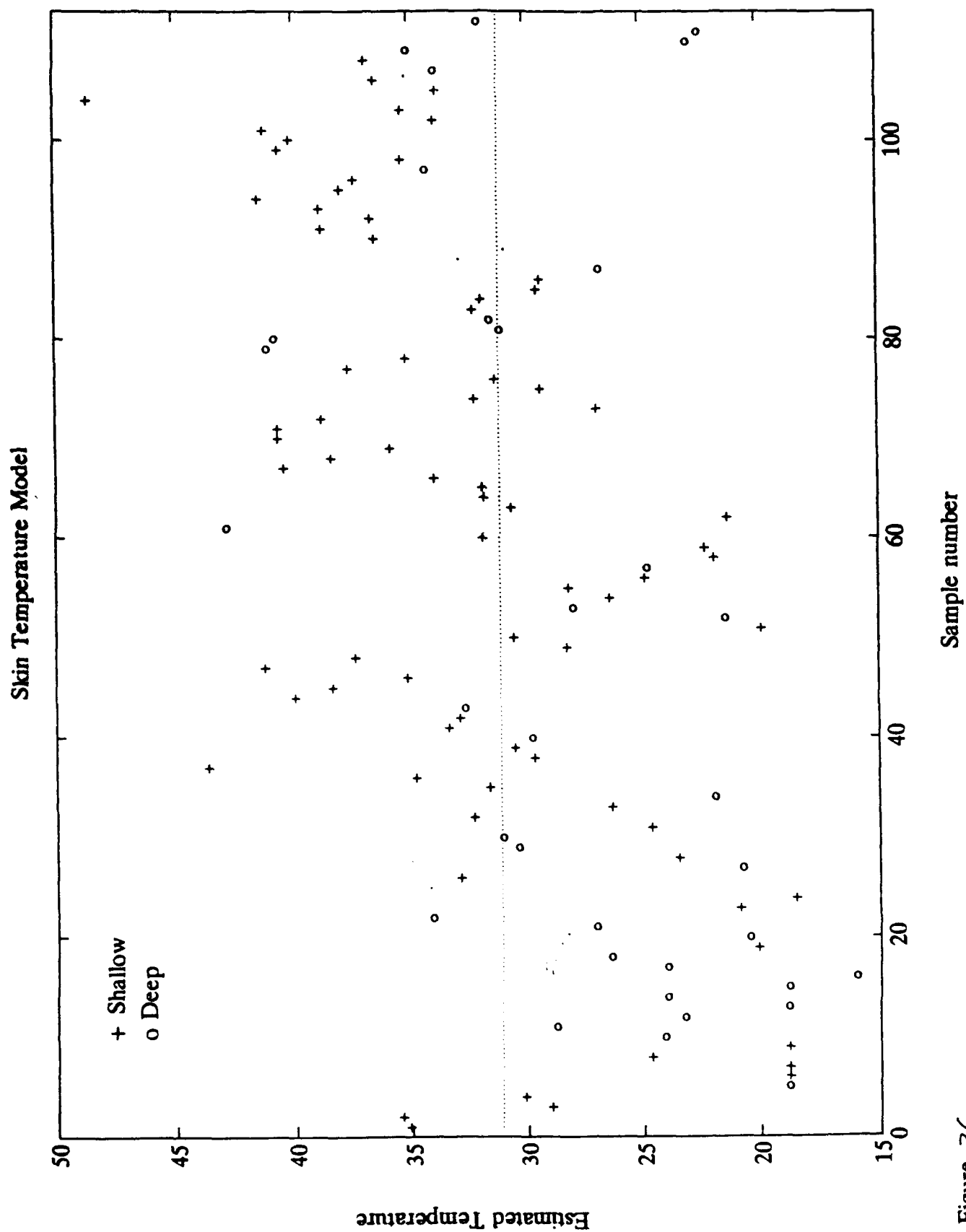
Figure 36

A
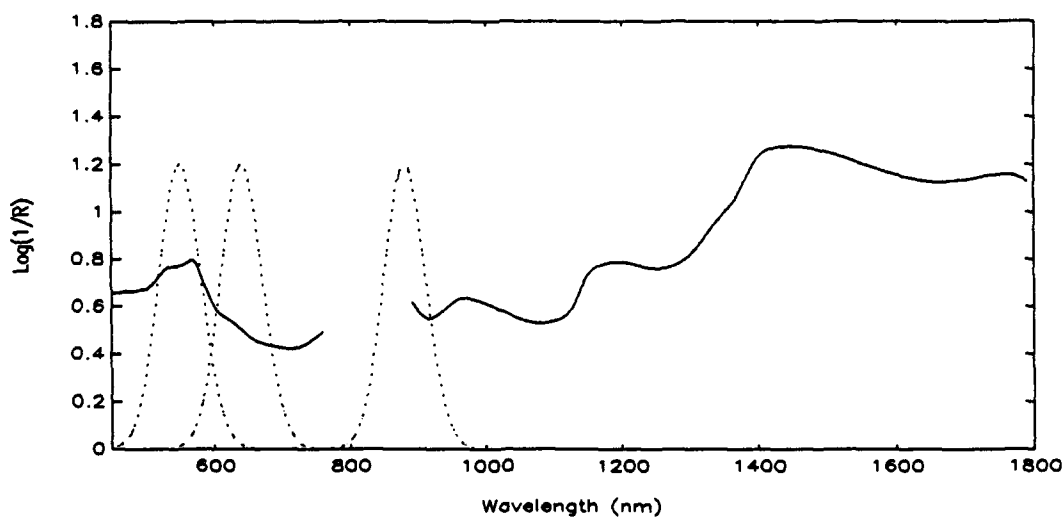
Figure 37.a Burn Depth Indicator Simulation. (—) a typical spectrum of a deep burn, and (• • •) the LED output functions.

B
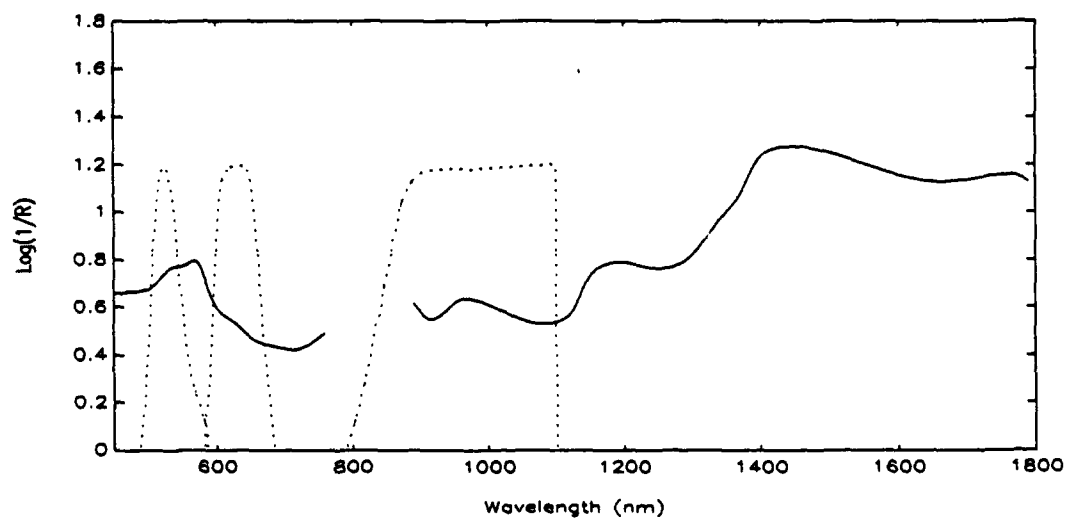
Figure 37.b Imaging Burn Depth Indicator Simulation. (—) a typical spectrum of a deep burn, and (• • •) the filter transmittance functions.

a)
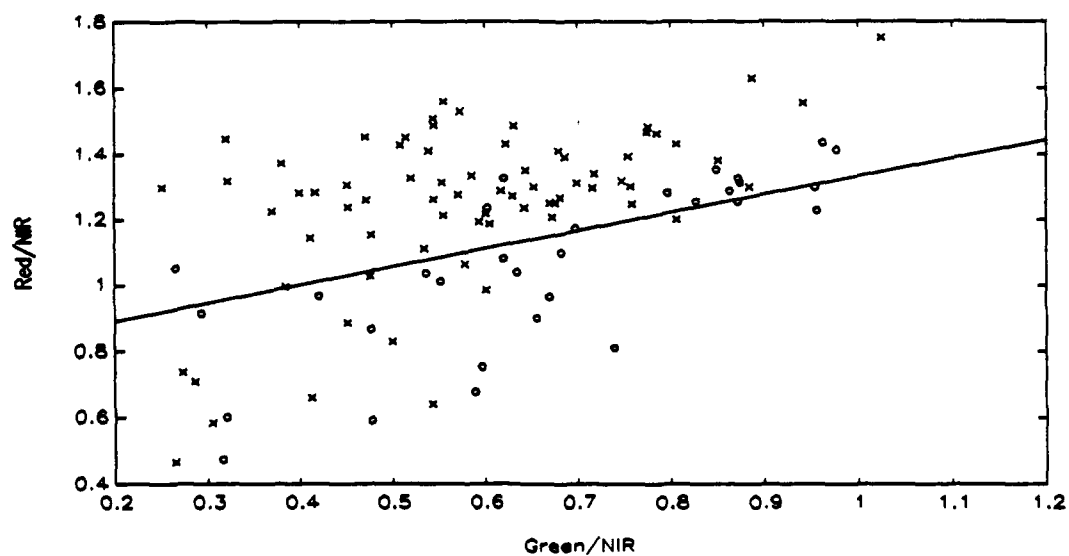
b)
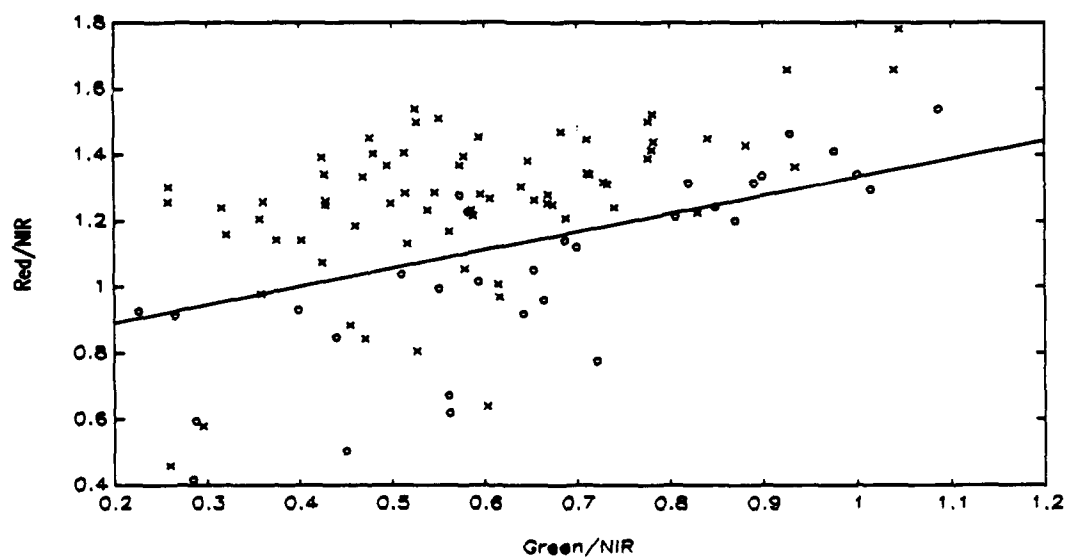
Figure 38. Simulated instrument responses. (a) the burn depth indicator, (b) the imaging burn depth indicator. (x) are responses for shallow burns, (o) for deep burns. (-) is the best discriminant line found by vanLiew.
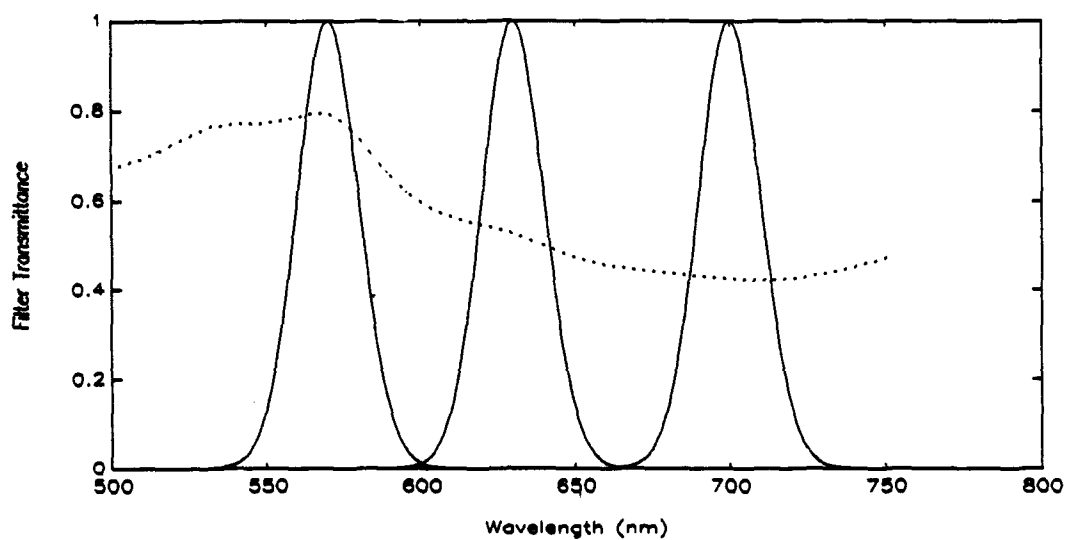
Figure 39. Filters chosen for the proposed IBDI model. (—) filters and (··) spectrum of a deep burn.
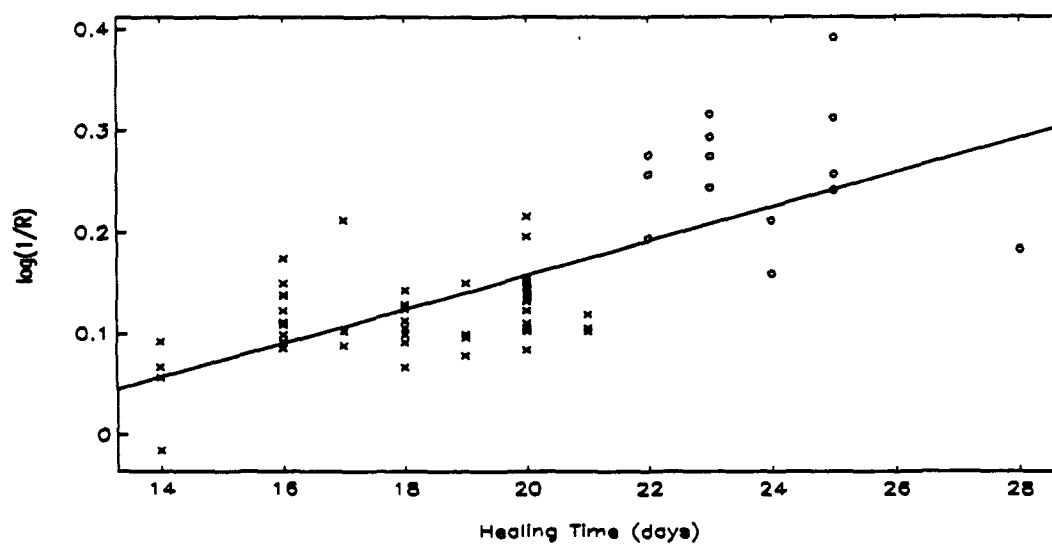
Figure 40. Simulated response of the proposed IBDI algorithm. (x) shallow and (o) deep injuries.

Figure 41

ABSORBANCE

WAVELENGTH, nm

WATER SPECTRA AFTER BASELINE SUBTRACTION

Figure 42

Figure 43

LOG FROM THE EIGENVALUES

RECIPROCAL TEMPERATURE, 1/T

x10⁻³

100

Figure 14

Figure 15

102

WAVELENGTH, nm

LOADINGS

Figure 16

Figure 47

CONCENTRATION

RECIPROCAL TEMPERATURE (1/K)

x10⁻³

ABSORBANCE

WAVELENGTH, nm

Figure 4B

WAVELENGTH(nm)

ARBITRARY UNITS
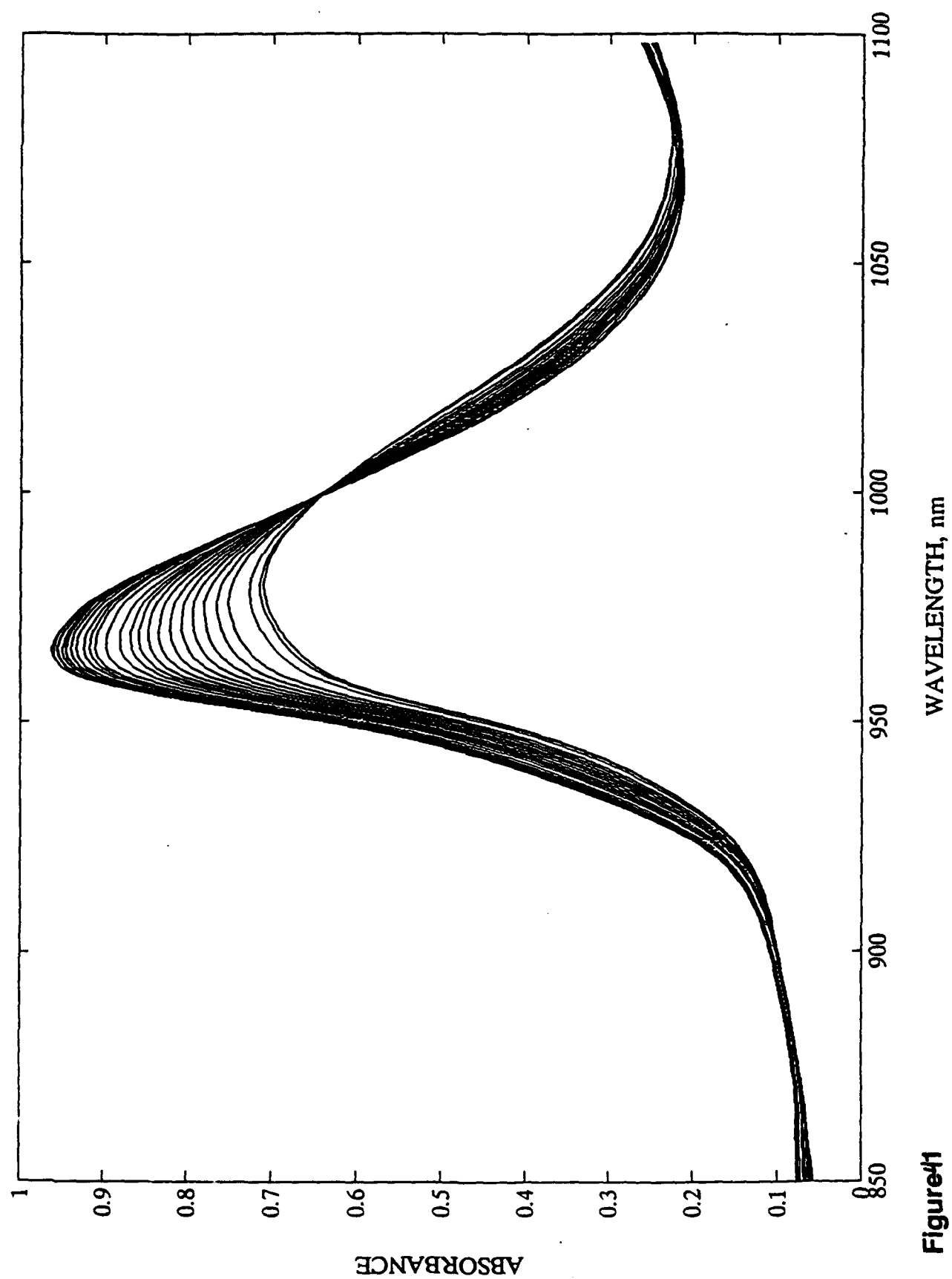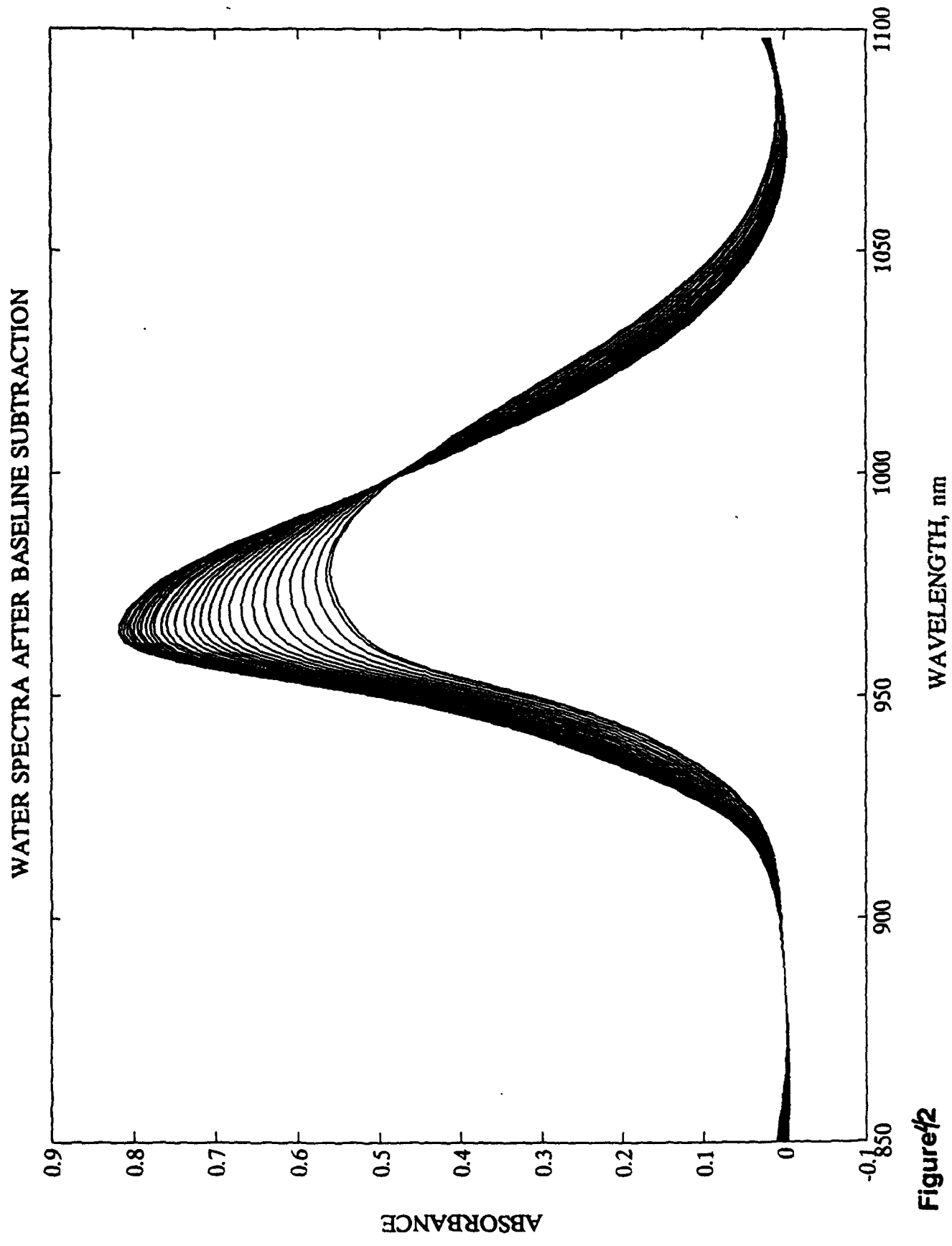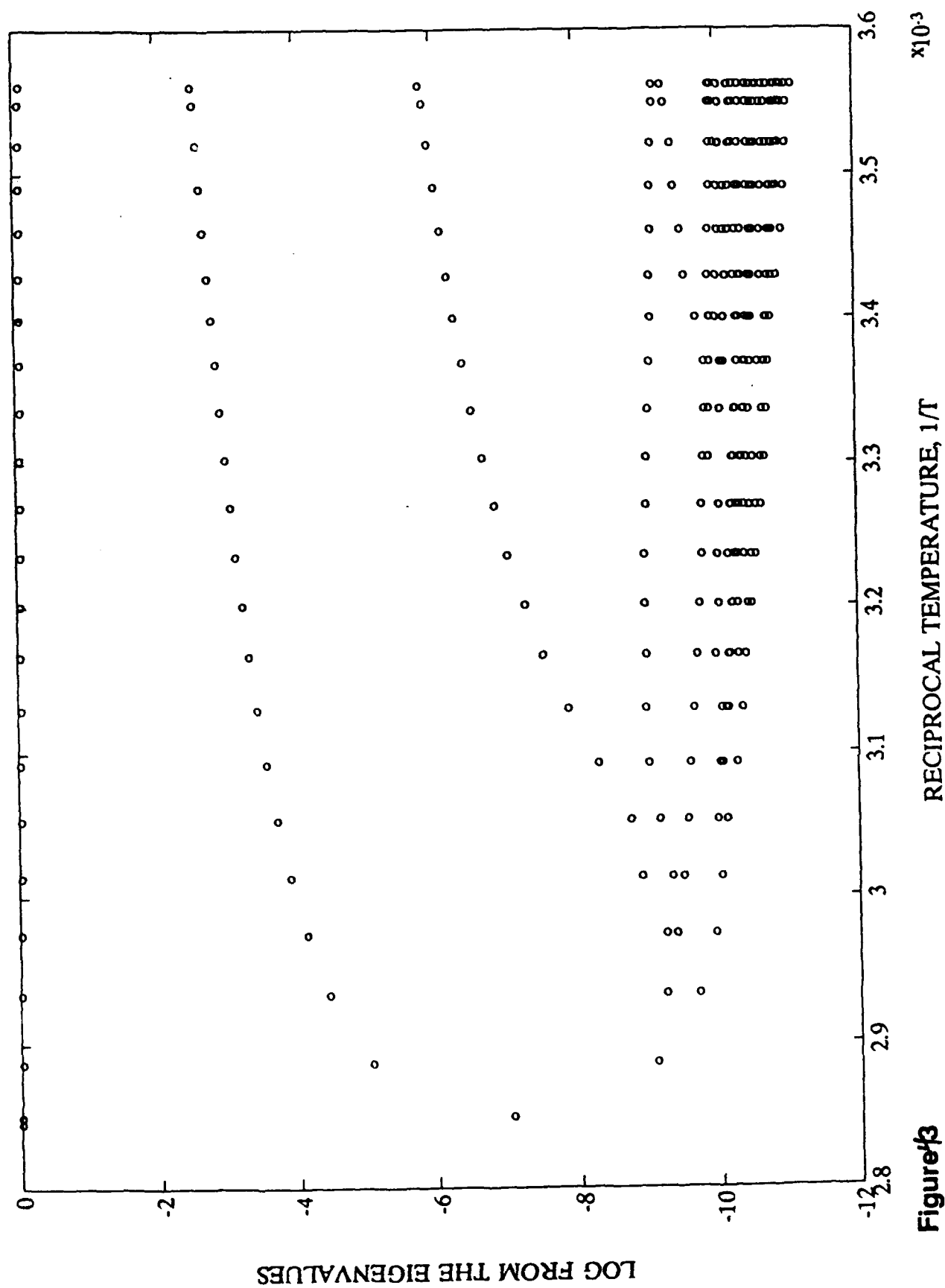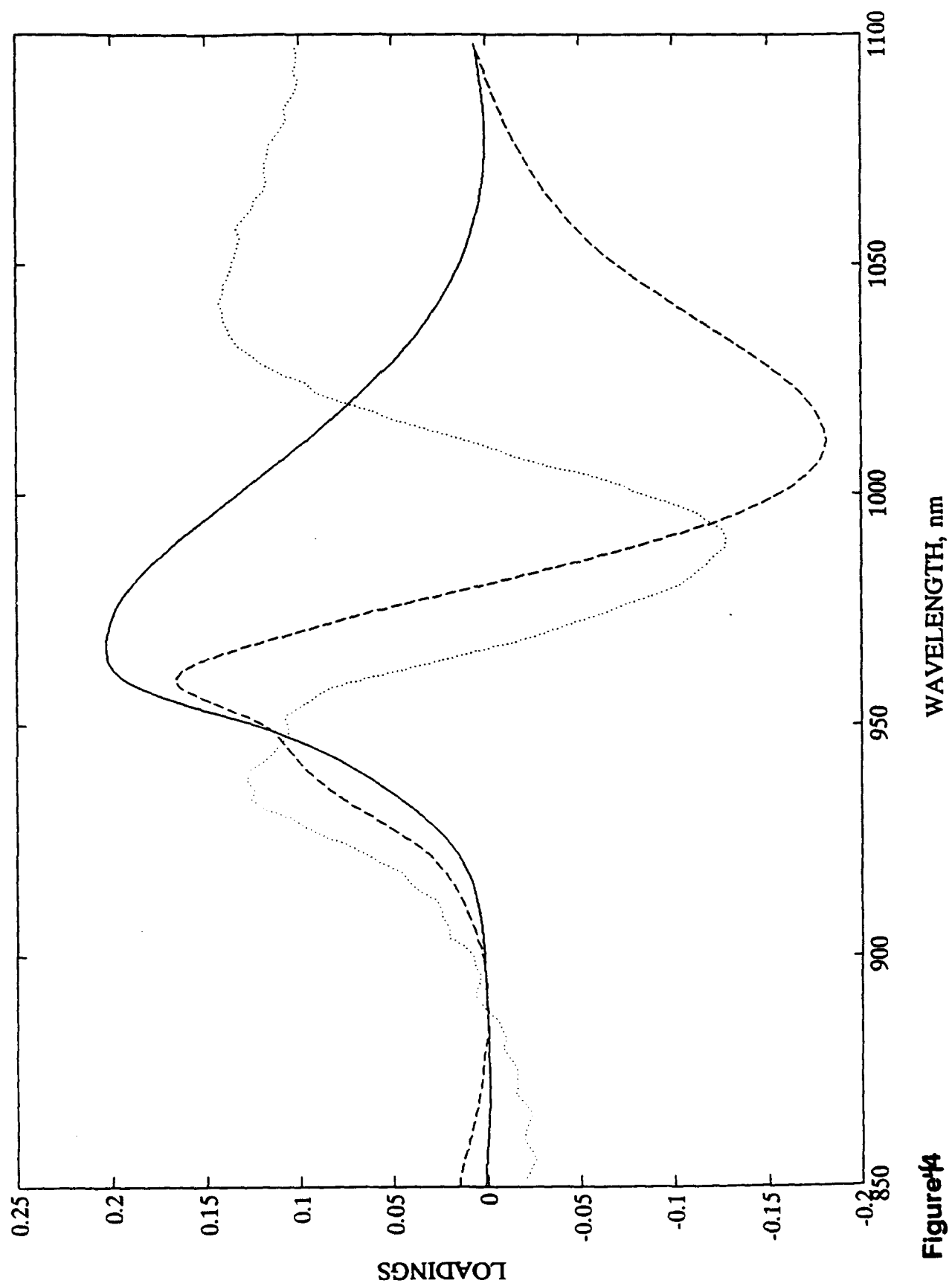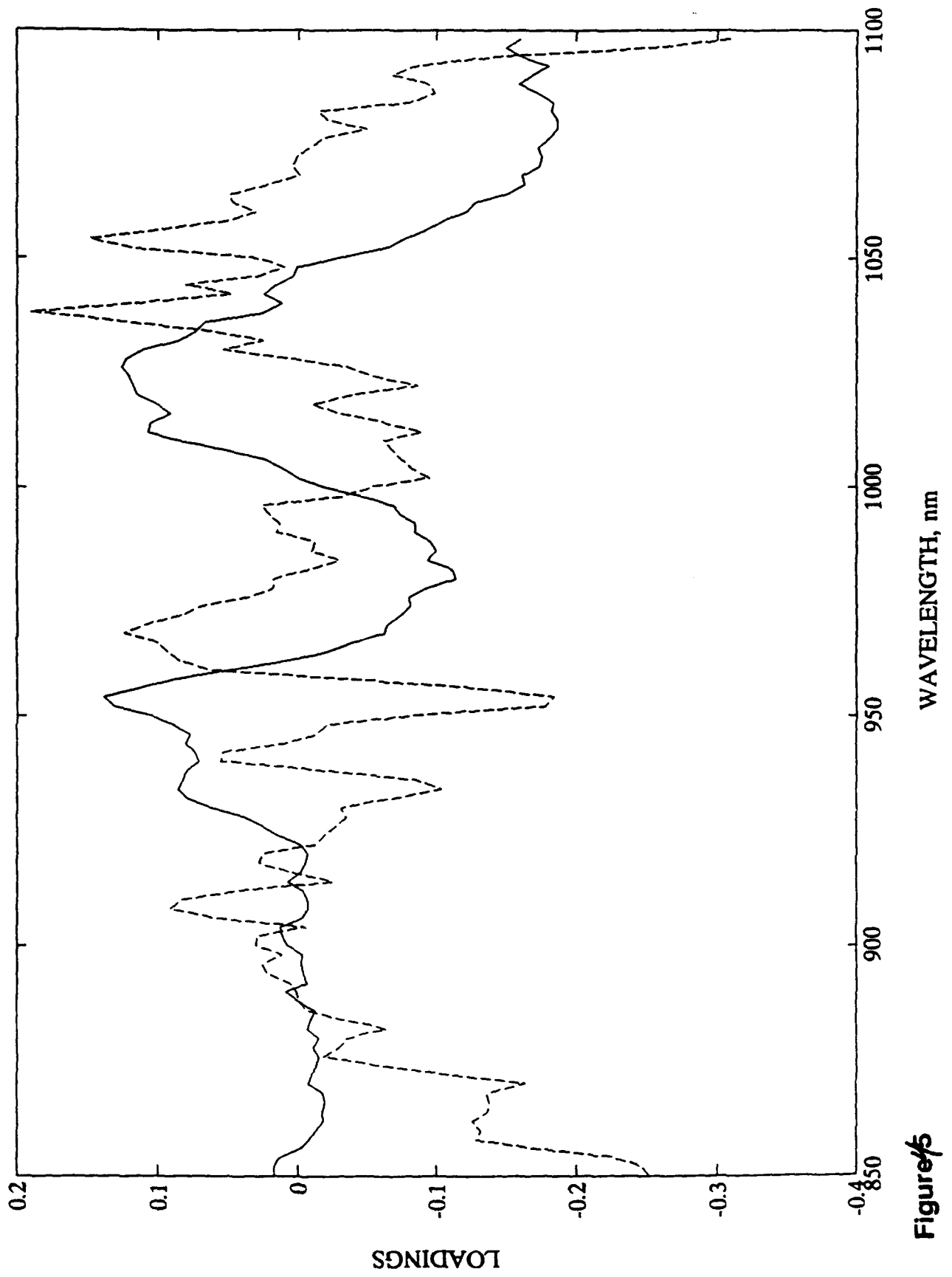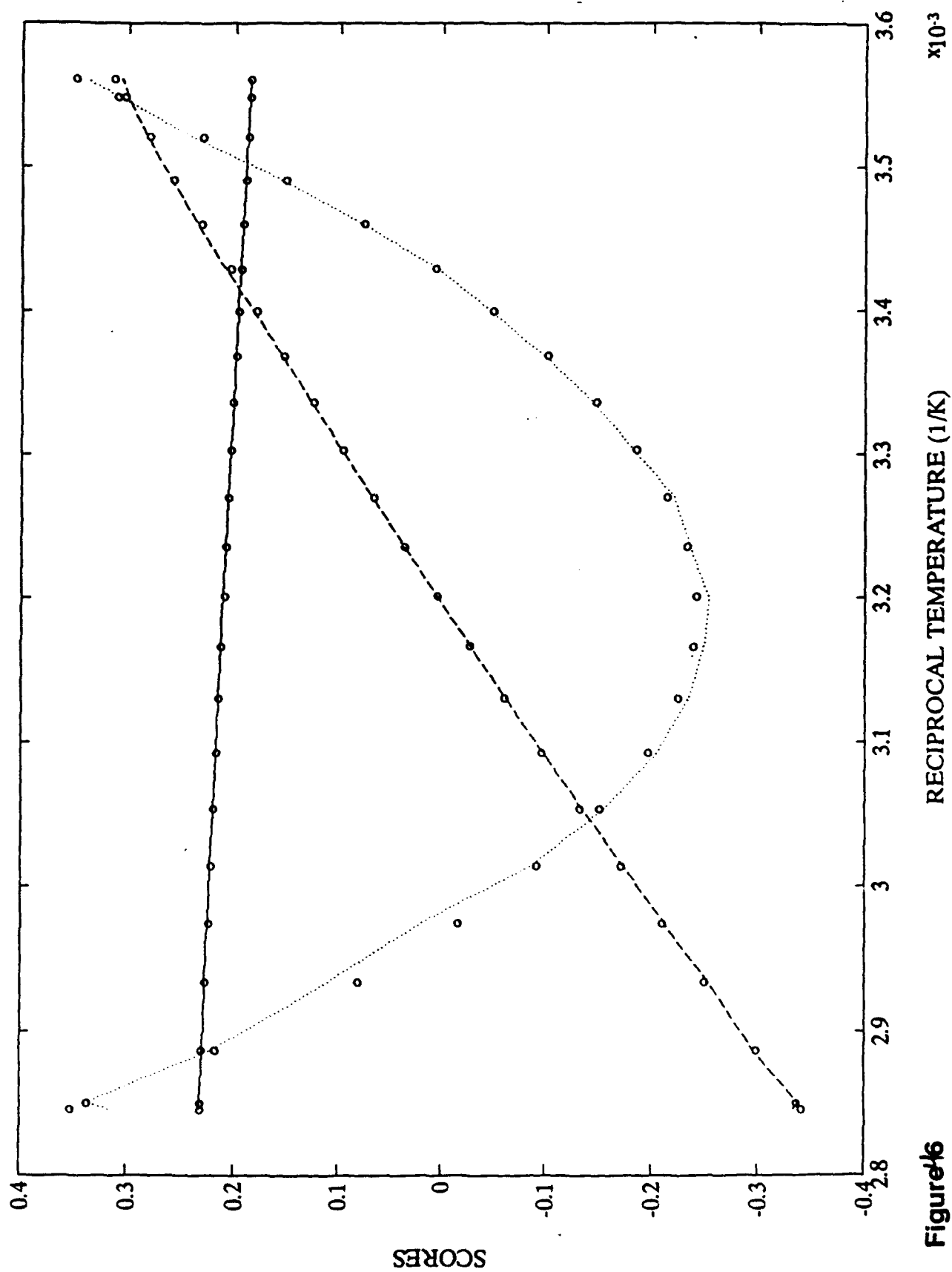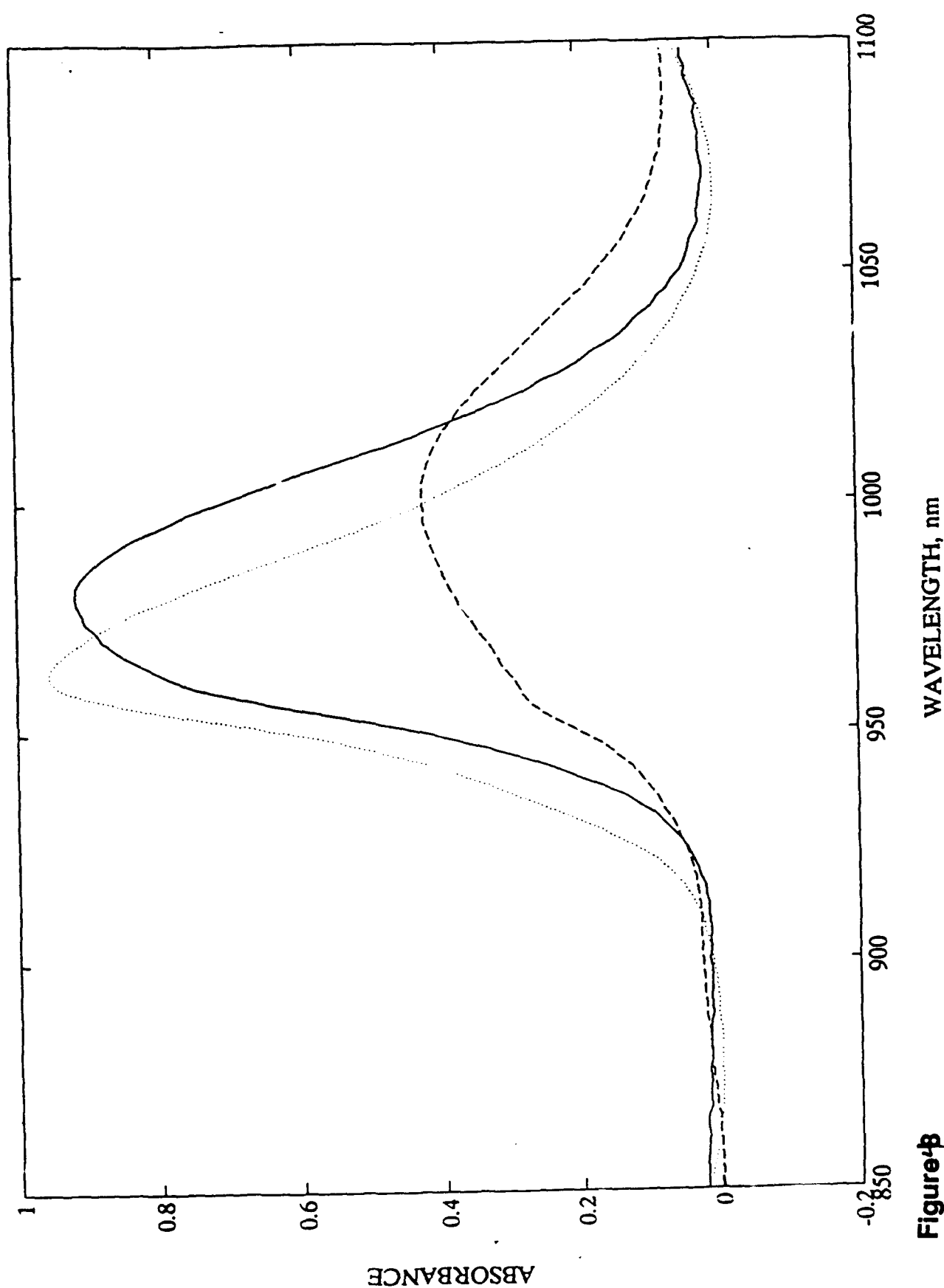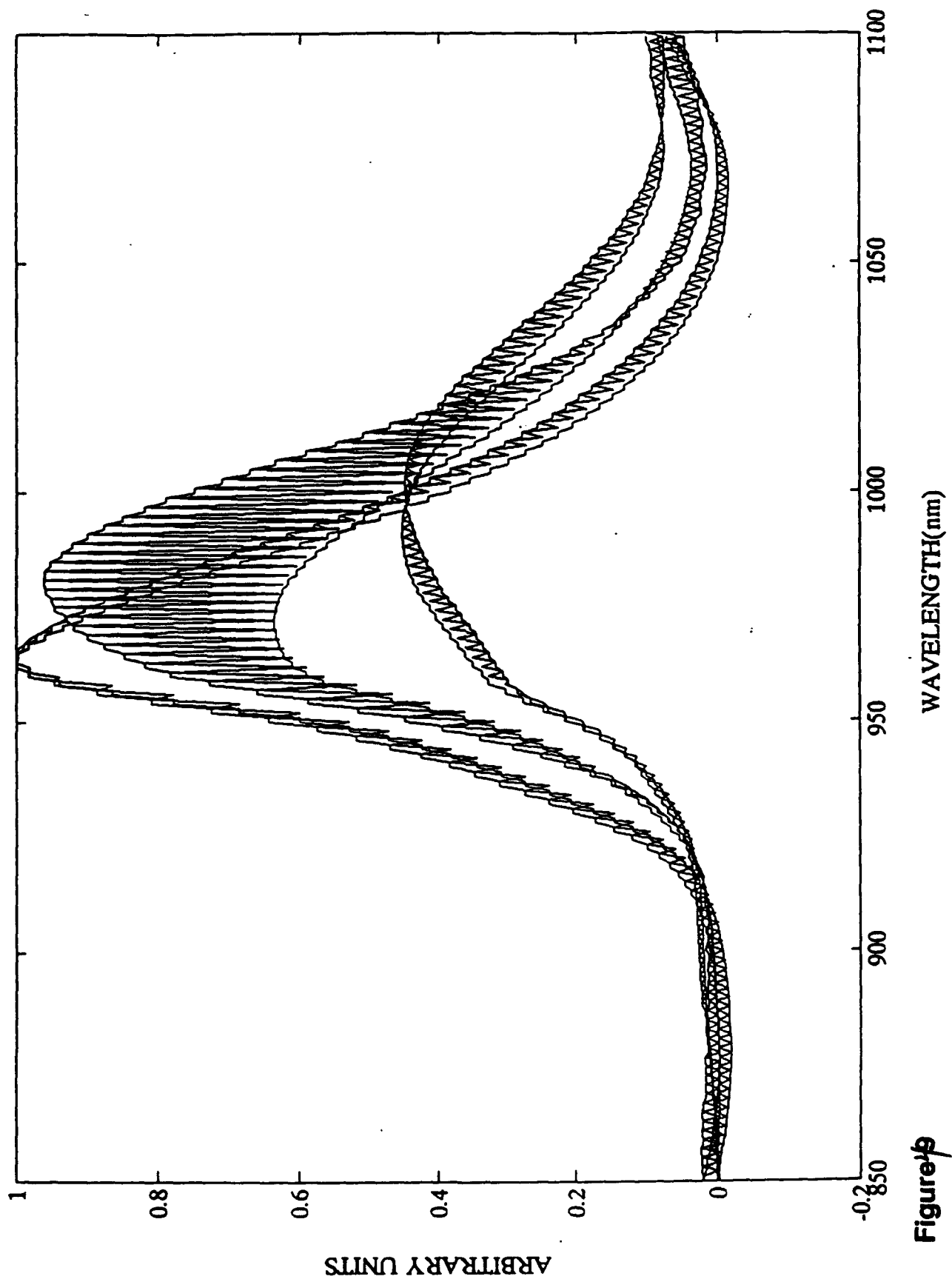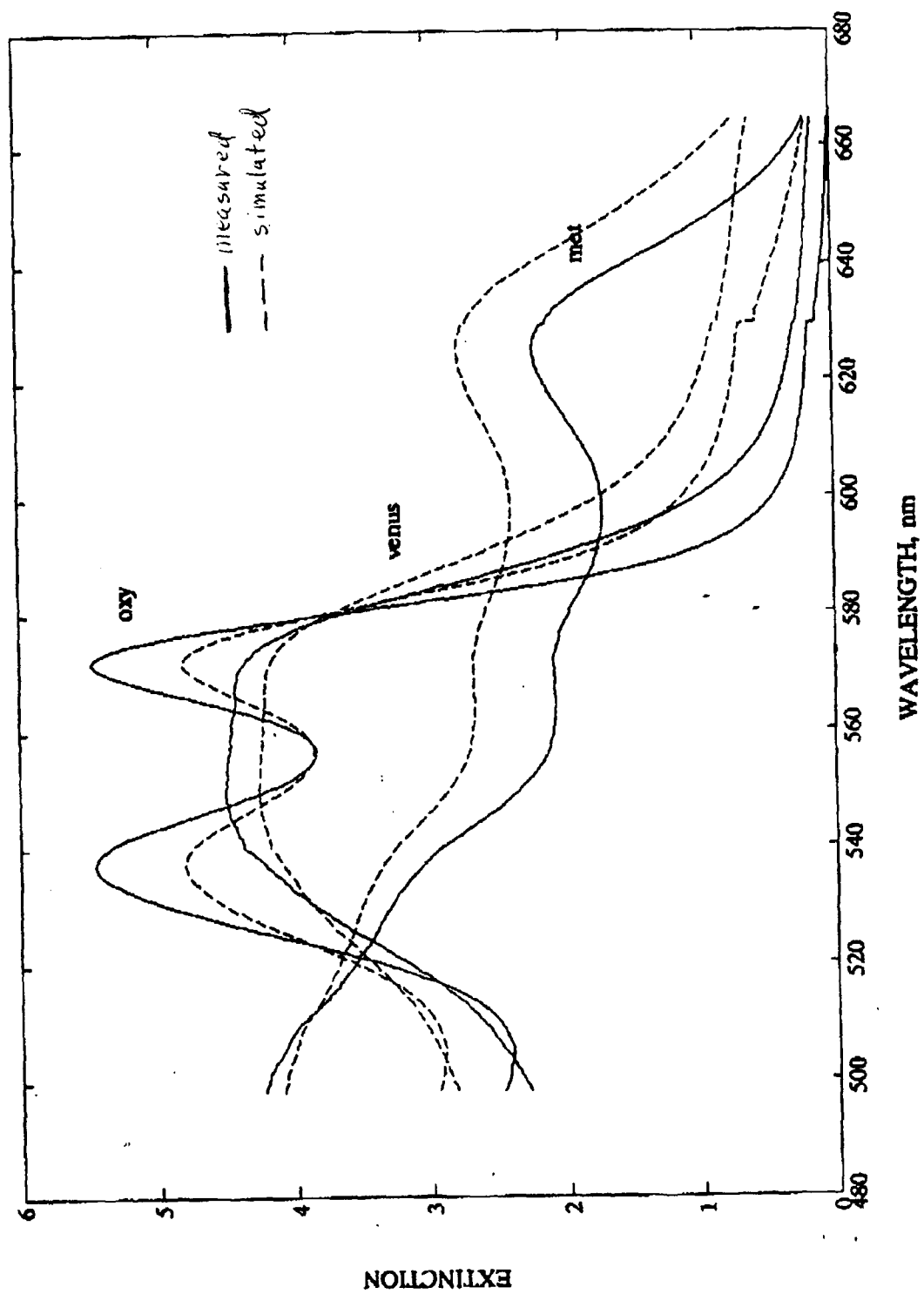
Figure 19

Figure 50
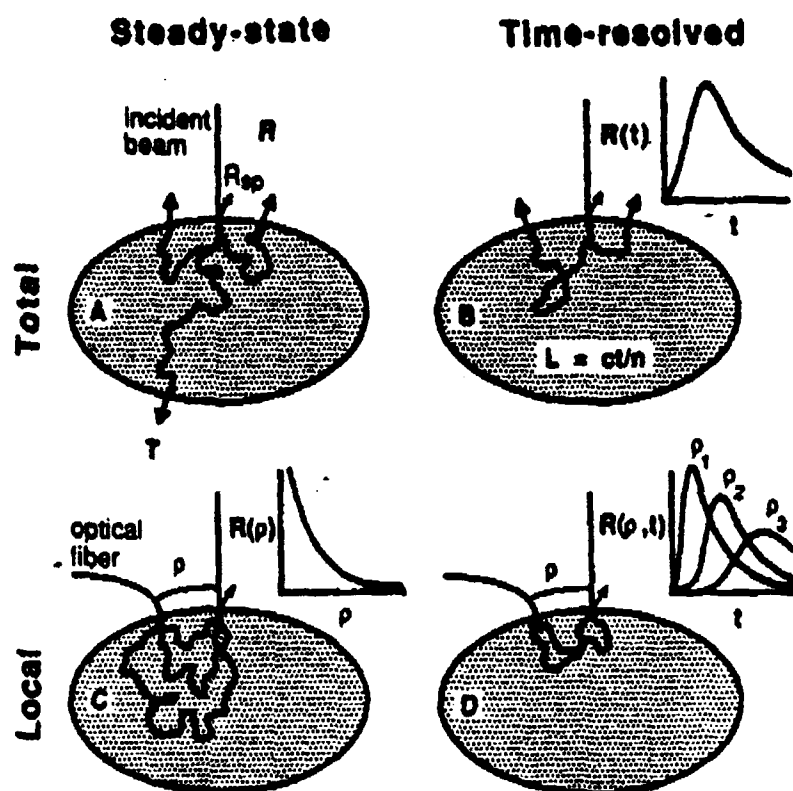
Fig. *51* Types of remittance measurements. The four types of remittance measurements are 1) steady-state measurement of the total remittance as either reflectance R and/or transmittance T, 2) time-resolved measurement of total remittance $R(t)$ as a function of time, 3) steady-state measurement of the local spatial distribution of remittance $R(\rho)$ along the tissue surface, and 4) the time-resolved measurement of the local spatial distribution of remittance $R(\rho, t)$ along the tissue surface as a function of time. The photon pathlength in the tissue is $L = ct/n$ where c is the *in vacuo* speed of light and n is the tissue refractive index.

CALCULATION OF PHOTON PATH

1. PHOTON INSERTED AT NORMAL INCIDENCE WITH AN INITIAL WEIGHTING OF ONE.

2. PATHLENGTH AND NEW WEIGHTING OF PHOTON CALCULATED FOR FIRST EVENT

3. ANGLE AND PATHLENGTH OF NEXT EVENT CALCULATED. NEW WEIGHTING ALSO DETERMINED.

4. REPEAT STEP 3 UNTIL PHOTON WEIGHT IS LESS THAN .0005
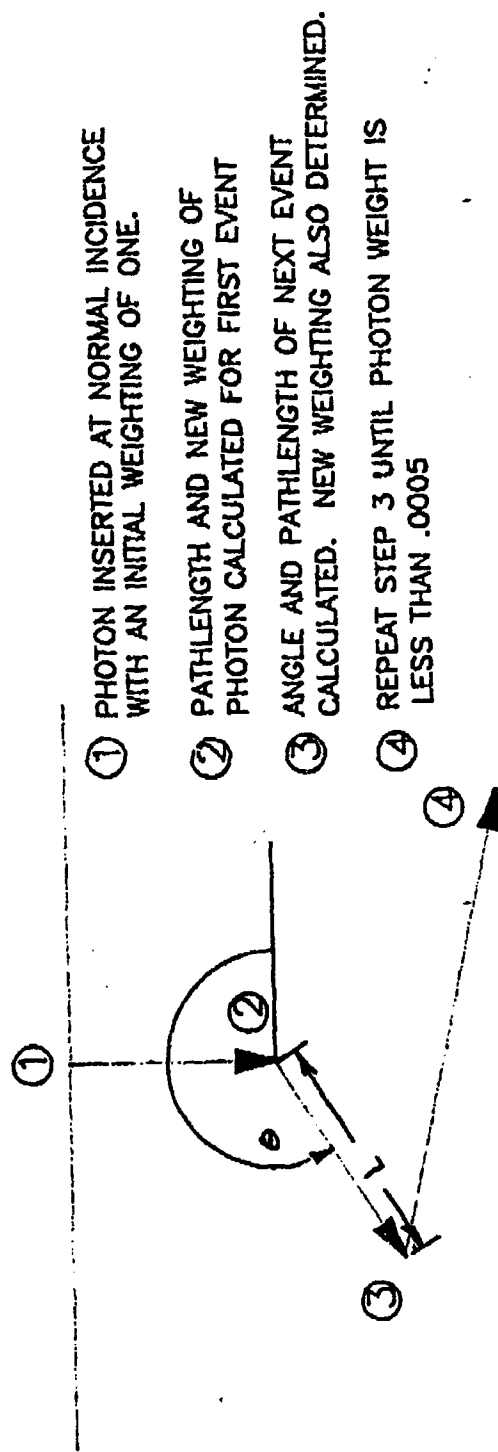
Figure 52

Figure 53

SIGMAtissue=5.e-12 cm2
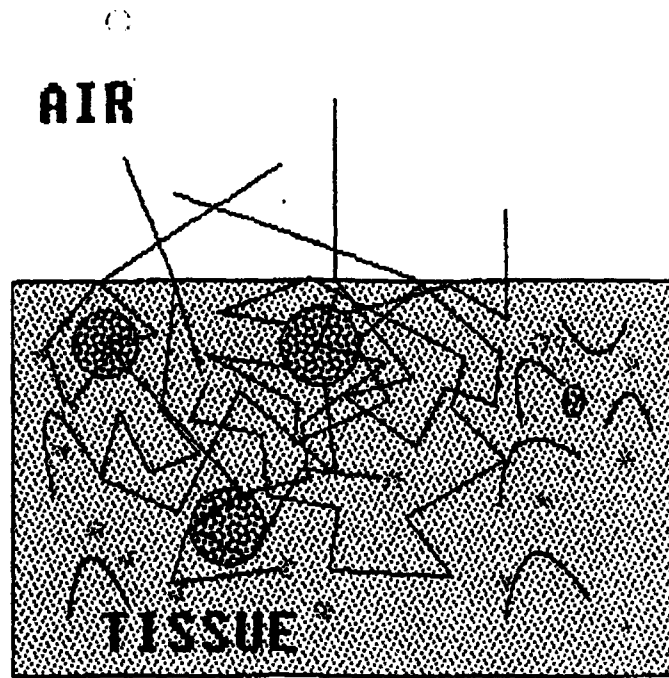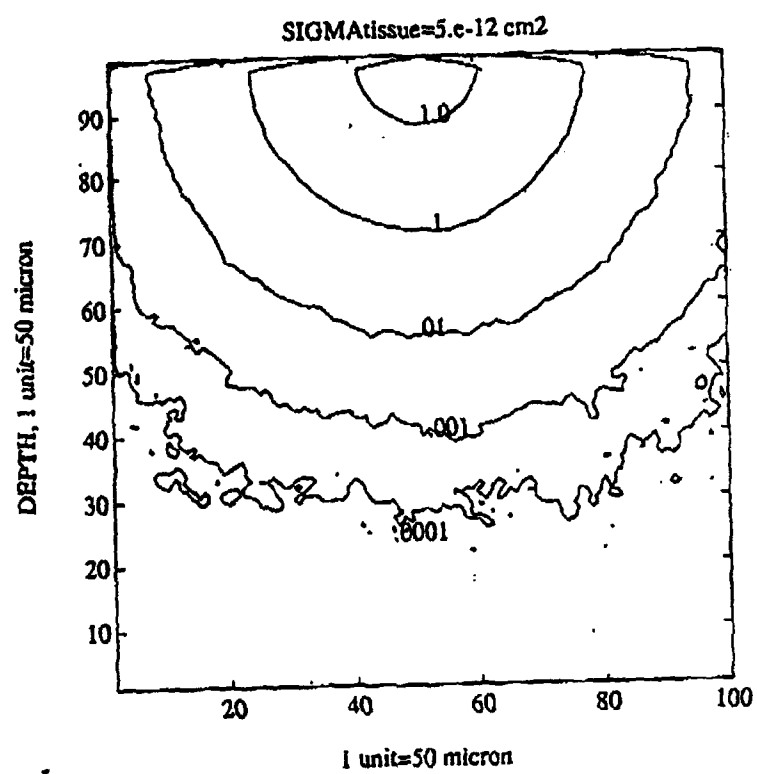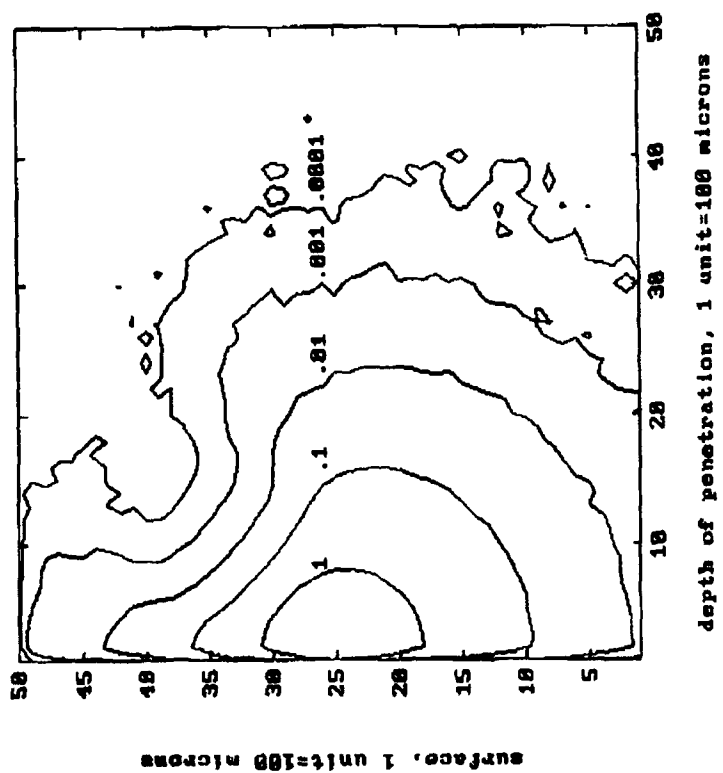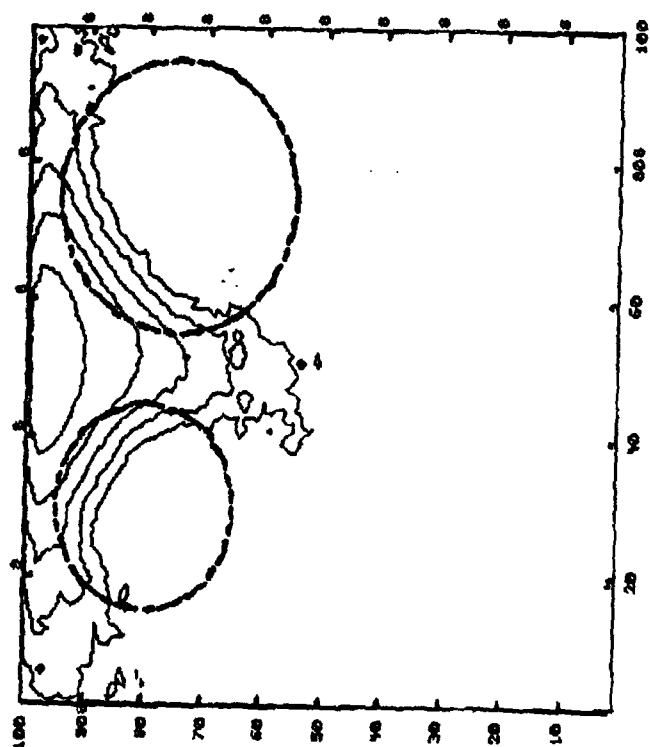
Figure 54

Figure 55

Figure 5G
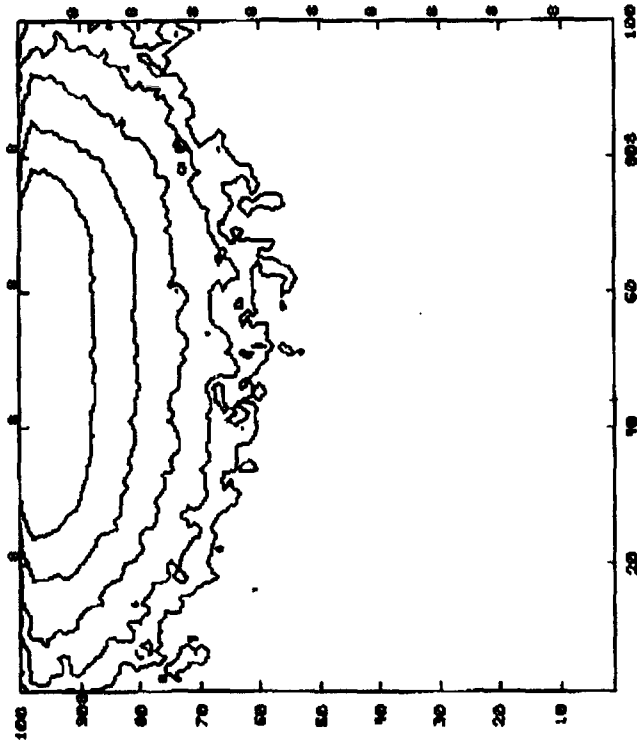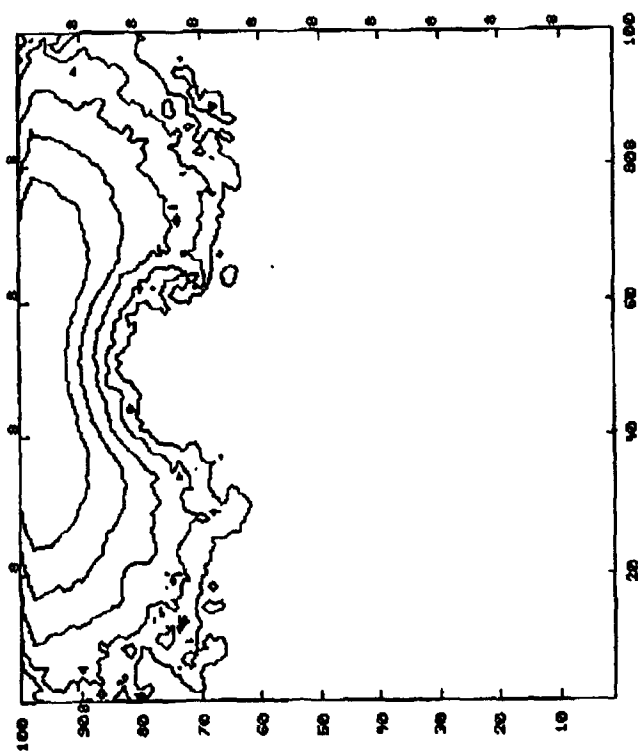
Figure 57

Figure 58
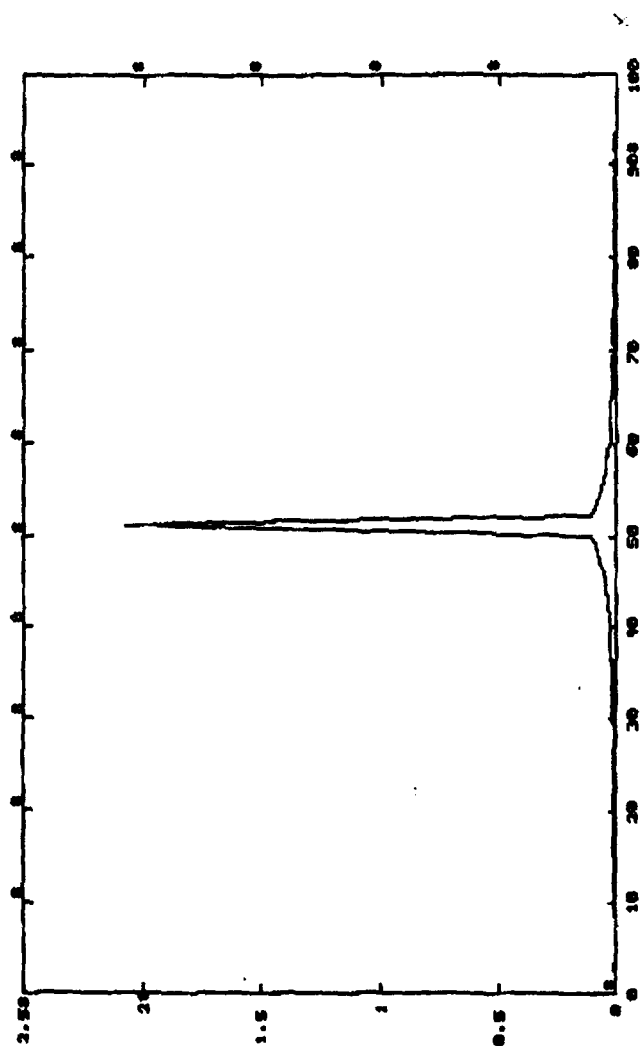
Figure 59
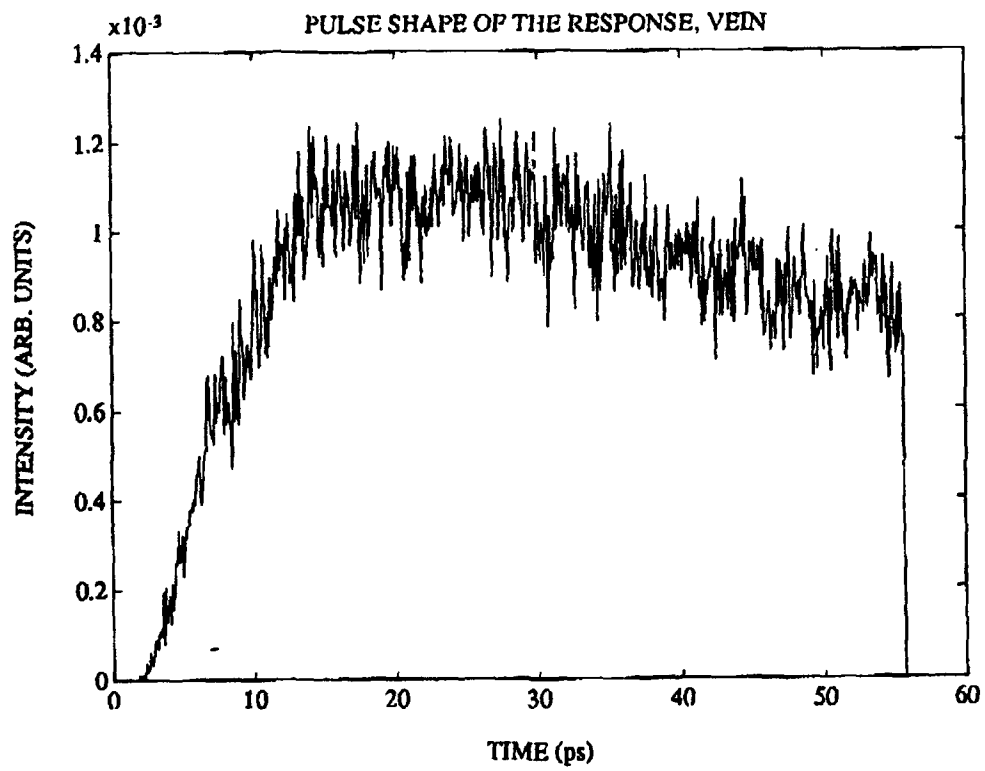
Figure 60

Appendix A
MATLAB Code for Rotation and Single-Plane Discrimination

```
function [Xmean,Scale,Rota] = spinc(X,C,Options)
%  X = all data (samples by variables, more samples than variables)
%  C = class vector, containing 1's and 2's only, 0's for ignored data
%OUTLINE
%  mean center
%  scale
%  rotate
%SUBROUTEINS NEEDED
%  std, varwt, fisherwt
%OPTIONS
%  1 scale (Range, Auto, Variance, Fisher, none)
%  2 rotation steps
%  3 number of rotated variables to calculate
%function [Xmean,Scale,Rota] = spinc(X,C,Options)


%%%%%%%%%%%%%%%%%%%%%%%%%%%%%%%%%%%%%%%%%%%%%%%%%%%%%%%
                   SETUP
%%%%%%%%%%%%%%%%%%%%%%%%%%%%%%%%%%%%%%%%%%%%%%%%%%%%%%%%
%*********************************************************** CHECK SIZES *****
%CHECK SIZES
 [m,n] = size(C);
   if m~=1 & n~=1, error('Rotation: Too many constituents.'), end
   if n>m, C=C'; [m,n]=size(C); end
 [np,nv] = size(X);
   if np~=m & nv~=m, error('Rotation: Incompatable matrices'), end
   if nv==m, X=X'; [np,nv]=size(X); end
 clear m n

 if any(C~=1 & C~=2 & C~=0), error('Rotation: Bad constituent values.'), end
 n1 = find(C==1);
   if length(n1)<2, error('Rotation: Too few of class #1'), end
 n2 = find(C==2);
   if length(n2)<2, error('Rotation: Too few of class #2'), end

 if ~any([1 2 3 4 5] == Options(1)),
   error('Rotation: Not a valid scaling option.')
 end
 if length(Options)<3, Options(3)=nv-1; end
 if Options(3)>nv-1, Options(3)=nv-1; end


%*********************************************************** SETUP MATRICES *****
%SETUP MATRICIES
 PhiStepSize = 1 / Options(2);
 Rota = eye(nv);                    %Main rotation matrix
 Cycle = 0;


%%%%%%%%%%%%%%%%%%%%%%%%%%%%%%%%%%%%%%%%%%%%%%%%%%%%%%%
%                   PREPROCESS DATA
```
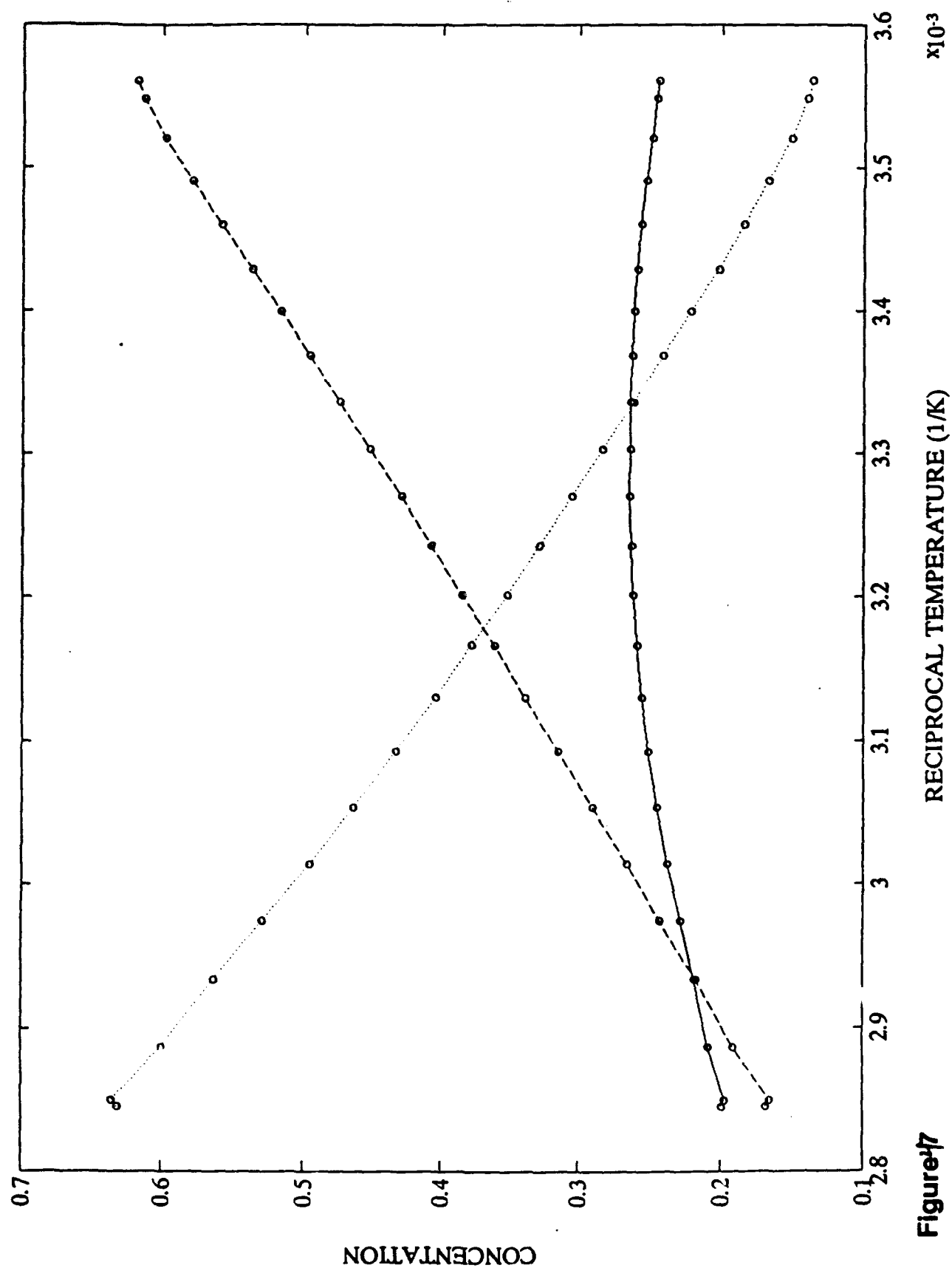
```
%%%%%%%%%%%%%%%%%%%%%%%%%%%%%%%%%%%%%%%%%%%%%%%%%
%***************************************************** MEAN-CENTER *****
%MEAN-CENTER
 Xmean = mean(X);
 Data  = X - ones(np,1)*Xmean;


%********************************************************************* SCALE *****
%SCALE  (Sharaf,Illman,Kowalski; "Chemometrics", p.193)

 if Options(1) == 1, %_____ Range scaling ____
   for i=1:nv, Scale(i) = 1 / max(abs(Data(:,i))); end
 elseif Options(1) ==2, %_____ Autoscaling ____
   for i=1:nv, Scale(i) = 1 / std(Data(:,i)); end
 elseif Options(1) ==3, %_____ Variance weights ____
   for i=1:nv, DataTmp(:,i)=Data(:,i)/max(abs(Data(:,i))); end
   [Scale] = varwt(DataTmp,C);
   for i=1:nv, Scale(i)=Scale(i)/max(abs(Data(:,i))); end
 elseif Options(1) ==4, %_____ Fisher weights ____
   for i=1:nv, DataTmp(:,i)=Data(:,i)/max(abs(Data(:,i))); end
   [Scale] = fisherwt(DataTmp,C);
   for i=1:nv, Scale(i)=Scale(i)/max(abs(Data(:,i))); end
 elseif Options(1) ==5,
   %no scaling
 end

 for i=1:nv, Data(:,i)=Data(:,i)*Scale(i); end



%%%%%%%%%%%%%%%%%%%%%%%%%%%%%%%%%%%%%%%%%%%%%%%%
%              ROTATE (two vectors at a time)
%%%%%%%%%%%%%%%%%%%%%%%%%%%%%%%%%%%%%%%%%%%%%%%%
for var1 = 1:Options(3),
for var2 = (var1+1):nv,
  %********************************************** TWO-VECTOR SUB-MATRICES *****
  %Choose vectors
    Data2 = Data(:,[var1,var2]);
    Rota2 = Rota(:,[var1,var2]);
    Axis  = sqrt(2) * [-1 1 -1 1] * max(max((Data2)));
  %********************************************************** ROTATE (loop) *****
  %Spin about [0 0]
  for phistep=1:Options(2),
    %+ + + + + + + + + + + + + + + + + + + + + + + + + + + + + + + + + + + + + Rotation Angle
    %Rotate data
     phi = phistep * PhiStepSize * (2*pi);
     rot = [cos(phi), -sin(phi); sin(phi), cos(phi)];
     data = Data2 * rot;
     rota = Rota2 * rot;
    %+ + + + + + + + + + + + + + + + + + + + + + + + + + + + + + + + + + + + DistanceBetweenClasses
    %Distance between classes
     [d,sign] = varwt(data(:,1),C);
     if sign == '-', d = -d; end        .
     dist(phistep) = d;
  end %for phistep
    %*********************************************** FIND MAXIMUM ANGLE *****
```

```
%Maximize distance
   %+ + + + + + + + + + + + + + + + + + + + + + + + + + + + + + + + + + + + + + + + + + + + + + + +  Angle
   maxphi = find( dist = = max(dist) );
     if length(maxphi) > 1,   maxphi = maxphi(1);   end
   phi = maxphi * PhiStepSize * (2*pi);
   rot = [cos(phi), -sin(phi); sin(phi), cos(phi)];
   %***************************************************  NEW SUB-MATRICES  *****
   %New sub-matrices
   %+ + + + + + + + + + + + + + + + + + + + + + + + + + + + + + + + + + +  New Matrices  + + + + +
   data = Data2 * rot;
   rota = Rota2 * rot;
   Data(:,[var1,var2]) = data;
   Rota(:,[var1,var2]) = rota;
 disp(['Rotation: Finnished variables ',int2str(var1),' and ',int2str(var2)])
end %for var2 = (var1 + 1):nv
end %for var1 = 1:(nv-1)
```

```
function [DataNew] = spinp(Xmean,Scale,Rota,Xp)
%function [DataNew] = spinp(Xmean,Scale,Rota,Xp)

[np ,nv] = size(Xp);

Data  = Xp - ones(np,1)*Xmean;
for i=1:nv,  Data(:,i)=Data(:,i)*Scale(i);  end
  Data = Data * Rota;
for i=1:nv,  Data(:,i)=Data(:,i)/Scale(i);  end
DataNew = Data  + ones(np,1)*Xmean;
```

```
function [discPoint] = disc(D,C);
% DISCc.m
% Finds the most discriminating point to separate two classes
% M.R.Balkenhol, 1/12/92
%
% D = data in two columns, column 1 is for discriminating
% C = class vector, 1's and 2's only
%
% minE  = best point (index and data value)
% E     = number of misclassifications [index, class1, class2, both classes]
%
%function [discPoint] = disc(D,C);


%%%%%%%%%%%%%%%%%%%%%%%%%%%%%%%%%%%%%%%%%%%%%%%%%%%%%%%%%
                INPUT and SETUP
%%%%%%%%%%%%%%%%%%%%%%%%%%%%%%%%%%%%%%%%%%%%%%%%%%%%%%%%%
minD = min(D(:,1));
maxD = max(D(:,1));
maxi = 300;
Error  = 999*ones(maxi+1,1);
Error2 = 999*ones(maxi+1,1);
Index  = zeros(maxi+1,1);


%%%%%%%%%%%%%%%%%%%%%%%%%%%%%%%%%%%%%%%%%%%%%%%%%%%%%%%%%
%            LOCATION OF MOST DISCRIMINATING POINT
%%%%%%%%%%%%%%%%%%%%%%%%%%%%%%%%%%%%%%%%%%%%%%%%%%%%%%%%%
%************************************************* Fewest Mispredictions *****
for i=1:maxi,
  j = i*(maxD-minD)/maxi + minD;
  e1 = sum( D(:,1)>=j & C==1 );
  e2 = sum( D(:,1)<j & C==2 );
  Error(i) = e1 + e2;
end

[minEs] = min(Error);
minIs = find(Error==minEs);

%********************************************* Smallest Sum-of-Squares Error *****
I=min(minIs) : max(minIs);
for i=I,
  j = i*(maxD-minD)/maxi + minD;
  n1 = find( D(:,1)>=j & C==1 );
  n2 = find( D(:,1)<j & C==2 );
  Error2(i) = sum(  ( D([n1;n2],1) - j ).^2  );
end

[minE,minI] = min(Error2);
  n = length(minE);
  if n > 1, minE = minE( round(n/2), : );  end

discPoint = minI*(maxD-minD)/maxi + minD;
```

```
function [Cest,ep] = discp(disc,Dp,Cp);
% DISCp.m
% Sorts a predictions set (Class1 < disc, Class2 > disc)
% M.R.Balkenhol, 1/12/92
%
% Dp = data in two columns, column 1 is for discriminating
% Cp = class vector, 1's and 2's only (optional)
%
% disc = discriminating point, minE(1,2) from disc.m
%
%function [Cest] = discp(disc,Dp,Cp);


%%%%%%%%%%%%%%%%%%%%%%%%%%%%%%%%%%%%%%%%%%%%%%%%%%%
              INPUT and SETUP
%%%%%%%%%%%%%%%%%%%%%%%%%%%%%%%%%%%%%%%%%%%%%%%%%%%
[np,nv] = size(Dp);


%%%%%%%%%%%%%%%%%%%%%%%%%%%%%%%%%%%%%%%%%%%%%%%%%%%
%              SORTING DATA POINTS with respect to DISC
%%%%%%%%%%%%%%%%%%%%%%%%%%%%%%%%%%%%%%%%%%%%%%%%%%%
for i=1:np,
  if Dp(i,1) < disc,
    Cest(i) = 1;
  elseif Dp(i,1) > disc,
    Cest(i) = 2;
  else
    Cest(i) = 0;
  end
end
Cest = Cest';


%%%%%%%%%%%%%%%%%%%%%%%%%%%%%%%%%%%%%%%%%%%%%%%%%%%
%                DISPLAY (if Cp exists)
%%%%%%%%%%%%%%%%%%%%%%%%%%%%%%%%%%%%%%%%%%%%%%%%%%%
if nargin > 2,
  errors = find( Cest ~= Cp );
  plot(find(Cest==1), Dp(Cest==1,1), 'c6+',..
       find(Cest==2), Dp(Cest==2,1), 'rx',..
       [1 np], [disc disc], 'b:',..
       errors, Dp(errors,1), 'c5o')
  ep = length(errors);
end
```

PROGRAM SVEIN   Appendix B

```
      REAL NO,NT
      DIMENSION A(2), FLUX(100,100),ALR(11,600),ALT(11,600)
      INTEGER*4 IX,IY
      OPEN(UNIT=1,FILE='FVEIN.GGP',STATUS='NEW')
      OPEN(UNIT=2,FILE='LVEIN.GGP',STATUS='NEW')

C DEFINITION OF PARAMATERSS

C FLUX ARRAY THAT IS CELL HISTORIES ARE STORED TO CALCULATE
C      A GRAPHIC DISPLAY OF FLUX.

C ALR,ALT ARRAYS THAT RECORD PHOTON PATHLENGTH ABOVE AND BELOW
C      THE TISSUE INTERFACE

C THETA ANGLE THAT PHOTON WILL MOVE NEXT
C PLNGTH PATH LENGTH THAT PHOTON TRAVELS IN ONE STEP
C RHO DENSITY OF PARTICAL IN WHOLE BLOOD
C SIGMSV SCATTERING CROSS SECTION OF VEIN
C SIGMAV ABSORPTION CROSS SECTION OF VEIN
C SIGMAS SCATTERING CROSS SECTION OF TISSUE
C SIGMAA ABSORPTION CROSS SECTION OF TISSUE
C COEFS SCATTERING COEFFICIENT TISSUE
C COEFSV SCATTERING COEFFICIENT VEIN
C COEFA ABSORPTION COEFFICIENT TISSUE
C COEFAV ABSORPTION COEFFICIENT VEIN
C THETAC CRITICAL ANGLE CALCULATE FOR SURFACE
C      TISSUE BOUNDARY

C NO     INDEX OF REFRACTION OUTSIDE TISSUE
C NT     INDEX OF REFRACTION OF TISSUE
C XO,YO COORDINATES OF CENTER OF CIRCULAR VEIN
C RADIUS RADIUS OF CIRCLE
C SLNGTH ACCUMULATIVE PATH LENGTH
C NPHOTN NUMBER PHOTONS TO BE INJECTED INTO TISSUE
C INTIALIZATION OF PARAMETERS
      DO 300 I = 1,100
      DO 300 J = 1,100
      FLUX(J,I) = 0.0
 300  CONTINUE
      DO 301 I = 1,11
      DO 301 J = 1,600
      ALR(I,J) = 0.0
      ALT(I,J) = 0.0
 301  CONTINUE
          N = 2
          A(1) = 0.0
          A(2) = 0.0
          THETA = 0.0
          PLNGTH = 0.0
          RHO = 5.0E03
          CALL SECNDS(ISEED)
          NPHOTN = 10000
          SIGMSV = 56.58
          SIGMAV = 0.542
          HEMAT = 0.41
```

```
        ELSE

        CALL TISSUE(RANDM1,RANDM2,COEFA,COEFS,X,Y,PLNGTH,WEIGHT,THETA)
        ENDIF
        SLNGTH = SLNGTH + PLNGTH
        IX    = INT(AINT(X/10.0))
        IY    = INT(ABS(AINT(Y/10.0))) + 1
        ENDIF

C TERMINATION OF PHOTON IN TISSUE

        IF (WEIGHT .LT. .0005)THEN
        WEIGHT = 1.0
        GOTO 10
        ENDIF
        IF(Y .LT. 0.0)THEN
        IF(IX .GT. 49 .OR. IX .LE. -50 .OR. IY .GT. 100)THEN
        INC = INC + 1
        ELSE
        FLUX(IX+51,IY+1) = FLUX(IX+51,IY+1) + WEIGHT
        INC = INC+1
        ENDIF
        GOTO 1
        ELSE

C IF PHOTON IS AT SURFACE INTERFACE PROGRAM CALLS
C SUBROUTINE REFLECT WHICH DETERMINES HOW THE PHOTON
C WILL BE REFLECTED

        CALL REFLECT(NO,NT,THETA,THETAC,Y,X,WT,WR,THETAI,THETAT
     1,RPERP,RPAR,XS)
        IY = INT(ABS(AINT(Y))) + 1
        IXS = INT(AINT(XS/10.0))
        IF(ILNGTH .LT. 600)THEN
        ILNGTH = INT(SLNGTH/10.0)
        ALT(1,ILNGTH) = ALT(1,ILNGTH) + WEIGHT*WT
        ALR(1,ILNGTH) = ALR(1,ILNGTH) + WEIGHT*WR
        IA = ABS(INT(XS/50.0)) + 2
        IF(IA .LE. 11)THEN
        ALT(IA,ILNGTH) = ALT(IA,ILNGTH) + WEIGHT*WT
        ALR(IA,ILNGTH) = ALR(IA,ILNGTH) + WEIGHT*WR
        ENDIF
        ENDIF

C RECORDING OF WHERE PHOTON HAS TRAVELED DURING THIS INCREMENT

        IF(IXS .GT. 49 .OR. IXS .LT. -50)GOTO 111
        IF(IX .GT. 49 .OR. IX .LE. -50 .OR. IY .GT. 100)GOTO 111
        IF(WT .EQ. 1.0) THEN
        FLUX(IXS+51,1) = FLUX(IXS+51,1) + WEIGHT
        GOTO 111
        ENDIF
        IF (WR .NE. 1.0)THEN
        FLUX(IXS+51,1) = FLUX(IXS+51,1) + WEIGHT*WT
        FLUX(IX +51,IY +1) = FLUX(IX +51,IY +1) + WEIGHT*WR
        ELSE

        FLUX(IX+51,IY +1) = FLUX(IX +51,IY +1) + WEIGHT
        ENDIF
111  CONTINUE
```

```fortran
      ENDIF
      GOTO 1
10    CONTINUE

C CONSTRUCTION OF OUTPUT FILE THAT BUILDS A FILE WHICH
C CONTAINS INFORMATION ON THE FLUX DENSITY

      DO 30 IY = 1,100
      WRITE(1,'("IY",I4,/,"IY IX FLUX")')(IY-1)*10
      DO 20 IX = 1,100
      WRITE(1,'(I4,1X,I4,1X,G13.6)')(IY-1)*10,(IX-51)*10,FLUX(IX,IY)/
     !NPHOTN
20    CONTINUE
      WRITE(1,'("*EOF")')
30    CONTINUE

C CONSTRUCTION OF FILE THAT OUTPUTS INFORMATION OBTAINED FOR
C HISTOGRAMS OF TOTAL PHOTON PATHLENGTH BEFORE READMITTANCE
C AT THE TISSUE SURFACE INTERFACE

      WRITE(2,'(/,"OUTSIDE",/,"LENGTH ALL D050 D50100",
     !1X,"D100150 D150200")')
      DO 303 J = 1,600
      WRITE(2,'(6(G13.6,1X))')REAL(J)*10.0,ALT(1,J)/NPHOTN
     !,ALT(2,1)/NPHOTN,ALT(3,J)/NPHOTN,ALT(4,1)/NPHOTN,ALT(5,J)/NPHOTN
303   CONTINUE
      WRITE(2,'("*EOF")')
      WRITE(2,'("OUTSIDE2",/,"LENGTH D200250 D250300 D300350",
     !1X,"D350400 D400450 D450500")')
      DO 304 K = 1,600
      WRITE(2,'(7(G13.6,1X))')REAL(K)*10.0,ALT(6,K)/NPHOTN,
     !ALT(7,K)/NPHOTN,ALT(8,K)/NPHOTN
     !,ALT(9,K)/NPHOTN,ALT(11,K)/NPHOTN,ALT(11,K)/NPHOTN
304   CONTINUE
      WRITE(2,'("*EOF")')
      WRITE(2,'(/,"INSIDE",/,"LENGTH ALL D050 D50100",
     !1X,"D100150 D150200")')
      DO 305 I = 1,600
      WRITE(2,'(6(G13.6,1X))')REAL(I)*10.0,ALR(1,I)/NPHOTN,
     !ALR(2,I)/NPHOTN,ALR(3,I)/NPHOTN,ALR(4,I)/NPHOTN,ALR(5,I)/NPHOTN
305   CONTINUE
      WRITE(2,'("*EOF")')
      WRITE(2,'("INSIDE2",/,"LENGTH D200250 D250300 D300350",
     !1X,"D350400 D400450 D450500")')
      DO 306 I = 1,600
      WRITE(2,'(7(G13.6,1X))')REAL(I)*10.0,ALR(6,I)/NPHOTN,
     !ALR(7,I)/NPHOTN,ALR(8,I)/NPHOTN
     !,ALR(9,I)/NPHOTN,ALR(10,I)/NPHOTN,ALR(11,I)/NPHOTN
306   CONTINUE
      WRITE(2,'("*EOF")')
      STOP
      END
C **********************************************************
C ******************* REFLECTION ***************************

C
      SUBROUTINE REFLECT(NO,NT,THETA,THETAC,Y,X,WT,WR,
     !THETAI,THETAT,RPERP,RPAR,XS)
      REAL NO,NT
      THETAI = ABS(THETA - (3.1416/2.0))
```

```fortran
      TANTA = TAN(THETA)
      IF(TANTA .EQ. 0.0)TANTA = 0.00001
      XS = X - Y*(1.0/TANTA)
      Y  = -1.0 * Y
c     degreei = thetai*180.0/(3.1416)
c     degreet = theta*180.0/(3.1416)
c     degreec = thetac*180.0/(3.1456)
c     write(6,'("thetai=",g13.6,"theta=",g13.6,"y=",g13.6,
c     !"thetac=",g13.6,"x=",g13.6,"xa=",g13.6)')
c     !degreei,degreet,y,degreec,x,xa
      IF(THETAI .LE. THETAC)THEN
      THETAT = ASIN((NO/NT)*SIN(THETAI))
      IF(THETAI .EQ. 0.0)THEN
      WT = 1.0
      WR = 0.0
      GOTO 10
      ENDIF
      RPERP = (-1.0)*((SIN(THETAI-THETAT))/(SIN(THETAI+THETAT)))
      RPAR =     ((TAN(THETAI-THETAT))/(SIN(THETAI+THETAT)))
      WR = (0.5)*(RPERP*RPERP + RPAR*RPAR)
      WT = 1.0 - WR
      ELSE
      WT = 0.0
      WR = 1.0
      ENDIF
10    RETURN
      END


cc    SUBROUTINE REFLECT(NO,NT,THETA,THETAC,Y,WT,WR,
c     !THETAI,THETAT,RPERP,RPAR)
c     REAL NO,NT
c     THETAI = ABS(THETA - (3.1416/2.0))
c     Y = -1.0*Y
c     IF(THETAI .LE. THETAC)THEN
c      THETAT = ASIN((NO/NT)*SIN(THETAI))
c      RPERP = (-1.0)*((SIN(THETAI-THETAT))/(SIN(THETAI+THETAT)))
c      RPAR = ((TAN(THETAI-THETAT))/(SIN(THETAI+THETAT)))
c      WR    = (0.5)*(RPERP*RPERP + RPAR*RPAR)
c      WT    = 1.0 - WR
c      ELSE
c      WT    = 0.0
c      WR    = 1.0
c      ENDIF
c      RETURN
c      END
C ****************************************************************
C ******************** VEIN    ***********************************
C ****************************************************************
      SUBROUTINE VEIN(RANDM1,RANDM2,COEFAV,COEFSV,X,Y,PLNGTH,
     !WEIGHT,THETA)
      TWOPI  = 2.0*(3.1416)
      THETA = TWOPI*(RANDM1)
      PLNGTH = (-1.0*ALOG(RANDM2))/(COEFSV)
      X      = X + (PLNGTH*COS(THETA))
      Y      = Y + (PLNGTH*SIN(THETA))
      WEIGHT = WEIGHT*EXP((-1.0)*(PLNGTH)*(COEFAV))
      RETURN
      END
****************************************************************
******************** TISSUE ***********************************
```

```
      SIGMAS = 56.58
      SIGMAA = 0.0001
COEFS = (RHO*SIGMAS*HEMAT*(1.0-HEMAT))/(1.0E06)
COEFSV = (RHO*SIGMSV*HEMAT*(1.0-HEMAT))/(1.0E06)
TWOPI  = 2.0*(3.1416)
COEFA = (RHO*SIGMAA)/(1.0E06)
COEFAV = (RHO*SIGMAV)/(1.0E06)
WEIGHT = 1.0
WR     =0.0
WT     =0.0
NO     = 1.0
NT     =1.55
THETAC = ASIN(NO/NT)
RPAR = 0.0
RPERP = 0.0
XO    = 0.0
YO    = -200.0
RADIUS = 150.0


C INITIALIZATION OF RANDOM NUMBER GENERATOR AND THE
C GENERATION OF PHOTONS TO BE INSERTED


1     CALL HSRPST(JSEED)
      DO 10 I = 1,NPHOTN
      X    = 0.0
      Y    = 0.0
      IX   = 0
      IY   = 0
      INC = 1
      SLNGTH = 0.0
      SWITCH = 1.0
      FLUX(51,1) = FLUX(51,1) + 1.0


C CALCULATION OF RANDOM NUMBER AND POINT WHERE ITERATION
C OF PHOTON PATHLENGTHS WHILE IN MEDIA


      CALL HSRPUN(N,A)
      IF (INC .GT. 5000) GOTO 10
      RANDM1 = A(1)
      RANDM2 = A(2)


C INSERTION INTO TISSUE


      IF (SWITCH .EQ. 1.0)THEN
      X = 0.0
      PLNGTH = (-1.0*ALOG(RANDM2))/(COEFS)
      Y = Y + (-1.0)*PLNGTH
      SWITCH = 0.0
      ELSE


C CALCULATION OF PHOTON POSITION RELATIVE TO VEIN AND TEST

C TO SEE WHETHER PHOTON IS INSIDE OR OUTSIDE THE VEIN. PHOTON
C ENTERS APPROPRIATE SUBROUTINE WHERE PATHLENGTH AND ABSORPTION
C IS CALCULATED


      RCIRC = SQRT ((X - XO) * (X - XO) + (Y - YO) * (Y - YO))
      IF(RCIRC .LE. RADIUS)THEN


      CALL VEIN(RANDM1,RANDM2,COEFAV,COEFSV,X,Y,PLNGTH,WEIGHT,THETA)
```

```
C ****************************************************************
      SUBROUTINE TISSUE(RANDM1,RANDM2,COEFA,COEFS,X,Y,PLNGTH
     !,WEIGHT,THETA)
      TWOPI = 2.0*(3.1416)
      THETA = TWOPI*(RANDM1)
      PLNGTH = (-1.0*ALOG(RANDM2))/(COEFS)
      X     = X + (PLNGTH*COS(THETA))
      Y     = Y + (PLNGTH*SIN(THETA))
      WEIGHT   = WEIGHT*EXP((-1.0)*(PLNGTH)*(COEFA))
      RETURN
      END           -
C ****************************************************************
C ***************** secnds     ***********************************
C ****************************************************************
C     SUBROUTINE SECNDS(ISEC)
C     integer*2 idat(6)
CInclude:'/sys/ins/time.ins.ftn'
C     call CAL_$DECODE_LOCAL_TIME(idat)
C     ISEC=INT(idat(6) + 10*idat(5))
C     return
C     end
```